Synthesis and Characterisation of Amino Acid Derived Frameworks

Thesis submitted in accordance with the requirements of the University of Liverpool for the degree Doctor in Philosophy by Jamie Andrew Gould

September 2009

THESIS CONTAINS

CD

Synthesis and Characterisation of Amino Acid Derived Frameworks

Abstract

This thesis describes the synthesis and characterisation of a number of metal-organic frameworks, containing amino acids, or ligands derived from amino acids, with the aim of forming homochiral porous materials. The characterisation of two amino-acid derived coordination polymer single crystals by high-pressure crystallography is also presented.

Chapter 1 gives an overview to chiral porous materials, beginning with zeotype materials, and moving on to metal-organic frameworks, highlighting the modular approach to the synthesis of these materials, allowing the production of enantiopure porous materials. Chapter 2 introduces the experimental techniques used to synthesise and characterise the materials presented within this thesis, focussing upon the crystallographic methods used to determine the structure of the materials.

Chapter 3 and 4 describes the synthesis and characterisation of the new materials, highlighting the control of the formation of the structures, by adjustment of the synthetic parameters. The porosity study of a aspartic acid derived material is also presented.

Chapter 5 introduces the use of high-pressure crystallography as a tool to modify the structures a nickel aspartate 1D coordination polymer, causing a cooperative rearrangement within the supramolecular bond structure, caused by the tilting of Ni octahedra within the framework.

Acknowledgements

First of all, I would like to thank Matt Rosseinsky for giving me the opportunity to come to Liverpool and work on this project. It's been a tough three years, but I know that I have learned so much and feel much more driven to succeed than when I first arrived. I am also grateful that he allowed me to pursue my own ideas and interests during the course of my PhD.

Next I would like to thank other significant members of staff in the chemistry department, such as Steve Apter for CHN measurements, and John Bacsa for help with crystallography, but most particularly Darren Bradshaw for the additional guidance and cups of tea in the morning. Other notable people include Andrew Fogg and John Claridge for providing me with useful ideas, and for being good drinking buddies.

I should also mention the MOF group, specifically Jean-No and Jorge for making the lab so good to work in, but also Mike Ingleson, whose intellect and work ethic provided me with much inspiration for the time he was here.

I would like to thank all of the MJR group, both past and present, particularly Mathieu, Carlos and Matthew for getting me involved in football, and Helen and Amy for making me feel so welcome when I arrived. Also James Jones deserves a mention for dragging me down the pub so many times when I knew deep down I shouldn't go.

Thanks also goes to Stephen Moggach from Edinburgh for shouting 'I want to squeeze your MOF's' at the end of the Durham crystallography course, allowing me to further pursue my interest in crystallography and for being a good friend.

My thanks also goes to my family, for all the love and support, not only during my PhD, but ever since I started university. I wouldn't be here if it wasn't for all of you.

Finally, I'd like to thank my girlfriend Jess, who has been really supportive during my writing up period and pushing me to get things done, and for being a great listener whenever I panicked and thought that it would never be done. I probably don't say enough how much I've really appreciated it, but hopefully this will go a little way to demonstrate how wonderful I think you are.

Contents

Chapter 1 Introduction

1.1 Nanoporous materials

Materials with internal surface and having voids on the same scale as molecules are of significant scientific and technological interest as they allow manipulation of chemical moieties with size/shape recognition, and as such have found applications in the areas of ion exchange, separation and catalysis. These materials are classed in terms of the pore size by IUPAC,[1] with void sizes larger than 50nm termed macroporous, between 2 and 50nm termed mesoporous and less than 2nm termed microporous. The direct control over the pore geometry and its distribution within materials is of particular interest, as the control of these factors implies that the properties of the materials can be tailored for specific function. For instance, a material that contains a pore size of 10nm could be used as a molecular sieve, restricting access only to chemical species that are the same size, or smaller than 10nm. If such a material had catalytic properties, it could be used to catalyse chemical reactions with molecules based upon the size recognition described above, allowing a degree of selectivity for the catalytic process. This selectivity could be enhanced further if the chemistry of the internal surface could be tailored, for example pores lined with a hydrophilic surface would only allow access to molecules which are also hydrophilic, a property which has been put into practice with molecular sieves used as drying agents, removing water from organic solvents.

One major challenge in the synthesis of porous materials is the control of chirality, with potential properties in enantioselective separation and catalysis, which could have a major societal impact, as reactions within these materials from achiral precursors could yield products that are homochiral, thereby removing the

dependence upon utilising expensive enantiopure starting materials in the pharmaceutical industry. The work concerned within this thesis is upon the synthesis and characterisation of chiral porous materials called metal-organic frameworks from amino acid starting materials, which are both readily available and cost-effective. What follows is a description of the state of the art of chiral porous materials focussing initially upon the inorganic zeolite/zeotypes, followed by a detail description of the strategies involved in the formation of homochiral metal-organic frameworks, ending with a review of amino-acid coordination chemistry.

1.2 Zeolites – inorganic porous materials

Zeolites are the most widely studied type of microporous material, defined as crystalline extended aluminosilicates materials comprised of vertex sharing SiO_4/AlO_4 tetrahedral subunits. The formed structures are anionic due to the presence of alumina, and contain well-defined pore systems utilised in a variety of applications such as ion exchange, catalysis and separation. Zeolites are typically synthesised using hydrothermal/solvothermal methods with either inorganic cations or cationic ammonium species as structure directing agents (SDAs). These act to charge balance the structure, and also as a structural template, with the corner sharing anionic material forming cages around the cationic SDAs. The template is then removed by either ion exchange or calcination, leaving open pore frameworks containing charge balancing cations or protons respectively. The introduction of other chemical species to substitute Si/Al within the structures have led to the development of a host of different inorganic materials, including the aluminophosphates (where P^{5+} is used in the synthesis instead of Si, leading to neutral frameworks), gallophosphates, indium phosphates, and transition metal

phosphates.[2] Due to the strong bonds contained within the frameworks, zeotype materials possess high thermo- and chemostability, making them ideal materials for applications at high temperatures, such as the catalytic cracking of petroleum, and it is said that every molecule of petroleum has passed through zeolite Y. However the template-directing synthesis of these materials, make the introduction of chirality a considerable challenge.

1.2.1 Chiral zeolitic materials

Chirality within zeolites is due to the crystallisation of these materials in chiral space groups, with no chiral centres within the framework apparent in the structures.[3] The first occurrence of a chiral zeolite was zeolite beta[4] which is comprised of two closely related intergrown polymorphs (A and B), both containing three-dimensional pore systems based around 12-rings (Figure 1.1), however polymorph A is chiral, and polymorph B is achiral. Polymorph A crystallises in the space groups $P4_122$ or $P4_322$, with the change in screw axis dependent upon the handedness of the structure (left-hand gives $P4_322$, and right-hand gives $P4_122$). The result is a helical framework in a sequence of a single hand, such as LLL, or RRR. The second polymorph, B contains helices of both hands in the sequence RLRL, and crystallises in the achiral space group C2/*c*. Despite numerous attempts, it has not been possible to isolate polymorph A as a single homochiral material, however it is possible to isolate the achiral polymorph B utilising different reaction conditions to those outlined in the original synthesis.[5]

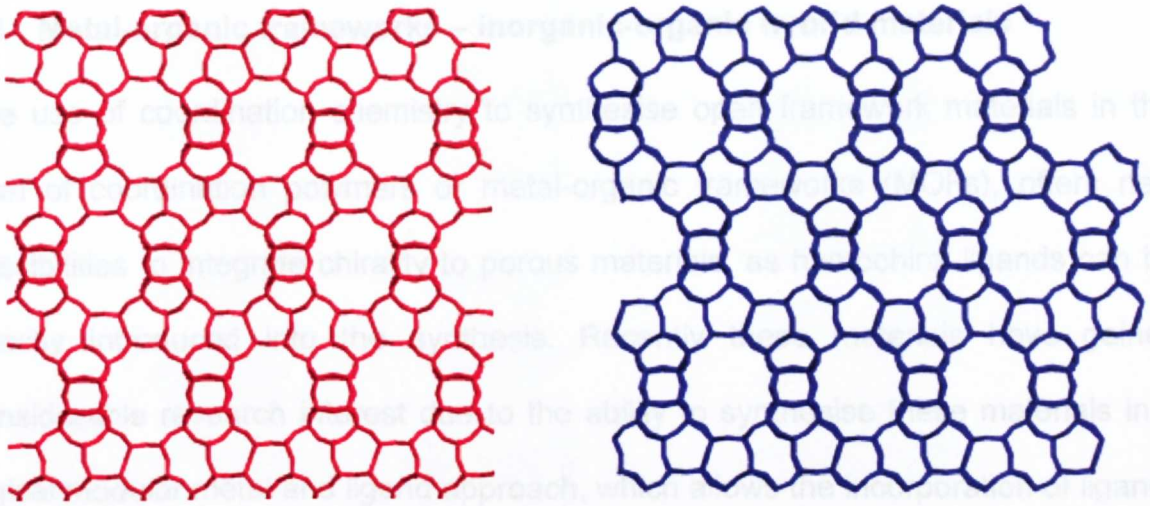

Figure 1.1. The two intergrown polymorphs of zeolite beta. Polymorph A, left, is chiral and crystallises in the tetragonal space group, $P4_122$, left, and polymorph B, right, which is achiral, and crystallises in the monoclinic space group $C2/c$,

Other chiral zeolitic materials include the aluminophosphate VPI-5,[6,7] which crystallises in the space group $P6_3$, and contains triple-helical channels filled with water; however the material loses its chirality upon dehydration, transforming to an achiral space group, and the titanosilicate ETS-10[8] which is comprised of two intergrown frameworks, analogous to zeolite beta. Recently the chiral germanosilicate, ITQ-37 was reported by Corma at al,[9] which was formed using a *meso* SDA. Each crystal is enantiopure, with the left-hand crystallising in $P4_332$, and the right-hand in $P4_132$. ITQ-37 also displays the lowest framework density of all existing 4-connected crystalline oxide frameworks, with 10.3 tetrahedral atoms per 1000 $Å^3$.

1.3 Metal-organic frameworks – inorganic-organic hybrid materials

The use of coordination chemistry to synthesise open framework materials in the form of coordination polymers or metal-organic frameworks (MOFs), offers new possibilities to integrate chirality to porous materials, as homochiral ligands can be directly introduced into the synthesis. Recently these materials have gained considerable research interest due to the ability to synthesise these materials in a logical modular metal and ligand approach, which allows the incorporation of ligands with different functionalities, and hence the chemistry of the materials to be tailored. One excellent example of this approach was performed by Yaghi et al in the formation of the IsoReticular Metal-Organic Framework series (IRMOF),[10] where the 1,4-benzenedicarboxylate (bdc) ligands within the framework MOF-5 ($[Zn_4O(bdc)_3]$)[11] were substituted for a series of dicarboxylate based ligands which display the same connectivity. The result was a family of frameworks with identical topology, due to the presence of a $Zn_4O(OAc)_6$ secondary building unit (SBU) within each structure, which has octahedral connectivity. Linking these octahedral SBUs together with different straight rod-like dicarboxylate ligands results in MOFs with identical cubic topology, but different pore sizes and chemistries, allowing an element of design within these structures to be realised (Figure 1.2).

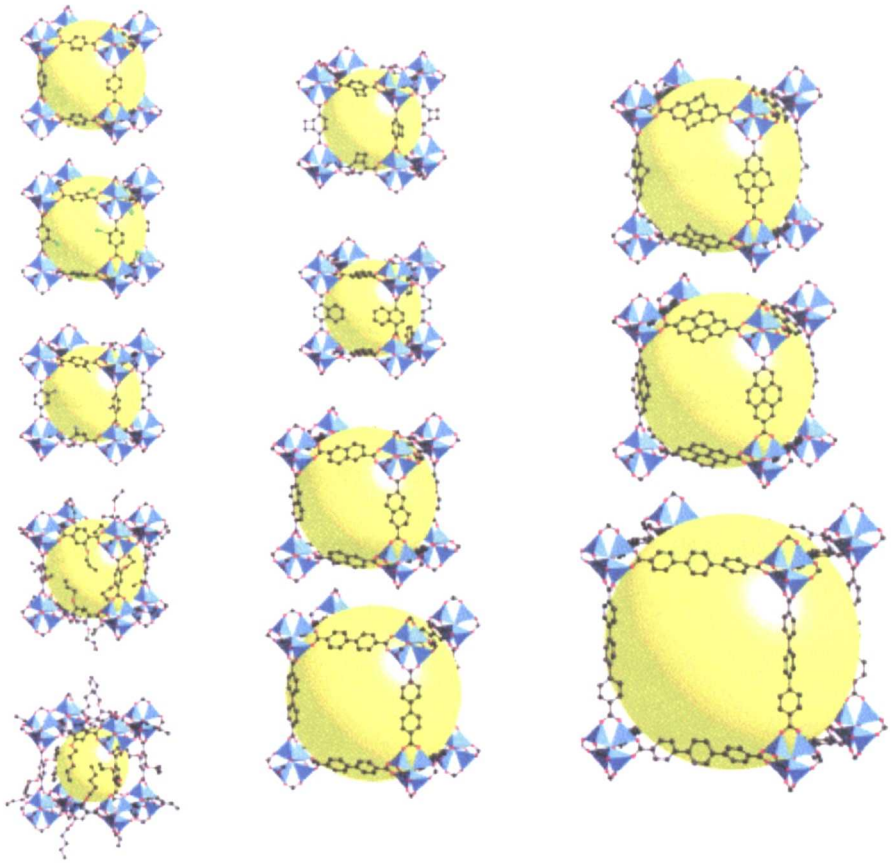

Figure 1.2. The isoreticular metal-organic framework (IRMOF) series based upon the formation of the $Zn_4O(OAc)_6$ octahedral cluster in reactions with linear dicarboxylic acids. Zinc is denoted by the blue tetrahedra, oxygen is red, carbon is black, and all hydrogen atoms are removed for clarity. The solvent accessible volume is denoted as yellow spheres.

This approach has since been extended with the use of copper acetate dimer paddlewheel SBUs with square-shaped connectivity and tetracarboxylic acids, which also has square-shaped connectivity by Schroder et al,[12,13] and substitution of the straight bdc ligands in MIL-53[14] (a set of M^{3+} based materials comprised of infinite 1D M-OH-M chains linked in the second and third dimensions by bdc), in an analogous manner to the IRMOF series.[15,16]

1.3.1 Chirality in metal-organic frameworks from achiral ligands

The first reports of chirality within MOFs resulted from spontaneous crystallisation in chiral space groups,[17,18] as observed within the chiral zeolites, despite the formed frameworks being devoid of any actual chiral centres. However, although the single crystals measured demonstrated that the materials were homochiral, with Flack parameters close to zero, the bulk samples were racemic, containing both enantiomorphs. There have been several successful attempts to resolve the structures, to yield homochiral materials and a brief discussion of the different methods employed follows.

1.3.1.1 Chirality by seeding

The first method by Aoyama et al[19] involved the growth of enantiopure crystals by adding a seed crystal to the reaction mixture prior to synthesis. The combination of $Cd(NO_3)_2 \cdot 4H_2O$ and the achiral ligand, 5-(9-anthracenyl)pyrimidine (anpym) in ethanol leads to the formation of the chiral material $[Cd(anpym)(NO_3)_2(H_2O)(EtOH)]$, which exists as 1-dimensional helical coordination polymers held together in the solid state by hydrogen bonding, with all strands within the structure displaying the same handedness. The material crystallises in the chiral space group $P2_1$, and is comprised of an octahedral Cd^{2+} ion, resulting from the coordination of two anpym ligands, water, ethanol and two nitrate ions. The 1D polymer arises from the bridging functionality of the 1,3-nitrogen atoms of the pyrimidine coordinating to two separate Cd^{2+} ions, with the helical chirality induced by the *cis* coordination, and the presence of bulky anthracene units (Figure 1.3).

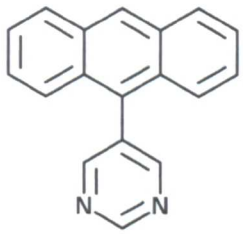

5-(9-anthracenyl)pyrimidine (anpym)

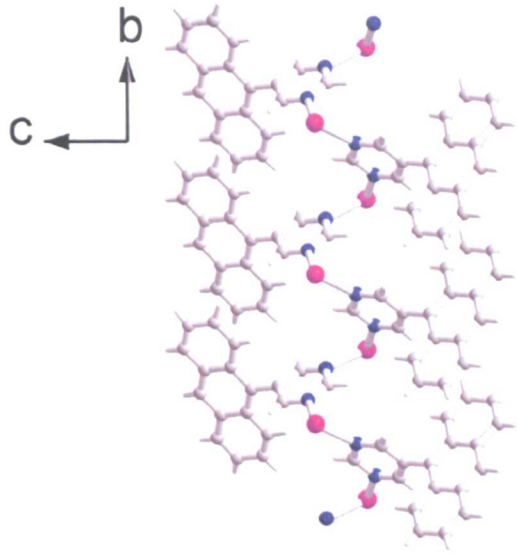

Figure 1.3. The achiral ligand anpym (left) used in the synthesis of the 1D helical polymer of [Cd(anpym)(NO_3)$_2$(H_2O)(EtOH)] (right). The nitrate, water and ethanol ligands are removed for clarity. Cadmium is magenta, carbon is grey, nitrogen is blue and hydrogen is white.

Although the single crystals formed are enantiopure, the bulk was shown to be racemic with an equal proportion of crystals containing helices which rotate in clockwise and anti-clockwise directions. However, the authors found that the addition of an enantiopure crystal to the reaction mixture, directs the chirality of the bulk material leading to a homochiral product. The chirality was demonstrated by the use of circular dichroism, and the method further verified by seeding materials containing the opposite hand, showing the required change in the circular dichroism spectra. The 1-dimensional helices are densely packed in the crystal structure, and are devoid of accessible volume.

1.3.1.2 Induction of chirality using chiral co-ligand templating

An alternative approach to control the handedness of bulk helical MOFs was demonstrated by Rosseinsky et al in the utilisation of enantiopure co-ligands, which do not impart any bridging functionality, to template helix formation to yield a homochiral material.[20] The slow diffusion of pyridine (py) in an ethylene glycol (eg) solution containing 1,3,5-benzenetricarboxylic acid (H_3btc) and $Ni(NO_3)_2 \cdot 6H_2O$ yields the three-dimensional chiral framework $[Ni_3(btc)_2(py)_6(eg)_6]$•guests, which crystallises in the cubic space group $P4_232$.[21] The structure is comprised of octahedral Ni^{2+} centres linked together axially with btc to form four interpenetrating chiral 10-3a nets, with both enantiomers present in the bulk material. The eg and py ligands coordinate to Ni^{2+} both in *cis* arrangements in the equatorial positions, with the eg ligand providing additional stabilisation by donating a hydrogen bond to btc (Figure 1.4). Substitution of achiral eg in the reaction mixture with enantiopure 1,2-propanediol (1,2-pd) leads to the formation of the chiral framework, $[Ni_3(btc)_2(py)_6(1,2\text{-pd})_3]$•guests, which crystallises in the space group $I4_132$, and is comprised of two interpenetrated 10-3a nets. The coordination sphere of Ni^{2+} in the 1,2-pd material was found to be slightly different to the eg grown material, with only one 1,2-pd bound to Ni^{2+}, via a bidentate chelation. The bulk material was found to be homochiral by structure solution from several different crystals from a single batch grown from enantiopure 1,2-pd, and the ligand control of helix formation was confirmed by measuring the single crystals formed separately from (*R*)-1,2-pd and (*S*)-1,2-pd, which demonstrated that (*R*) and (*S*) yielded anti-clockwise and clockwise helical frameworks respectively (Figure 1.4).

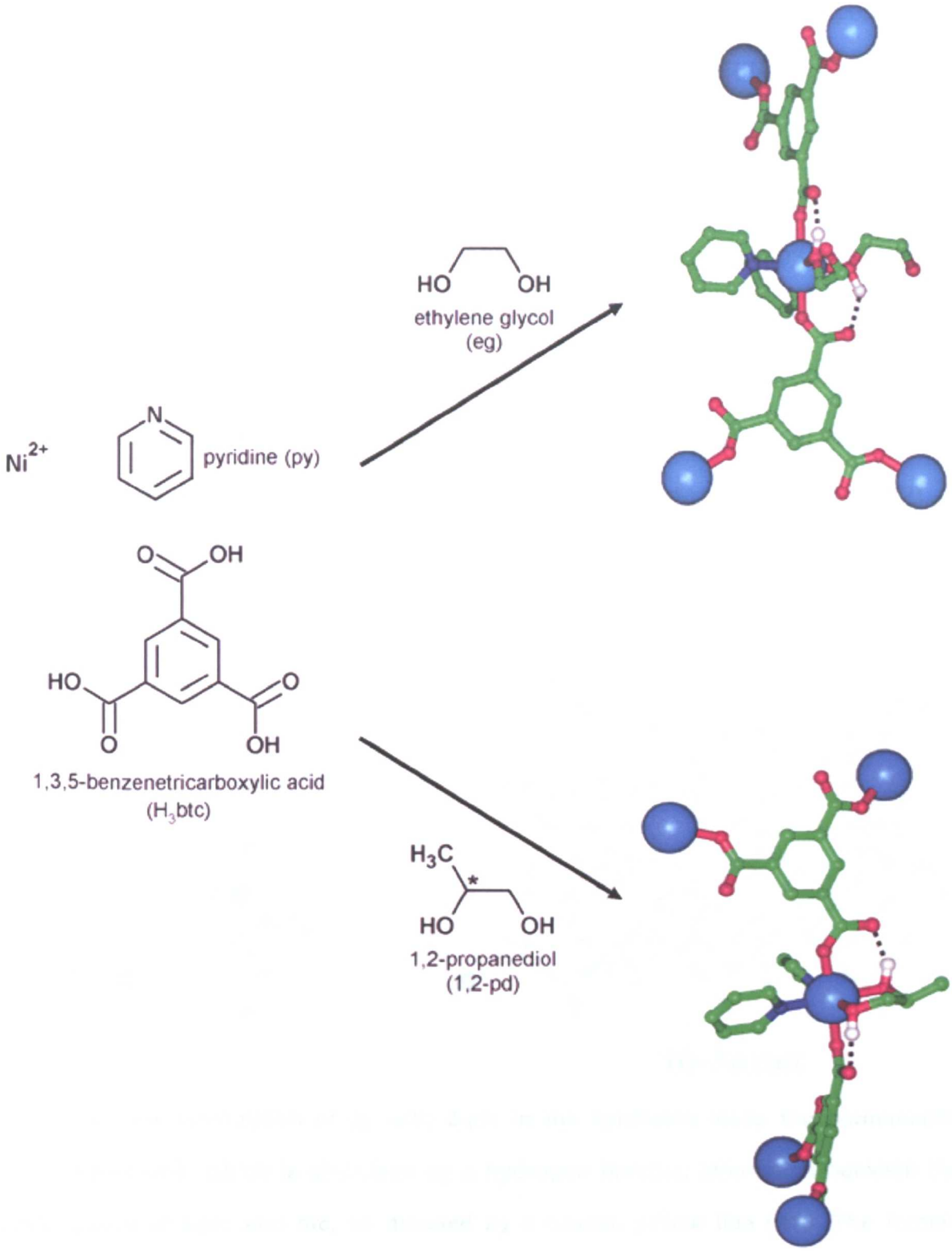

Figure 1.4. The control of crystallisation of 10-3a nets comprised of Ni^{2+} linked by axial btc, use of chiral co-ligands as templating agents. Nickel is light blue, carbon is green, oxygen is red, nitrogen is blue and hydrogen is white. Hydrogen bonds are denoted by dashed black lines. Hydrogen atoms not involved in hydrogen bonding interactions are removed for clarity.

The formed frameworks grown from 1,2-pd and py do not display any permanent porosity, and collapse upon removal of the guest moleculess. This can be avoided by exchanging py for 3-picoline (3-pic) in the synthesis yielding the homochiral framework; $[Ni_3(btc)_2(3\text{-pic})_6(1,2\text{-pd})_3]\bullet$guests,[22] which remains structurally intact upon guest removal, and displays permanent porosity, and contains pores larger than 10.5 Å (determined by sorption of a range of probe molecules of varying sizes). The structure of the framework upon desolvation is stabilised by the presence of a hydrogen bonding interaction between the methyl group of 3-pic and the non-coordinating C=O carboxylate oxygen atom of btc. (H···O = 2.768(2) Å) (Figure 1.5).

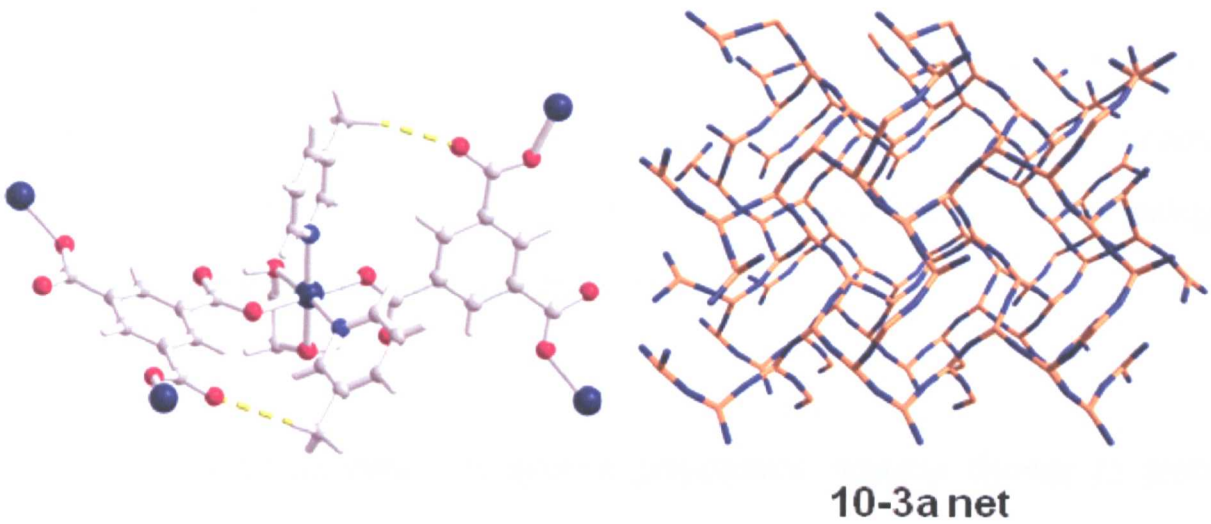

Figure 1.5. The substitution of py with 3-pic in the synthesis leads the permanently porous framework, which is stabilised by a hydrogen bonding interaction between the methyl group of 3-pic and btc, as denoted by a broken yellow line (left). The formed framework crystallises in a chiral cubic space group, and consists of a doubly interpenetrated 10-3a net (right).

1.3.1.3 Chiral frameworks using chiral ionic liquids as a solvent

Recently, Morris et al introduced the ionothermal synthesis of homochiral frameworks from achiral ligands using the chiral ionic liquid 1-butyl 3-methylimidazolium L-aspartate as a solvent/template.[23] The homochiral material, $[Ni(Hbtc)_2(H_2O)_2]$ crystallises in the space group $P4_12_12$, as a diamonoid net, and is comprised of Ni^{2+} ions linked together by the partially deprotonated Hbtc, forming a 3-dimensional framework. The bulk chirality of the material was determined by solving the absolute structure of 10 different single crystals, each of which gave the same enantiomorph, with the chirality reversed by using the opposite handed aspartate. In addition, reaction of the starting materials using the achiral ionic liquid 1-butyl 3-methylimidazolium bromide, results in the formation of the achiral framework $[Ni_3(Hbtc)_4(H_2O)_2]$ demonstrating further that the chirality within the framework is directly induced by the chiral ionic liquid. However, the ionic liquids cannot be removed from the pores without collapse of the structure, demonstrating that these materials are not permanently porous.

1.3.2 The use of synthetic enantiopure polydentate bridging ligands to form homochiral metal-organic frameworks

In addition to using chiral co-ligands to direct helical framework formation, enantiopure chiral ligands, which bridge between metal centres, can also lead to the formation of homochiral frameworks. These frameworks would contain chiral groups within the formed materials, which could find applications in the use of enantiomeric separation, and catalysis, if a catalytic centre could also be incorporated into the structure. To date there are two distinct strategies of building MOFs from chiral

polydentate ligands, the first was developed by Kim et al,[24] and utilises modification of enantiopure molecules from the chiral pool to include functionalities such as carboxylate or pyridyl groups, that could aid framework formation. Kim and co-workers first demonstrated this strategy with the synthesis of the framework $[Zn_3(\mu_3\text{-}O)(tartpy\text{-}H)_6]$•guests (D-POST-1) from the solvothermal reaction of a pyridyl-modified tartaric acid derived ligand (tartpy) with $Zn(NO_3)_2$ in H_2O/MeOH (Figure 1.6).[24]

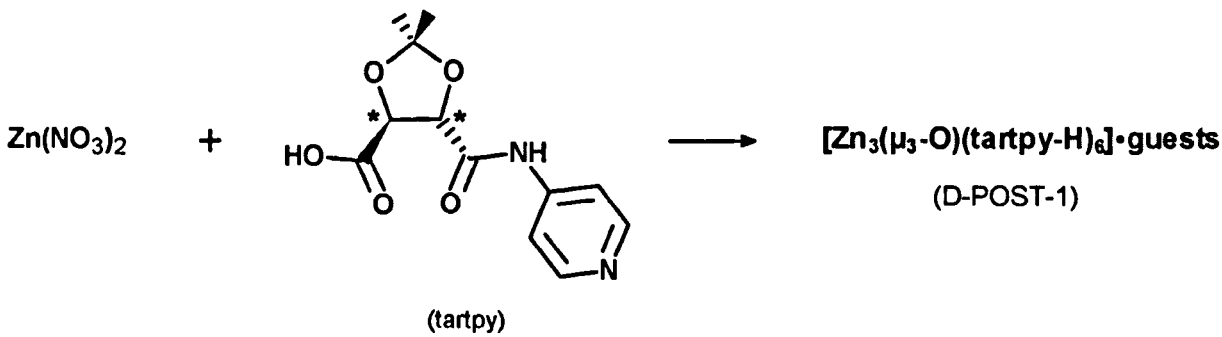

Figure 1.6. The synthesis of D-POST-1 via reaction of $Zn(NO_3)_2$ with an enantiopure pyridyl-modified tartaric acid derived ligand. Asterisks denote the chiral centres within the molecule.

The resulting framework crystallises in the trigonal space group *P*321, and is comprised of a $Zn(\mu_3\text{-}O)$ trizinc carboxylate cluster SBU connected via the carboxylate and pyridyl groups of tartpy, resulting in a 2D layer structure with a 1-dimensional pore system that have triangular shaped windows with a side length approximately equal to 13.4Å (Figure 1.7a and b).

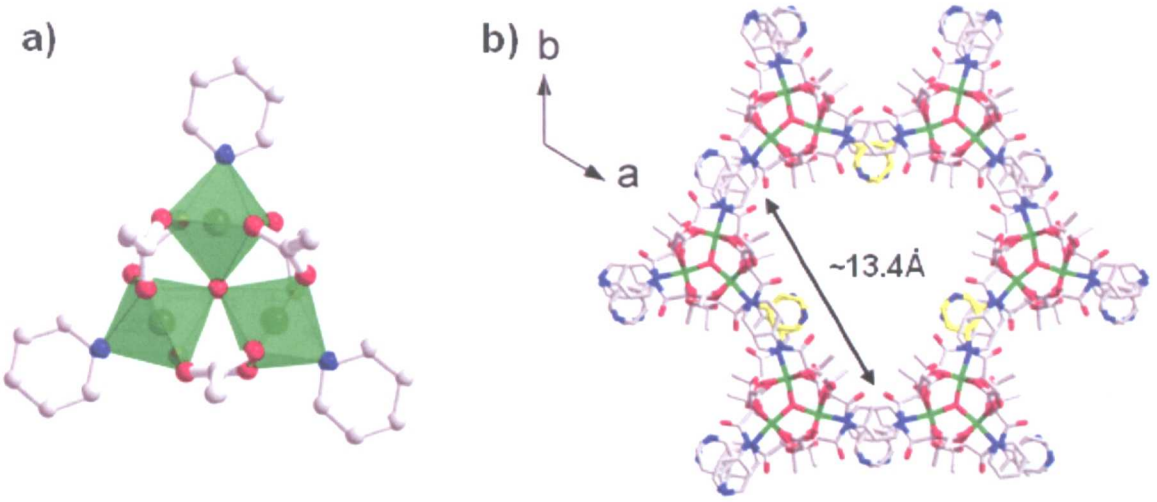

Figure 1.7. a) The μ_3-trizinc carboxylate cluster SBU within D-POST-1, with a pyridyl moiety coordinated to each Zn^{2+}. b) The triangular shaped window of the 1-dimensional channels that run along the *c*-axis, with a side length of ~13.4 Å. The pendant pyridyl units of tartpy which point towards the centre of the pore are coloured in yellow.

Although all 6 ligands within the structure each coordinate to the trinuclear zinc cluster via the carboxylate groups, only 3 of the pyridyl groups are bound to Zn, with the remaining three pointing directly into the channel centre. In addition, the host material has a charge of -2 per framework unit, balanced by the presence of two protons upon two of the three pendant pyridyl groups within the framework. This gives D-POST-1 the potential to be an active acid catalyst. However, removal of the encapsulated guest causes structural collapse, therefore in order to test the catalytic capabilities of the material, reactions such as the asymmetric transesterification of 2,4-dinitrophenyl acetate with the racemic alcohol 1-phenyl-2-propanol (Figure 1.8), were performed in the presence of D-POST-1. This yielded a chiral product with an enantiomeric excess (ee) of 8% in favour of the *S* enantiomer, with the handedness reversed with the same ee if the reaction is performed in the presence of the framework of opposite handedness. The catalysis was shown to occur primarily within the pores of the material, as the use of bulky substrates for reaction showed

decreased reaction rates. This was the first observation of asymmetric catalysis within a metal-organic framework.

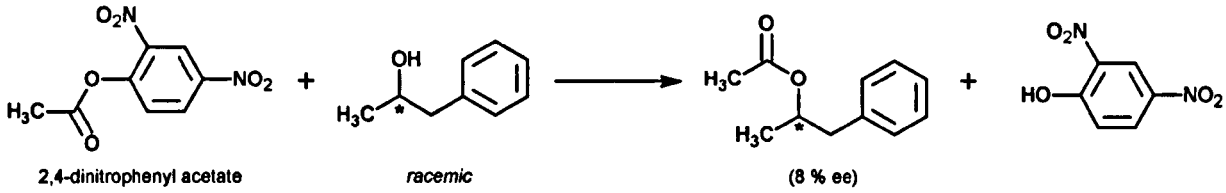

Figure 1.8. The transesterification reaction performed in CCl_4 at 27 °C, in the presence of D-POST-1 which acted as an asymmetric catalyst giving an enantiomeric excess of 8% in favour of the *S* enantiomer. Asterisks represent chiral centres.

Another notable example of modification of chiral molecules for use as framework forming ligands was produced from the Lin group using the BINOL-derived ligand (*R*)-6,6′-dichloro-2,2′-dihydroxy-1,1′-binaphthyl-4,4′-bipyridine (BINOL-bipy).[25] The ligand contains two types of functional groups; axial pyridine groups for framework formation and hydroxyl groups in the centre of the BINAP moiety (Figure 1.9a). Reaction of the BINOL-bipy with $CdCl_2$ yields the framework $[Cd_3(\mu_2\text{-}Cl)_6(\text{BINOL-bipy})_3]$, which crystallises in the triclinic space group *P*1, and is comprised of 2-dimensional square grids of Cd(BINOL-bipy) linked by μ_2-Cl atoms in the third dimension. The resulting material contains square chiral channels with a cross-section of ~1.6 *x* 1.8 nm, with the hydroxyl groups from one of the three BINOL-bipy ligands from the asymmetric unit pointing directly into the centre of the pore. As the hydroxyl groups are directly attached to the BINAP functionality of the ligand, these are themselves intrinsically chiral, and Lin et al took full advantage of this by reacting with titanium isopropoxide to yield the catalytically active framework, $[Cd_3(\mu_2\text{-}Cl)_6(\text{bipy-BINOLate-Ti}(O^iPr)_2)(\text{BINOL-bipy})_2]$, which contains a BINOLate-Ti(^{i}OPr)$_2$ active site (Figure 1.9b).

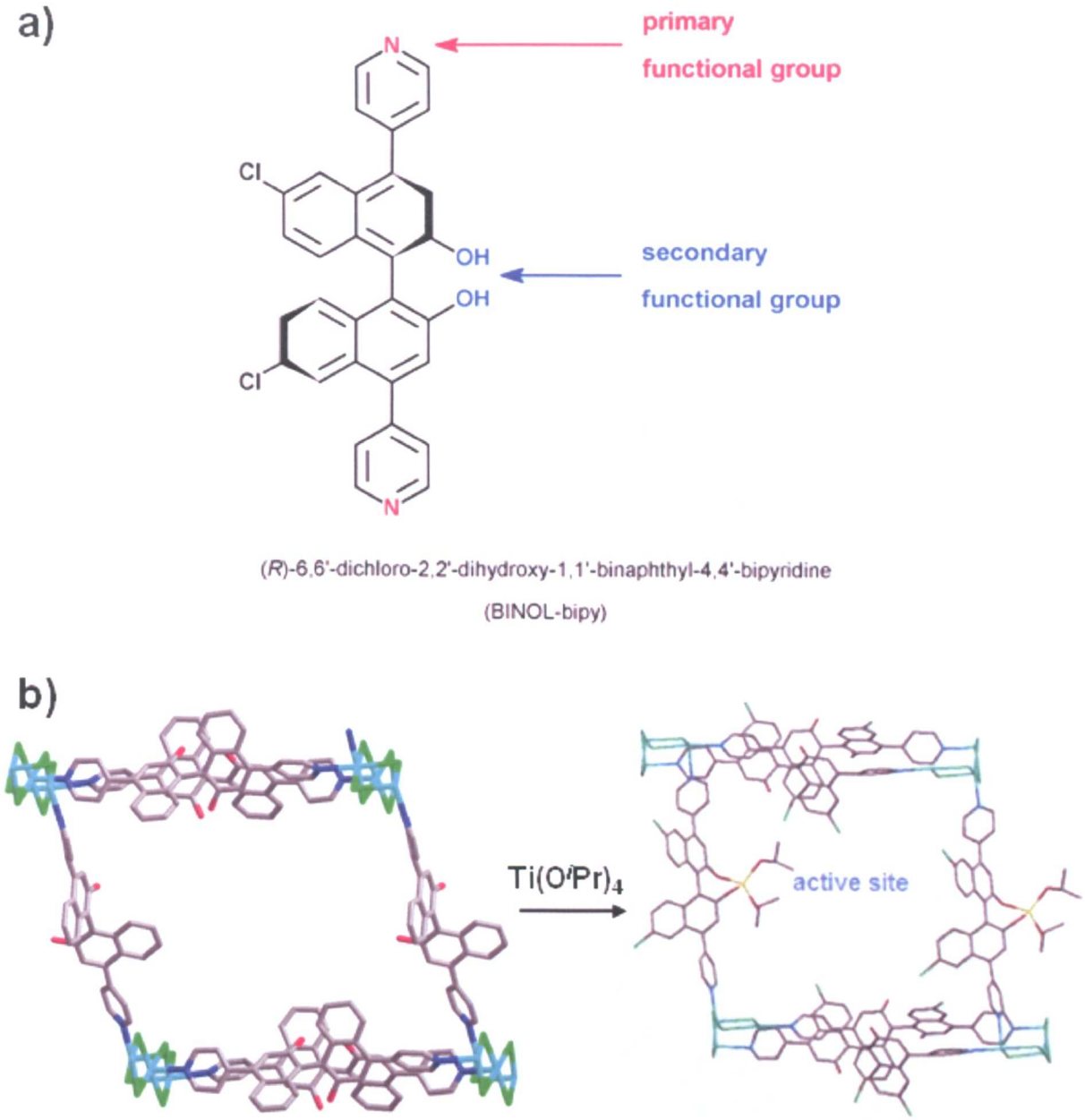

Figure 1.9. a) The bifunctional BINOL-bipy utilised in the synthesis of $[Cd_3(\mu_2\text{-}Cl)_6(BINOL\text{-}bipy)_3]$ by Lin and co-workers. b) The post-synthetic functionalisation to yield the yield the catalytically active framework, with $Ti(^iOPr)_2$ moieties pointing directly into the centre of the pores.

This post-synthetically functionalised framework was found to be permanently porous, by measurement of a CO_2 isotherm, and has been demonstranted to be an excellent catalyst for the addition of diethylzinc to aldehydes, with ee's comparable to the homogeneous $Ti(^iOPr)_4$ analogue. The aldehyde catalysis was shown to occur

only at the active site within the pores, as the reaction of bulky aldehydes, which are too large to access the interior of the material, does not occur. Additionally, the presence of Ti^{4+} was also found to be essential to catalytic activity, as the parent material devoid of $Ti(^{i}OPr)_2$, was also found to be inactive.

Other groups have managed to include catalytically active chiral centres into MOFs, notably Hupp and co-workers,[26] with the synthesis of a chiral salen based framework formed from the extended bdc derivative, biphenyldicarboxylate (bpdc) and the synthetic chiral ligand, (*R*,*R*)-(2)-1,2-cyclohexanediamino-*N*,*N*′-bis(3-*tert*-butyl-5-(4-pyridyl)salicylidene)$Mn^{III}Cl$ ((chiral-salen)$Mn^{III}Cl$) with Cu(II) ions (Figure 1.10).

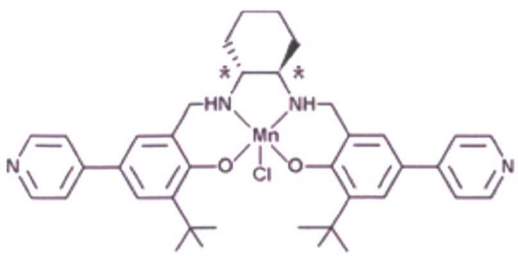

(chiral-salen)$Mn^{III}Cl$

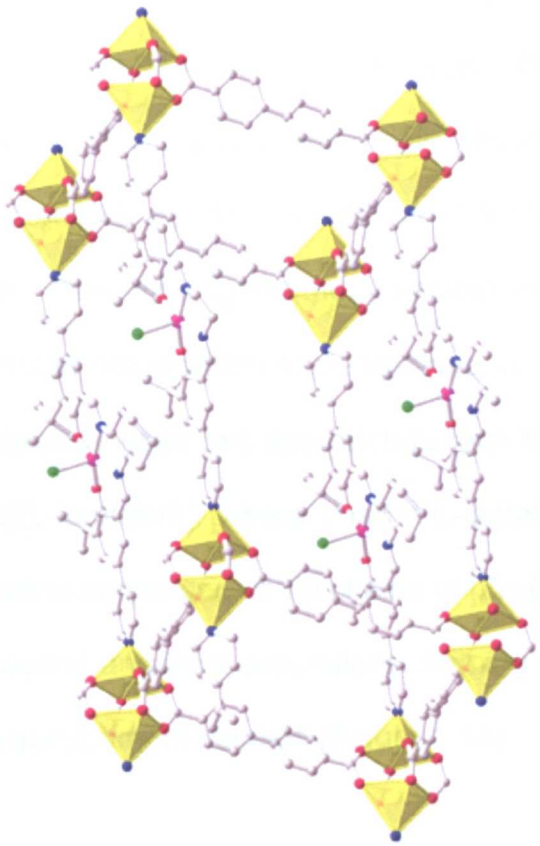

Figure 1.10. The synthetic bipy-salen based ligand utilised by Hupp et al (left), and the chiral catalytic framework formed by reaction with Cu and bpdc (right).

The formed structure displays cubic connectivity, derived from the square $Cu_2(bpdc)_2$ paddlewheel SBUs linked together by the (chiral-salen)$Mn^{III}Cl$ pyridyl struts. The framework is permanently porous, as the structure retains crystallinity upon desolvation. The catalytic capability of the framework was examined by performing asymmetric olefin epoxidation of 2,2-dimethyl-2*H*-chromene as a substrate resulting in the desired product in a 71% yield with 82% ee, which is comparable to the ee of reactions performed homogeneously in the presence of the free ligand (88%).

1.3.3 Chiral mixed ligand frameworks from naturally occurring chiral ligands

An alternative and more economic approach to exhaustive organic synthesis to yield ligands suitable for MOF formation is to use naturally occurring chiral molecules with existing functionalities that can bridge between metal centres. However, this combination tends to produce dense frameworks, lacking any accessible volume. This problem can be overcome by the use of a second ligand, that can act as a rigid spacer, such as 4,4′-bipyridyl (bipy), or H_2bdc. The chiral ligand/metal combination can then be noted as an SBU, analogous to those noted within such frameworks as MOF-5 and MIL-53. Recently Kim et al, successfully used this approach to form the homochiral mixed-ligand framework $[Zn_2(bdc)(L\text{-lac})(dmf)]$, where L-lac = L-lactate, and dmf = dimethylformamide.[27] The framework is comprised of 1D chains of $[Zn_2(L\text{-lac})(dmf)]^{2-}$, which are pillared by bdc in the second and third dimensions, forming 1-dimensional nanoporous channels containing guest dmf molecules (Figure 1.11).

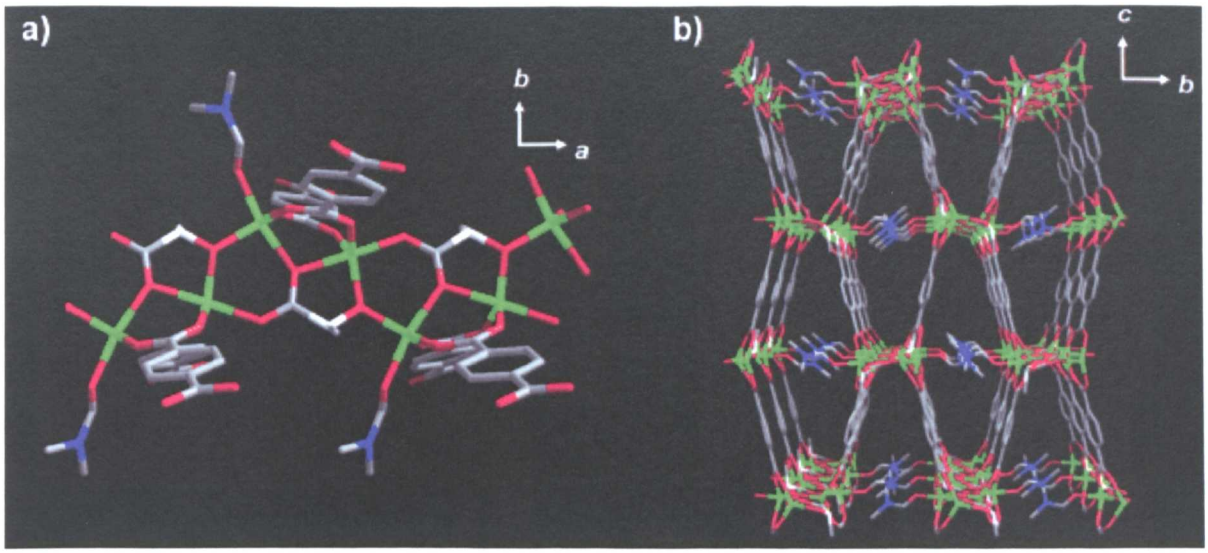

Figure 1.11. The chiral mixed-ligand framework $[Zn_2(bdc)(L\text{-}lac)(dmf)]$. a) The 1D chain of $[Zn_2(L\text{-}lac)(dmf)]^{2-}$ along the *a*-axis which is linked by bdc to yield b) The porous material with 1D rhomboidal-shaped channels. Zinc is green, carbon is grey, oxygen is red and nitrogen is blue. Chiral centres are labelled in white.

Removal of the guests by heating, causes partial framework collapse, as noted by the loss in crystallinity within the powder X-ray diffraction patterns compared to the as-synthesised material. However, the guest can be exchanged for other guest molecules, and the framework was demonstrated to enantioselectively adsorb chiral thioether sulfoxides with a maximum ee of 28%.

1.4 The coordination chemistry of amino acids

The amino acids are a set of naturally occurring enantiopure chiral acids, which contain both an amine and a carboxylic acid functionality, with the general formula $H_2NCH(R)CO_2H$.[28] There are 20 different naturally occurring acids, with the variety arising from the constitution of the side chain, 19 of which are chiral (R = H in glycine gives an achiral molecule) making them ideal building blocks for the synthesis of MOFs as the differing chemistries of these ligands allow internal surfaces of synthesised frameworks to be systematically modified.

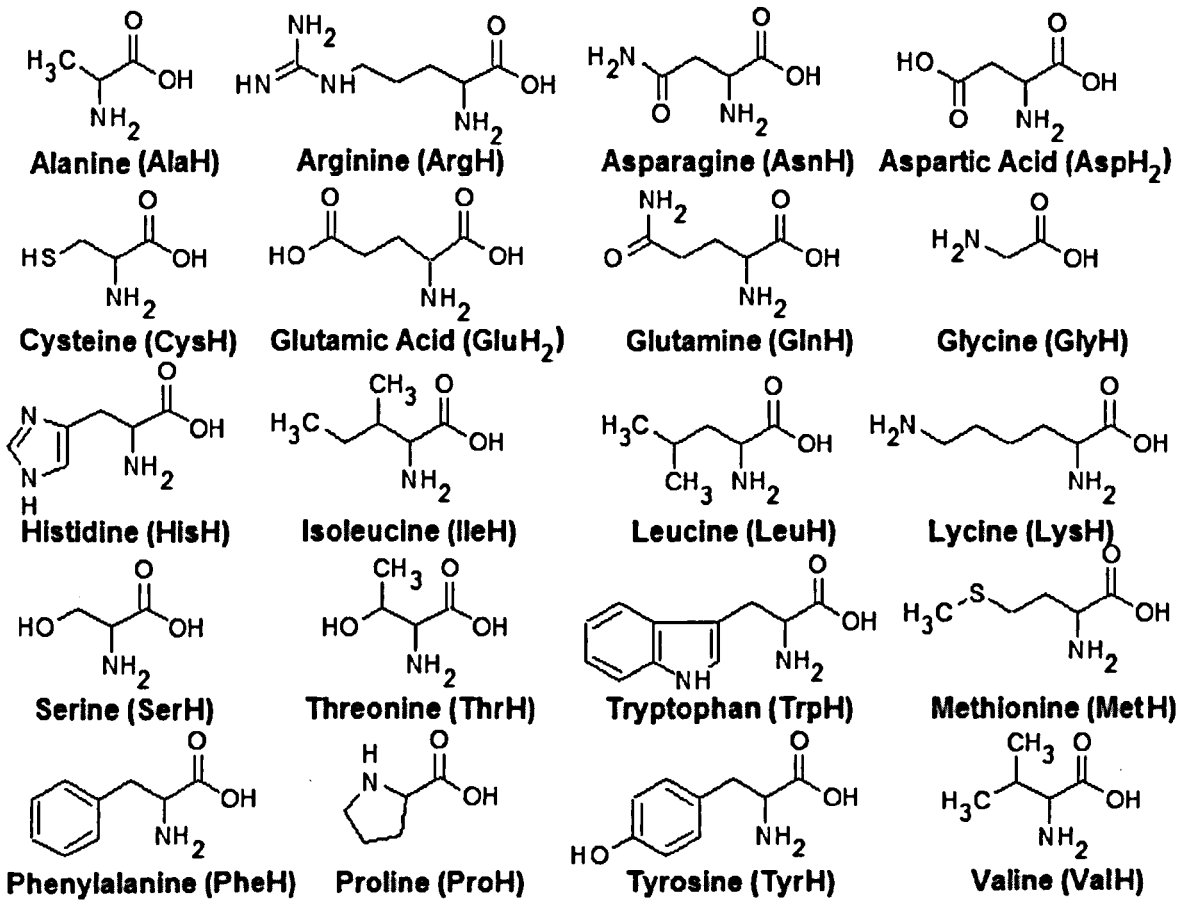

Figure 1.12. The 20 naturally occurring amino acids.

1.4.1 Metal complexes with amino acid ligands

Amino acid coordination chemistry is dominated by the formation of a bidentate N,O chelation to a single metal centre, resulting in a 5-membered metallacycle(Figure 1.13).[29] Typically amino acids without coordinating side chains bind to M^{2+} in a 1:2 metal:ligand ratio,[30-33] and M^{3+}, in a 1:3 M:L ratio. The M:L ratio can be lowered to 1:1 by the use of co-ligands, such as 2,2′-bipyridyl, or 1,10-phenanthroline.[34]

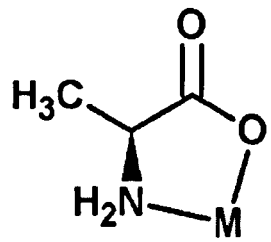

Figure 1.13. The 5-membered N,O metallacycle that is prevalent in amino acid chemistry.

The situation is different with amino acids that contain coordinating side chains, such as the acidic L-aspartate, or the basic L-histidine, as a number of different coordination modes are possible, including tridentate chelation with the side chain coordinating to the same metal centre as the N,O metallacycle,[35-40] or the coordinating side chain bridges to a second metal centre.[41-45] The M:L ratio can also be varied depending upon the amino acid, the existence of co-ligands, and the stoichiometry of the reagents within the synthesis. For example, L-histidine coordinates to M^{2+} with a M:L ratio of 1:2, as two tridentate N,O,N chelations in neutral conditions,[46] whereas L-aspartate coordinates with a M:L ratio of 1:1, due to the anionic nature of the carboxylate side chain.[38-40] In the presence of 2,2′-bipyridyl ligands, L-histidine coordinates to M^{2+} with a M:L ratio of 1:1, with the presence of ClO_4^- counterions,[34] in analogous fashion to that observed with amino acids devoid of coordinating side groups. In addition, recently L-histidine has been used to

synthesise a magnetic pseudo cubane clusters with Co and Mo with each L-histidine forming a tridentate chelation (Figure 1.14).[35]

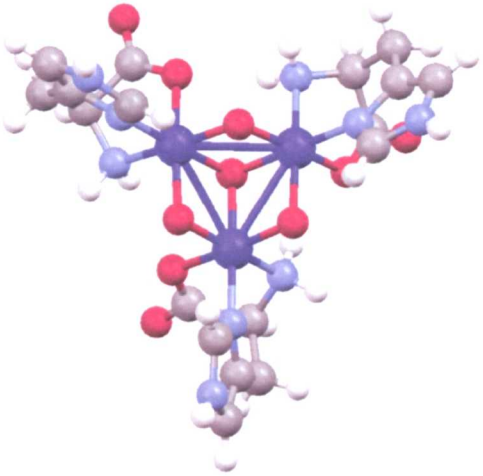

Figure 1.14. The L-his pseudo cubane cluster formed with Co. Each L-his coordinates to Co via a tridentate N,O,N chelation with the coordination spheres of Co filled by 3 *x* μ_2-O and 1 *x* μ_3-O.

The coordination chemistry of the amino acids can be altered by lowering the pH sufficiently to protonate the amine group. In these conditions, the ligands coordinate to more than one metal centre forming polynuclear clusters similar to those used as inorganic SBU's in MOF formation (Figure 1.15).[47-50]

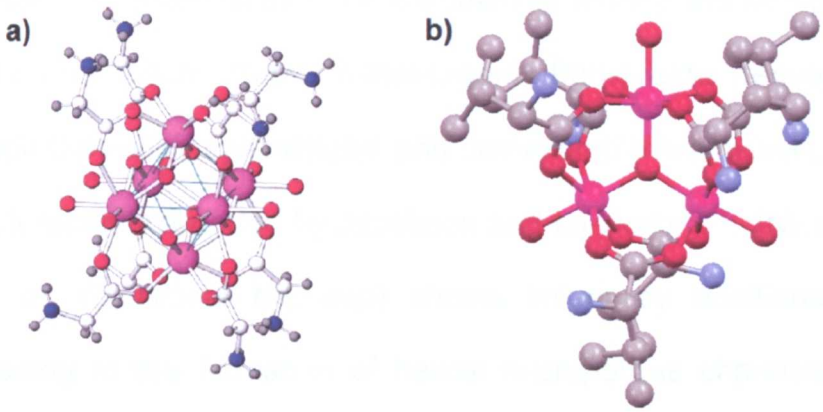

Figure 1.15. a) Hexanuclear Zr glycine cluster formed at low pH[49], and b) Trinuclear Cr cluster with valine, also formed at low pH.[48]

1.4.2 Amino acids in coordination polymers

Extended structures from amino acids have been previously synthesised with proline,[51,52] tyrosine,[53,54], threonine,[55] alanine,[55] tryptophan,[56] aspartic acid,[36,38-40,57] and glutamic acid.[42-45,58,59] In most cases, the structures are extended by formation of the N,O metallacycle, with the oxygen atom not involved in the chelation bridging to an adjacent metal ion. In the absence of any additional bridging ligands or coordinating moieties from the amino acid, this can lead to the formation of a 1D helical chain[52] (Figure 1.16a). In the presence of a bridging ligand, such as bipy, the dimensionality of the polymer can be extended to 2D (Figure 1.16b).[51] However, additional binding modes within the amino acid, can preclude the formation of the O–M bond from the C=O carboxylate oxygen, if more thermodynamically stable dimers are formed, as noted in $[Zn(L\text{-}Tyr)(H_2O)]$[53], where L-Tyr = L-tyrosine (Figure 1.16c). If low pH conditions are utilised in the synthetic conditions, this can modify the coordination modes by protonation of the amine group, preventing the formation of the N,O metallacycle. If combined with a suitable bridging ligand, this can lead to the formation of an extended coordination polymer (Figure 1.16d).[51]

In all of the examples given above, the frameworks formed are non-porous lacking any accessible void space. Porous metal-organic frameworks derived from amino acids have been previously synthesised, and one example is a nickel L-aspartate (L-asp) framework recently reported by Jacobson and co-workers[36]. $[Ni_{2.5}(OH)(L\text{-}asp)_2]$ is comprised of 1D helical Ni(L-asp) chains linked by additional $[Ni(L\text{-}asp)_2]$ octahedra, leading to the formation of helical microporous channels with a pore window of 8 *x* 5 Å. The framework was found to be permanently porous, as demonstrated by an N_2 isotherm, but does not display any chiral sorption properties.

Jacobson also reported a structurally related L-asp derived non-porous MOF, $[Ni_2O(L\text{-}asp)(H_2O)_2]$,[37] which is comprised of the same 1D helices noted within the porous $[Ni_{2.5}(OH)(L\text{-}asp)_2]$, however the absence of the additional $[Ni(L\text{-}asp)_2]$ octahedra leaves the 1D helices non-connected (Figure 1.17). The formation of the two frameworks can be directly controlled by adjusting the pH.

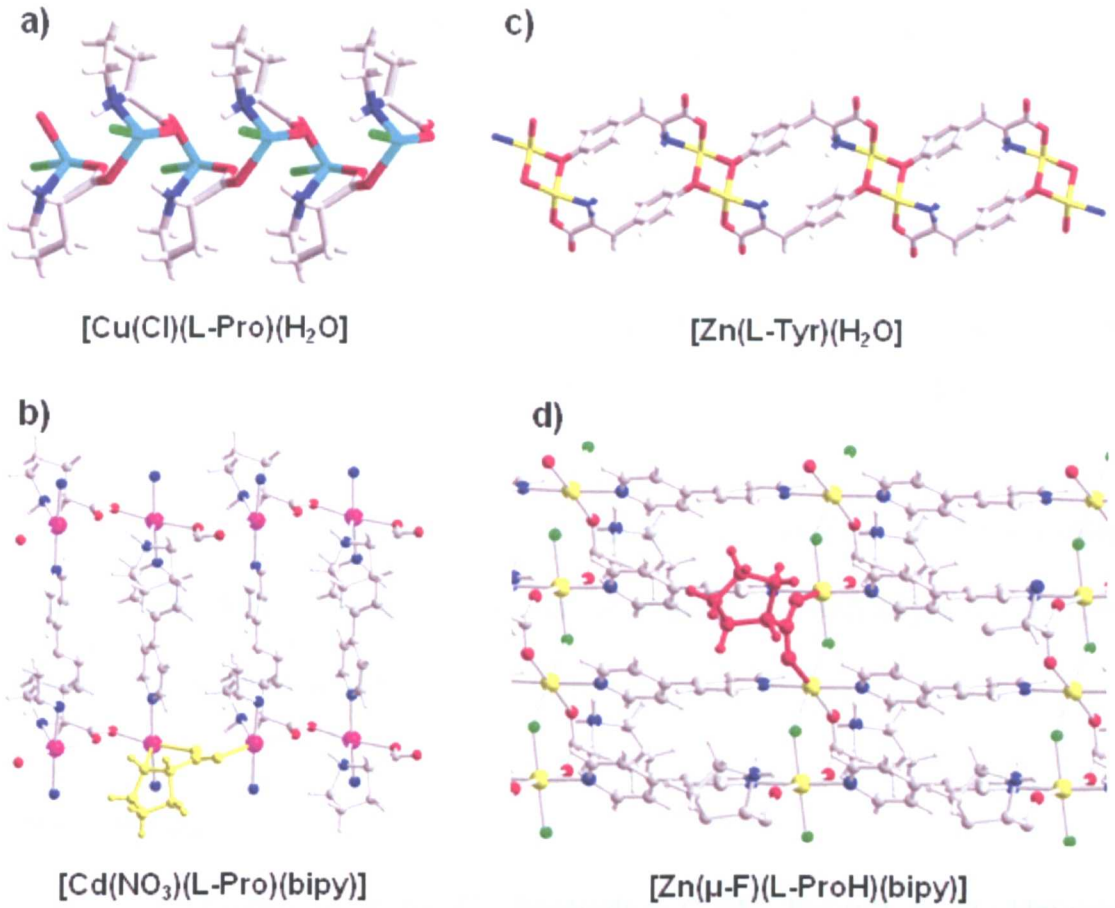

Figure 1.16. Examples of the amino acid coordination modes in MOFs. a) 1D polymer formed via 5-membered N,O chelation to M, with the second O from the carboxylate bridging to adjacent M. b) Addition of bridging bipy extends polymer to 2D. A single L-proline ligand is highlighted in yellow. c) Coordination from deprotonated phenolic side chain of L-Tyr prevents extension of polymer through formation of a Zn dimer. d) Protonation of amine group of L-proline (L-Pro) precludes metallacycle formation, and in the presence of F^- and bipy, leads to the formation of a Zn-proline/(μ-F) bridged chain, linked by bipy. A single L-proline ligand highlighted in red.

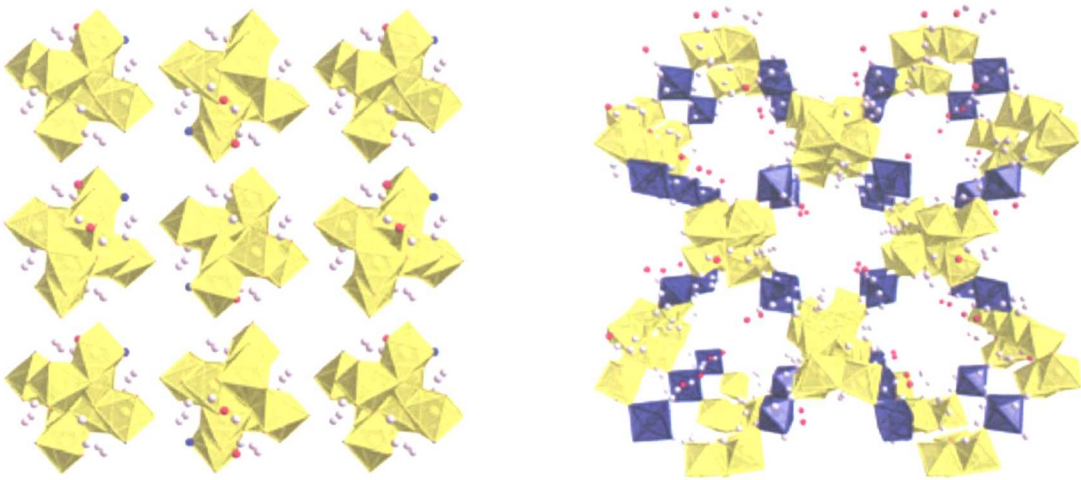

$[Ni_2O(L\text{-}Asp)(H_2O)_2]$
1D helical polymers – non-porous

$[Ni_{2.5}(OH)(L\text{-}Asp)_2]$
3D framework – porous

Figure 1.17. The two frameworks formed from Ni(L-asp). $[Ni_2O(L\text{-}Asp)(H_2O)_2]$ is 1D, and comprised of helical chains, whereas $[Ni_{2.5}(OH)(L\text{-}Asp)_2]$ consists of identical chains linked by additional $[Ni(L\text{-}asp)_2]$ octahedra (blue) to yield a 3D porous framework.

With 12 other chiral amino acids available for manipulation to form extended frameworks, there still remains a considerable amount of chemistry to be performed with these enantiopure ligands.

1.5 References

(1) Rouquerol, J.; Avnir, D.; Fairbridge, C. W.; Everett, D. H.; Haynes, J. M.; Pernicone, N.; Ramsay, J. D. F.; Sing, K. S. W.; Unger, K. K. *Pure & Appl. Chem.* **1994**, *66*, 1739-1758.

(2) Cheetham, A. K.; Ferey, G.; Loiseau, T. *Angew. Chem. Int. Ed.* **1999**, *38*, 3268-3292.

(3) Yu, J.; Xu, R. *J. Mater. Chem.* **2008**, *18*, 4021-4030.

(4) Treacy, M. M. J.; Newsam, J. M. *Nature* **1988**, *332*, 249-251.

(5) Corma, A.; Moliner, M.; Cantín, Á.; Díaz-Cabañas, M. J.; Jordá, J. L.; Zhang, D.; Sun, J.; Jansson, K.; Hovmölle, S.; Zou, X. *Chem. Mater.* **2008**, *20*, 3218-3223.

(6) Davis, M. E.; Saldarriaga, C.; C., M.; J., G.; C., C. *Nature* **1988**, *331*, 698-699.

(7) McCusker, L. B.; Baerlocher, C.; Jahn, E.; Bulow, M. *Zeolites* **1991**, *11*, 308-313.

(8) Anderson, M. W.; Terasaki, O.; Ohsuna, T.; Philippou, A.; MacKay, S. P.; Ferreira, A.; Rocha, J.; Lidin, S. *Nature* **1994**, *367*, 347-351.

(9) Sun, J.; Bonneau, C.; Cantín, Á.; Corma, A.; Díaz-Cabañas, M. J.; Moliner, M.; Zhang, D.; Li, M.; Zou, X. *Nature* **2009**, *458*, 1154-1157.

(10) Eddaoudi, M.; Kim, J.; Rosi, N.; Vodak, D.; Wachter, J.; O'Keeffe, M.; Yaghi, O. M. *Science* **2002**, *295*, 469-472.

(11) Li, H.; Eddaoudi, M.; O'Keeffe, M.; Yaghi, O. M. *Nature* **1999**, *402*, 276-279.

(12) Lin, X.; Jia, J.; Zhao, X.; Thomas, K. M.; Blake, A. J.; Walker, G. S.; Champness, N. R.; Hubberstey, P.; Schroder, M. *Angew. Chem. Int. Ed.* **2006**, *45*, 7358-7364.

(13) Lin, X.; Telepeni, I.; Blake, A. J.; Dailly, A.; Brown, C. M.; Simmons, J. M.; Zoppi, M.; Walker, G. S.; Thomas, K. M.; Mays, T. J.; Hubberstey, P.; Champness, N. R.; Schroder, M. *J. Am. Chem. Soc.* **2009**, *131*, 2159-2171.

(14) Millange, F.; Serre, C.; Férey, G. *Chem. Commun.* **2002**, 822-823.

(15) Ahnfeldt, T.; Gunzelmann, D.; Loiseau, T.; Hirsemann, D.; Senker, J.; Ferey, G.; Stock, N. *Inorg. Chem.* **2009**, *48*, 3057-3064.

(16) Bauer, S.; Serre, C.; Devic, T.; Horcajada, P.; Marrot, J.; Ferey, G.; Stock, N. *Inorg. Chem.* **2008**, *47*, 7568-7576.

(17) Biradha, K.; Seward, C.; Zaworotko, M. J. *Angew. Chem. Int. Ed.* **1999**, *38*, 492-495.

(18) Yaghi, O. M.; Davis, C. E.; Li, G.; Li, H. *J. Am. Chem. Soc.* **1997**, *119*, 2861-2868.

(19) Ezuhara, T.; Endo, K.; Aoyama, Y. *J. Am. Chem. Soc.* **1999**, *121*, 3279-3283.

(20) Kepert, C. J.; Prior, T. J.; Rosseinsky, M. J. *J. Am. Chem. Soc.* **2000**, *122*, 5158-5168.

(21) Kepert, C. J.; Rosseinsky, M. J. *Chem. Commun.* **1998**, 31-32.

(22) Bradshaw, D.; Prior, T. J.; Cussen, E. J.; Claridge, J. B.; Rosseinsky, M. J. *J. Am. Chem. Soc.* **2004**, *126*, 6106-6114.

(23) Lin, Z.; Slawin, A. M. Z.; Morris, R. E. *J. Am. Chem. Soc.* **2007**, *129*, 4880-4881.

(24) Seo, J. S.; Whang, D.; Lee, H.; Jun, S. I.; Oh, J.; Jeon, Y. J.; Kim, K. *Nature* **2000**, 982-986.

(25) Wu, C.-D.; Hu, A.; Zhang, L.; Lin, W. *J. Am. Chem. Soc.* **2005**, *127*, 8940-8941.

(26) Cho, S.-H.; Ma, B.; Nguyen, S. T.; Hupp, J. T.; Albrecht-Schmitt, T. E. *Chem. Commun.* **2006**, 2563-2565.

(27) Dybtsev, D. N.; Nuzhdin, A. L.; Chun, H.; Bryliakov, K. P.; Tals, E. P.; Fedin, V. P.; Kim, K. *Angew. Chem. Int. Ed.* **2005**, *45*, 916-920.

(28) McMurry, J. In *Organic Chemistry, Fourth Edition*; Brooks/Cole: **1996**, p1055-1059.

(29) Archibald, S. J. In *Comprehensive Coordination Chemistry II Vol 2*; Pergamon: **2004**; p1147-1252.

(30) Bell, P.; Sheldrick, W. S. *Z. Naturforsch.* **1984**, *39b*, 1732-1737.

(31) Newman, J. M.; Bear, C. A.; Hambley, T. W.; Freemann, H. C. *Acta Cryst.* **1990**, *C46* 44-48.

(32) Stosick, A. J. *J. Am. Chem. Soc.* **1945**, *67*, 365-370.

(33) Wilson, R. B.; de-Meester, P.; Hodgson, D. J. *Inorg. Chem.* **1977**, *16*, 1498-1502.

(34) Subramanian, P. S.; Suresh, E.; Dastidar, P.; Waghmode, S.; Srinivas, D. *Inorg. Chem.* **2001**, *40*, 4291-4301.

(35) Ama, T.; Rashid, M. M.; Sarker, A. K.; Miyakawa, H.; Yonemura, T.; Kawaguchi, H.; Yasui, T. *Bull. Chem. Soc. Jpn.* **2001**, *74*, 2327-2333.

(36) Anokhina, E. V.; Go, Y. B.; Lee, Y.; Vogt, T.; Jacobson, A. J. *J. Am. Chem. Soc.* **2006**, *128*, 9957-9962.

(37) Anokhina, E. V.; Jacobson, A. J. *J. Am. Chem. Soc.* **2004**, *126*, 3044-3045.

(38) Antolini, L.; Menabue, L.; Pellacani, G. C.; Marcotrigiano, G. *Dalton Trans.* **1982**, 2541–2543.

(39) Kryger, L.; Rasmussen, S. E. *Acta Chem. Scand.* **1973**, *27*, 2674-2676.

(40) Schmidbaur, H.; Bach, I.; Riede, J.; Muller, G.; Helbig, J.; Hopf, G. *Chem. Ber.* **1988**, *121*, 795-797.

(41) Antolini, L.; Marcotrigiano, G.; Menabue, L.; Pellacani, G. C.; Saladini, M.; Sola, M. *Inorg. Chem.* **1985**, *24*, 3621-3626.

(42) Flook, R. J.; Freeman, H. C.; Scudder, M. L. *Acta Crystallogr B* **1977**, *B33*, 801-809.

(43) Gramaccioli, C. M. *Acta Cryst.* **1966**, *21*, 600–605.

(44) Gramaccioli, C. M.; Marsh, R. E. *Acta Cryst.* **1966**, *21*, 594–600.

(45) Zhang, Y.; Saha, M. K.; Bernal, I. *CrystEngComm* **2003**, *5*, 34–37.

(46) Palmer, R. A.; Meredith, P. L. *Inorg. Chem.* **1971**, *10*, 1049-1056.

(47) Clegg, W.; Lam, O. M.; Straughan, B. P. *Angew. Chem. Int. Ed. Engl.* **1984**, *23*, 434-435.

(48) Kato, H.; Nakata, K.; Nagasawa, A.; Yamaguchi, T.; Sasaka, Y.; Ito, T. *Bull. Chem. Soc. Jpn* **1991**, *64*, 3463-4365.

(49) Pan, L.; Heddy, R.; Li, J.; Zheng, C.; Huang, X.-Y.; Tang, X.; Kilpatrick, L. *Inorg. Chem.* **2008**, *47*, 5537-5539.

(50) Puri, R. N.; Asplund, R. O. *Inorg. Chim. Acta.* **1981**, *54*, L187-L190.

(51) Ingleson, M. J.; Bacsa, J.; Rosseinsky, M. J. *Chem. Commun.* **2007**, 3036-3038.

(52) Yukawa, Y. *J. Chem. Soc. Dalton Trans.* **1992**, 3217-3221.

(53) Li, D.-Q.; Zhou, J.; Liu, X. *Acta Cryst.* **2007**, *C63*, m371-m373.

(54) Weng, J.; Hong, M.; Shi, Q.; Cao, R.; Chan, A. S. C. *Eur. J. Inorg. Chem.* **2002**, 2553-2556.

(55) Loua, B.-Y.; Wanga, R.-H.; Yuana, D.-Q.; Wua, B.-L.; Jiang, F.-L.; Hong, M.-C. *Inorg. Chem. Commun.* **2005**, *8*, 971-974.

(56) Wisser, B.; Lu, Y.; Janiak, C. *Z. Anorg. Allg. Chem.* **2007**, *633*, 1189-1192.

(57) Doyne, T. H.; Pepinsky, R.; Watanabe, T. *Acta Cryst.* **1957**, *10*, 438-439.

(58) Gutschke, S. O. H.; Price, D. J.; Powell, A. K.; Wood, P. T. *Inorg. Chem.* **2000**, *39*, 3705-3707.

(59) Lu, T.; Li, X.; Mao, Z.; Qiu, W.; Ji, L.; Yu, K. *Polyhedron* **1998**, *17*, 75–79.

Chapter 2 Synthetic and experimental techniques

2.1 Introduction

The aim of this chapter is to give an overview of the techniques utilised in the synthesis and characterisation of the amino acid derived metal-organic frameworks (MOFs), and the synthetic precursors presented in this thesis. Particular attention is upon the different types of synthetic procedures utilised and the equipment used to characterise the materials. Due to the crystalline nature of MOFs, the most widely used techniques were diffraction based, with powder X-ray diffraction (PXRD) used routinely to determine whether the formed products are crystalline in nature, and whether these products are phase pure. In order to determine the structure of the materials, single crystal X-ray diffraction was performed using laboratory sources and synchrotron radiation.

The bulk chirality of the amino acid derived frameworks was determined using chiral gas chromatography (GC), which was performed on a derivatised form of the amino acid used in the synthesis, isolated from a sample of the bulk material.

Thermogravimetric analysis (TGA) was used to determine the decomposition temperatures of the frameworks, and the temperature range in which guest molecules are removed from the internal surface, and the ability of the MOFs to adsorb gases, such as N_2, H_2 and CO_2 were determined using intelligent gravimetric analysis (IGA). The effects of guest loss and the adsorption of different gases upon the crystallinity of the frameworks were monitored using PXRD.

The high-pressure crystallography experiments performed in Chapter 5 were performed using diamond anvil cells (DAC), to apply the pressure, and the diffraction was measured using synchrotron radiation.

2.2 Synthetic Techniques

The synthesis of MOFs is concerned with the growth of a crystalline array of metal-ligand combinations in the form of single crystals or microcrystalline powders. Typically the growth of single crystals suitable for diffraction is a slow process taking between minutes and months, and can be conducted using a variety of methods including diffusion, slow evaporation and controlled cooling.[1] If microcrystalline powders are desired, the synthesis can be altered by increasing concentration, temperature or by direct mixing of the components. In addition to these methods, metal-organic frameworks can be synthesised using solvothermal synthesis, and the majority of the frameworks within this thesis are produced using this method.

2.2.1 Principles of solvothermal synthesis[2-4]

Solvothermal synthesis is typically concerned with homogeneous reactions within sealed autoclaves above room temperature and 1 bar, with autogeneous pressure due to the gas/liquid equilibrium within the reactor. The pressure within the sealed reactor is controlled by the vapour pressure, which increases with temperature, due to the solvent expanding. The increasing temperature also affects other properties of the solvent, lowering the dielectric constant of the solvent and increasing the dissociation constant of ionising species within the reactor, such as carboxylic acids, water and methanol. This allows the solubilisation of species that are typically insoluble at ambient pressure, and gives a greater degree of control over the reaction. Other variables to note within the synthesis are the heating and cooling rates, and also the time at maximum temperature, as depending upon how the crystals form within the reactor, any or all of these factors could have a direct influence over the purity and yield of formed material. The reactors used within this

thesis were supplied by Parr, made of steel with PTFE (Teflon) inserts of volume = 23ml (Figure 2.1). The temperature range used within synthetic exploration was between 80 and 200 °C, with filling percentages between 10 and 50%, to ensure that expansion of the solvent does not cause rupture of the reactor. Typical heating rate in use was 2 °C min^{-1}, and cooling rates varied from 0.1 – 2 °C min^{-1}, depending on the effect upon crystallisation.

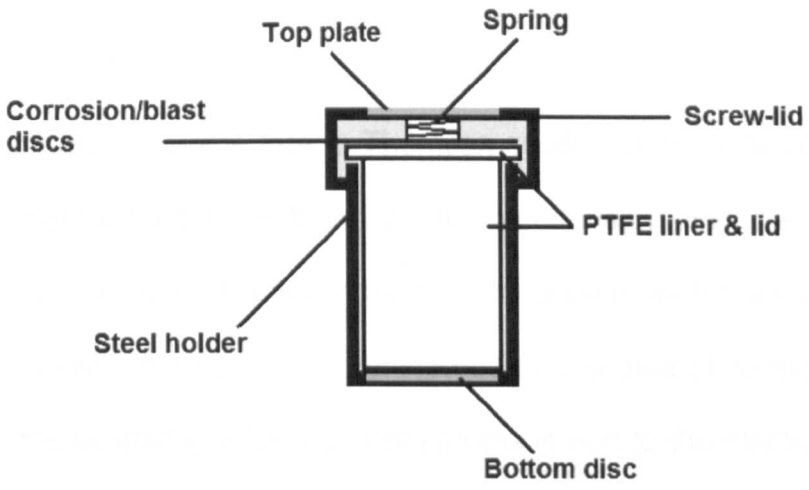

Figure 2.1. A schematic diagram of the PTFE lined solvothermal autoclave used in synthesising frameworks in this thesis.

2.3 X-ray diffraction

In order to understand the structure-property relationships within materials, knowledge of the structure is of vital importance. This was achieved within this thesis using single crystal X-ray diffraction. Several texts that describe these methods in detail already exist;[5,6] therefore a brief introduction to the method follows.

2.3.1 X-ray scattering

X-rays are scattered by atoms due to Thomson scattering, the interaction between the oscillating electric field of the X-ray and the electrons orbiting the nucleus of the atom. This causes the electrons within the atom to oscillate with the same frequency as the incident radiation, and can be considered to a source of X-rays of the same frequency. As the scattering of X-rays from atoms is due to the electrons within the atom, elements with increasing number of electrons, and hence atomic number, scatter X-rays to a greater degree.

2.3.2 Principles of X-ray diffraction

Crystals consist of a periodic array of atoms or molecules. Diffraction occurs within crystals, due to their inherent ability to act as diffraction gratings when in contact with X-rays, which have a wavelength on same scale as interatomic spacing. When X-rays have been passed through a crystal, the result is a diffraction pattern, comprised of a geometric array of reflections, which is determined by the symmetry of the crystal structure.

The position of the reflections within the diffraction pattern can be related to the unit cell parameters using the Bragg condition, which is based upon the construct that the interaction between X-rays and crystals behave like waves reflecting off a series of parallel planes of atoms defined by Miller indices (*hkl*), when the angle of incidence is equal to the angle of reflection. If the spacing between the planes is equal to a multiple of the wavelength of the X-ray radiation, then the waves will be in phase, as given by Bragg's Law:[7]

$$n\lambda = 2d_{hkl} \sin \theta_{hkl}$$

Equation 2.1

Where n is a positive integer λ = the wavelength of radiation, d_{hkl} = the plane spacing, and θ = the incident/reflection angle between the X-ray beam and the atomic plane. This can also be viewed schematically in Figure 2.2.

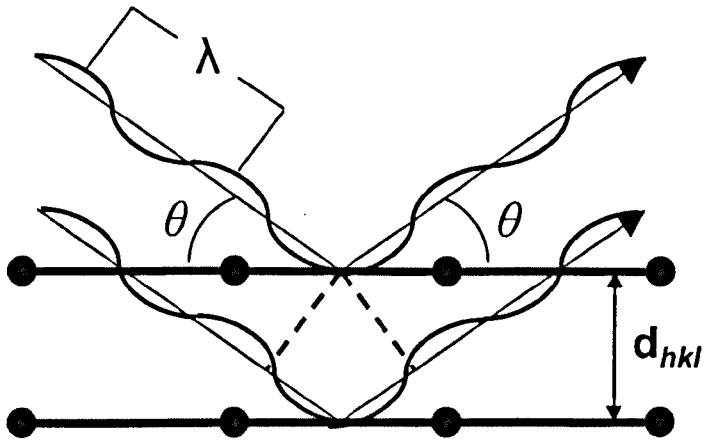

Figure 2.2. Schematic of the Bragg condition.

Bragg's Law allows a geometric interpretation of the diffraction pattern, to yield a set of unit cell parameters. This information combined with the missing reflections within the diffraction pattern arises from systematic absences due to symmetry elements within the unit cell. These are due to translational symmetry operations, such as glide planes, screw axes, or lattice centring, and allows the determination of the space group. Therefore, the entire symmetry of the unit cell can be determined through the measurement of the geometric location of the reflections. However, in order to determine the coordinates of each individual atom within the structure, we need to utilise the information contained within the intensity data of each reflection.

2.3.3 The intensity of X-rays

The measured intensity of each reflection is given by the formula:

$$I_{hkl} = cLp|F_{hkl}|^2$$

Equation 2.2

Where I_{hkl} is the observed intensity of the reflection, *hkl*, *c* is a constant scale factor, *L* is the Lorentz factor, which is dependent upon the way in which the instrument sweeps through 2θ, *p* is a polarisation correction factor, and $|F_{hkl}|$ is the modulus of the structure factor of the reflection, *hkl*.

The structure factor, $F(hkl)$ directly relates the fractional coordinates of the individual atoms within the unit cell to the observed intensities, and hence is dependent solely upon the crystal structure, and is given by the following formula:

$$F(hkl) = \sum_{j=1}^{N} f_j \exp[2\pi i(hx_j + ky_j + lz_j)]$$

Equation 2.3

Here, the position of atom j, which has a scattering factor f_j, is given by the fractional coordinates (x_j, y_j, z_j.). There are N atoms within the unit cell.

Each structure factor represents a diffracted beam, which has an amplitude and a relative phase, as represented by the following formula, where $\varphi(hkl)$ is the phase of the structure factor:

$$F(hkl) = |F(hkl)| \cdot \exp[i\varphi\,(hkl)]$$

Equation 2.4

Therefore, the experimental intensity data are missing the information for the relative phases of each reflection, which is essential to calculate the electron density of each reflection, as denoted by the formula, where $\rho(xyz)$ is the electron density at coordinated xyz:

$$\rho(xyz) = \frac{1}{V} \sum_{hkl} F(hkl) \exp\,\mathrm{i}[-2\pi(hx + ky + lz)]$$

Equation 2.5. The Fourier transformation of the electron density.

This missing data is known as the phase problem.

The phase problem is generally overcome using one of two methods, Patterson synthesis and direct methods. In a Patterson synthesis, the Fourier transform is completed using the square of the observed structure factors| F_o^2|, with all of the phases set equal to zero, leading to a Patterson map, which is a map of vectors between pairs of atoms in the structure. The second method, Direct methods, which approximates the reflection phases from the measured intensities, by selecting the reflections which contribute most to the original Fourier transform, and working out the relationships between them. The generated electron density map is then examined, with the electron density corresponding to familiar molecular features assigned as atomic positions. The next step is to calculate the reflection intensities (F_c), using the phase information from the designated electron densities, and to compare with the observed reflection intensities (F_o), using least squares refinement against F^2 for all reflections. This can be achieved using several different figures of merit such as the residual-factor (*R*-factor), the weighted *R*-factor and the Goodness of fit. These are expressed in equations 2.6-2.8:

$$R = \frac{\sum[|F_o| - |F_c|]}{\sum |F_o|}$$

Equation 2.6. The residual-factor, or *R*-factor. A complete crystal structure from good quality data will have an *R*-factor between 0.02-0.07. The subscripts o and c correspond to the observed and calculated values respectively.

$$wR_2 = \sqrt{\frac{\sum(w(F_o^2 - F_c^2)^2)}{\sum w(F_o^4)}}$$

Equation 2.7. The weighted residual-factor, which is based upon F^2; *w* corresponds to the weight for each reflection.

$$S = \frac{\sum(w(F_o^2 - F_c^2)^2)}{\sqrt{n-p}}$$

Equation 2.8. The goodness of fit (GooF), S, which is expressed in terms of the weighted squared observed and calculated reflections, *n*, and the number of parameters.

If the *R*-factor is high, and not all of the atoms have been located, a new electron density map can be generated by performing a Fourier transform with the experimental amplitudes and the calculated phases from the last cycle of refinement. This new electron density map can then be used to once more allocate familiar molecular features, and the refinement process repeated until the *R*-factor is sufficiently below 10% and the thermal parameters of the atoms, and the estimated standard deviation of the bond lengths are sensible.

2.3.4 Powder X-ray diffraction (PXRD)[6]

Unlike single crystal diffraction where each reflection produces a single spot in the diffraction pattern, the data from PXRD is comprised of many reflections arising from randomly orientated polycrystallites, each of which give a diffraction pattern when a beam of X-rays are incident upon the sample. These reflections overlap leading to the appearance of rings in the diffraction pattern (Figure 2.3). In a typical powder diffraction experiment, the intensity of the diffracted beam is measured as a function of 2θ in one dimension, leading to a pattern of lines, each of which correspond to a single reflection. As with single crystal structure analysis, the reflection positions can be used to determine the unit cell of the crystal structure. In addition, comparable to single crystal, the data within these reflections contain the information of the

atomic/molecular arrangement within the unit cell, however, due to the overlapping reflections, the 3-dimensional data are only available within 1-dimensional space.

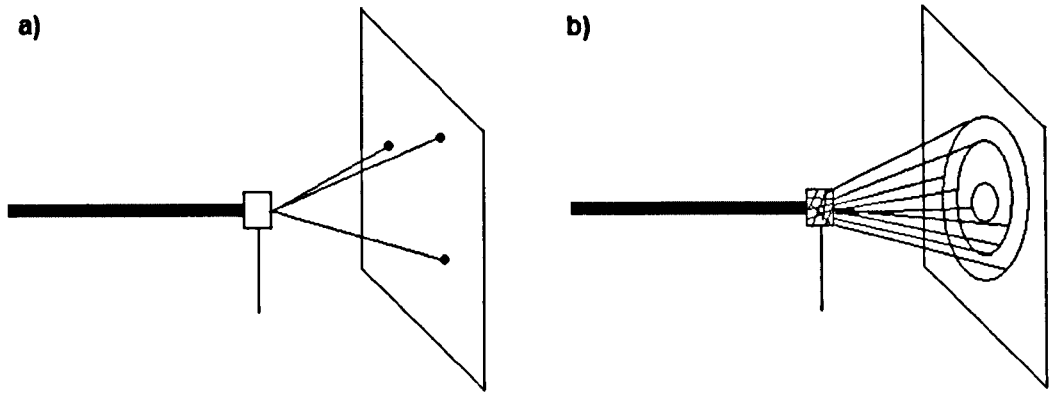

Figure 2.3. a) Single crystal diffraction leads to the generation of single reflections in the diffraction pattern, whilst in powder diffraction, b) the reflections from the polycrystalline sample overlap to lead to the generation of rings in the diffraction pattern.

Powder diffraction methods can be used for structure solution, and in particular, the Rietveld method[8,9] is regularly employed. This method relies upon refining the cell parameters and peak profiles against calculated structure factors data, which are determined from a structural model, using least-squares refinements.

Within this thesis, PXRD was used as a method for phase determination of samples, and also to determine phase purity using the LeBail method,[10,11] with the program FULLPROF.[12] The LeBail method, unlike the Rietveld method, does not employ the use of a structure model, and refines the position and intensity of the reflections from the observed data against a constant structure factor.

2.3.5 High-pressure single crystal diffraction

The high-pressure single crystal diffraction work described in Chapter 5 was carried out using Merrill-Basset Diamond Anvil Cells (DAC),[13] in collaboration with the

University of Edinburgh. The cells are comprised of two steel plates held together with three screws. In the middle of two plates, are two backing disks, two diamond anvils and a tungsten gasket (Figure 2.4).

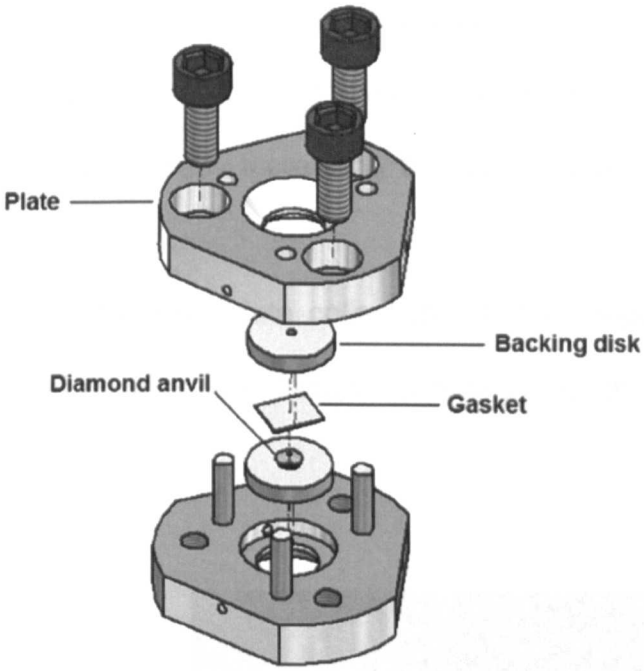

Figure 2.4. The Schematic of a Merrill-Bassett diamond anvil cell (DAC)

In the centre of the gasket, a single crystal of the material under study is placed along with a ruby crystal, which acts as a fluorescent probe for pressure measurement by Raman spectroscopy.[14] In order to apply uniform pressure, hydrostatic media, consisting of a compound that stays fluidic throughout the application of pressure, typically comprised of either a 16 : 3 : 1 volumetric mixture of MeOH : EtOH : H_2O, or a 1 : 1 volumetric mixture of pentane : isopentane, depending upon the reactivity, or the solubility of the material under study.

Once sealed, the DAC can be fixed on to a goniometer head and diffraction intensities can be measured. However, due to the small size of the opening angle at

the top of the DAC, and the geometry of the goniometer, the possible number of reflections that can be collected is restricted, having a direct effect upon the completeness of the data. In addition to these problems, the crystal size has to be small, in order to fit within the sample chamber, and the resulting diffraction is partially masked from absorption from the backing seats, reducing the intensity of the measured reflections. Some of these problems can be overcome by using short wavelength X-rays (≤0.5Å), thereby increasing the size of the available reciprocal space available.

Further problems amount from the data collection, as the images contain intense diamond reflections, and powder lines from the backing seat and gasket materials (Figure 2.5).

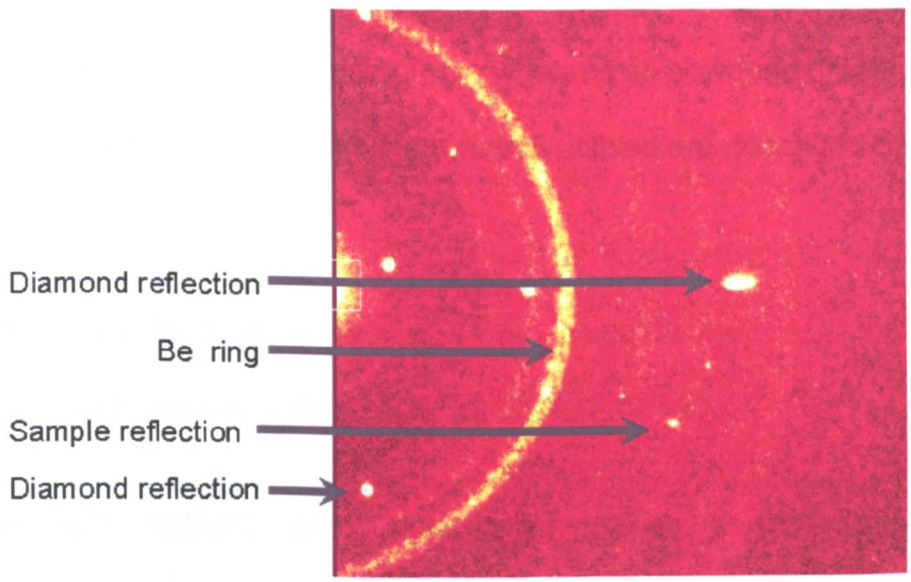

Figure 2.5. Example of the different reflections within a single frame of data from a high-pressure data collection.

The extra reflections can be resolved in two ways; firstly by the use of twin indexing software, such as CELL_NOW,[15] or by indexing only the sample reflections by selecting the appropriate reflections using a reciprocal lattice viewer, such as

RLATT. In addition, the integration of the high-pressure data also needs to take into account the reduced amount of reciprocal space due to shading of the DAC. This problem has been solved by the use of masks by Dawson et al,[16] which take into account these regions of the detector that are shaded during the integration process.

The specific protocol for data collection, integration, and the pressures used are provided in Chapter 5. CIF data for all solved structures is supplied on a DVD attached to this thesis.

2.3.6 X-ray diffractometers

Single crystal X-ray diffraction data was collected using either conventional laboratory sources, or a synchrotron source, whereas all powder diffraction data was collected on laboratory sources. The instruments utilised are described below.

2.3.7 Single crystal diffractometers

2.3.7.1 Bruker AXS SMART APEX

The Bruker AXS SMART APEX instrument utilises a CCD area detector diffractometer. The X-rays are generated using graphite monochromated Mo Kα radiation from a molybdenum X-ray tube operating at 40kV and 30 mA. Typically samples were mounted in oil on a fibre loop, which is magnetically attached to a 3-axis goniometer. It is equipped with an Oxford Cryosystems nitrogen stream setup, and data collections were typically performed between 150K and room temperature

following flash cooling of the crystals. Methods for integration and refinement are noted within the CIF files.

2.3.7.2 Daresbury Laboratory SRS Station 9.8[17]

The synchrotron radiation source (SRS) at Daresbury was a UK based synchrotron, until its closure in 2008. It is comprised of a Linac gun which generates electrons, and injects them into the booster ring, where they are accelerated close to the speed of light. The electrons are then injected into a storage ring, where they are kept within a by a series of magnets, and upon passing through each magnet, the momentum of the electron beam is changed, emitting synchrotron radiation, of much higher intensity than standard laboratory sources. Although the wavelengths can be altered, station typically operated at a wavelength of approximately 0.69 Å.

Single crystal diffraction data were collected using a Bruker-Nonius APEXII CCD area detector diffractometer fitted with an Oxford Cryosystems Cryostream 700+ series, capable of cooling crystals down to 85K. Samples were mounted on the end of a two stage glass fibre, and typically measured at 150 or 100K following flash cooling of the crystals. In standard data collections, a hemisphere of data in reciprocal space was collected, and modified depending upon the crystal system of the structure. Methods for integration and refinement are noted within the main text.

2.3.8 Powder diffractometers

2.3.8.1 Stoe STADI-P diffractometer

Samples collected within this instrument were loaded into 0.5mm glass capillaries, and collected in Debye-Scherrer geometry by a linear 6.5 ° PSD (Position Sensitive Detector) using a monochromated copper X-ray source. Capillaries were rotated about their central axis during data collection, minimising any potential effects from preferred rotation. The diffractometer was controlled using Stoe WinXPOW software (version 1.19). Measurements for phase identification were performed with a step size of 0.5° at a rate of 30 sec/step, and measurements for Le Bail fitting were measured with a step size of 0.1° at a rate of 120 sec/step. All measurements were performed at room temperature, unless otherwise indicated.

2.4 Gravimetric analysis

Gravimetry can be used to study the changes within the structures of MOFs upon the effect of temperature, or in the presence of gases at different pressures. Detailed information about the loss of encapsulated guest molecules and volatile ligands, in terms of their lability can also be obtained with this method, and it also gives information on the purity of the bulk material and the decomposition temperature. Prior to analysis, samples were filtered from the mother liquor and dried in air, with the surface bound guest molecules removed by rinsing with a volatile solvent, such as methanol.

2.4.1 *Thermogravimetric analysis*

Thermogravimetric data were recorded on a Seiko Instruments EXSTAR TG/DTA 6030. Solid samples of approximately 10 mg were loaded into a platinum pan, and heated, and cooled at a rate of 5 °C min^{-1}, unless otherwise stated in a flow of nitrogen at a rate of 80 ml min^{-1}. When structural integrity upon guest loss was determined, samples were heated to the temperature at which mass loss initially occurs and held at that temperature for one hour to ensure all guest is lost, and cooled at the standard rate to room temperature. PXRD was then measured upon this sample.

2.4.2 *Adsorption measurements*

The measurement of isotherms reflects the ability of a porous material to interact with adsorbates, leading to physisorption directly upon the interior, or exterior surface. There are six different types of sorption defined by IUPAC,[18] which have different characteristics, distinguishable upon the shape of the plot of relative pressure *vs* the amount adsorbed (Figure 2.6).

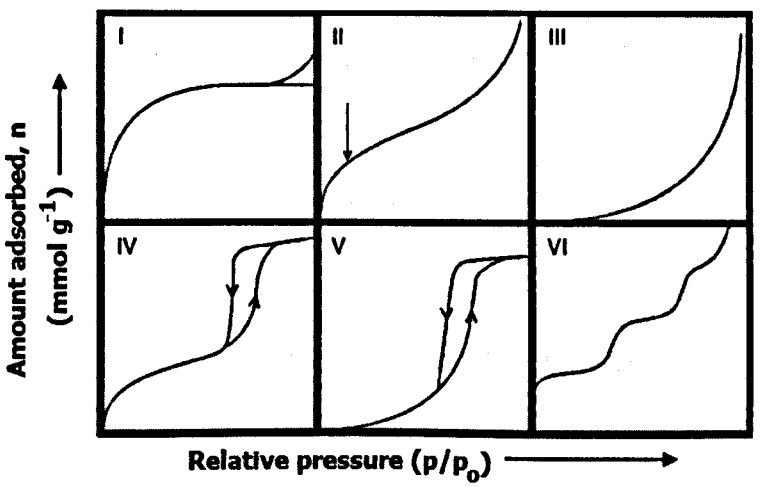

Figure 2.6. The shapes of the six different types of isotherms, as classified by IUPAC.

The following information can be obtained from these different types of isotherms:

Type I – Solid is microporous, with pores less than 2 nm.

Type II – Solid is either non-porous, or macroporous with pores larger than 50 nm. In case of non-porous solids, physical adsorption of gases is on external surface. For macroporous solids, adsorption takes the form of a monolayer followed by multilayer coverage.

Type III – Weak interactions between solid and adsorbate. Interactions increase once primary adsorption sites are occupied, as adsorbate-adsorbate interactions are stronger.

Type IV – Solid is potentially mesoporous, with pore size between 2 and 50 nm. The hysteresis within the isotherm is typically associated with capillary condensation within the mesopores.

Type V – Solid is microporous, or mesoporous, with weak adsorbate-adsorbent interactions.

Type VI – Complete formation of monomolecular layers before progression to a subsequent layer

The materials within this thesis are classed as microporous, with pore sizes less than 2nm, and display either type I, or type II adsorption behaviour, depending upon whether the material is permanently porous.

To determine the amount of gas adsorbed into the materials presented within this thesis, data were recorded on a Hiden IGA gravimetric sorption balance at 198 K, unless otherwise stated. Prior activation of samples was carried out at 120 °C overnight at 10^{-7} mbar. The obtained data is expressed as the total amount of guest

adsorbed, quoted as a percentage change in the mass measured at complete desorption.

2.4.2.1 Determination of surface area

The surface area of a porous material is a measure of the internal area that is available to interact directly with the adsorbate. This is of particular interest, as increasing surface area gives a greater number of sites for guest adsorption, allowing access to the chemistry of the internal pores.

Within microporous and mesoporous materials, such as MOFs, the surface area of is typically determined using the Brunauer-Emmett-Teller (BET) model,[19] which is an extension of the Langmuir model,[20] taking into account multi-layer adsorption.

The BET equation is defined as:

$$\frac{p}{\left[\frac{n}{p_0 - p}\right]} = \frac{1}{(n_M c)} + \frac{(c-1)}{(n_M c)} x \frac{p}{p_0}$$

Equation 2.9

Where, p_0 = the saturation vapour pressure, n = the uptake, at pressure p, expressed as a molar quantity ($mmolg^{-1}$), n_m = the complete monolayer coverage, expressed as a molar quantity, ($mmolg^{-1}$), and c = a constant dimensionless quantity.

The surface area of $[Zn_2(IDS)(bipy)]$, determined within Chapter 3 was determined by plotting: $\frac{p}{n[p_o-p]}$ vs $\frac{p}{p_o}$, in the P/P_o range 0.01-0.27 using individual 26 points.

The plot was linear, with the gradient defined by $\frac{(c-1)}{(n_m c)}$, and an intercept of $\frac{1}{(n_m c)}$.

The values of c and n_m is then solved by multiplying the intercept and the gradient together to give $(c - 1)$, which can then be used to give n_m. Finally, the surface area, S ($m^2\ g^{-1}$) can be determined using n_m, the Avogadro's constant, N_A, and the area occupied by one molecule, A_m, using the equation:

$$S = n_m N_A A_m$$

Equation 2.10

2.5 Gas chromatography (GC)[21]

Chromatography is a separation process consisting where a compound mixture is combined with a mobile phase, which in the case of GC is an inert carrier gas, such as He, and is passed through a stationary phase. This is typically a solid, which interacts with the individual components of the mixture with differing strengths, leading to separation as the mobile phase is passed through the column. The stationary phases used in chiral separations are typically cyclodextrin based, comprised of five or more D-(+)-glucose units covalently linked together in a ring, with the cyclodextrin type determined by the number of units within the ring. This intrinsically chiral column provides recognition between one enantiomer over its opposite, with the separation increasing with the column length, analogous to liquid chromatography.

All chiral GC analyses were performed on a Shimadzu GC-148 chromatogram, using a Lipodex-E capillary-GC column at 120 °C, with He as the carrier gas. In order to increase the volatility of the amino acids, derivatisation by reaction with trifluoroacetic anhydride (TFA) carried out beforehand. This procedure is described within the main text, and by Rosseinsky et al.[22]

2.6 Spectroscopic techniques

2.6.1 Infra-red spectroscopy

Infra-red (IR) spectroscopy is concerned with the absorption of energy, resulting in a change of the electronic dipole moments within a molecules, from the displacement of atoms. In the study of glutamic acid based metal-organic frameworks in chapter 4, IR spectroscopy was used to determine whether glutamic acid had been incorporated within the material, and to identify the binding modes of glutamic acid to the metal centre, through identification of the symmetric (ν_{sym}) and asymmetric (ν_{asym}) carboxylate stretches within the amorphous material. A small selection of the potential binding modes on carboxylates to M are shown in Figure 2.7, each of which have a symmetric, and an asymmetric stretch, and a specified shift between them within the spectra, which varies systematically depending upon the coordination modes.[23,24] Therefore, by assigning both the ν_{sym}, and ν_{asym} stretches, it was possible to ascertain the coordination even within an amorphous material.

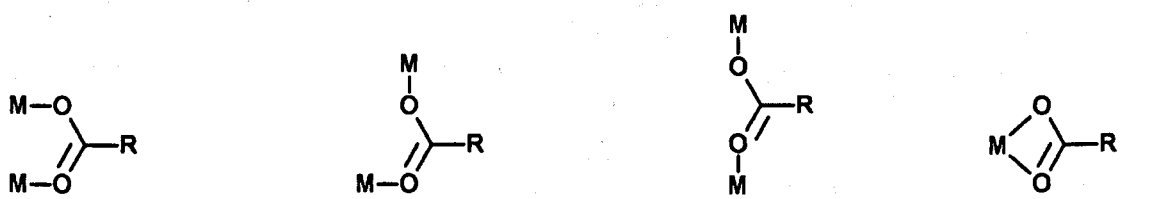

Figure 2.7. A selection of the different coordination modes of carboxylate groups to M.

IR spectra were collected using a PerkinElmer Spectrum 100 FTIR Spectrometer in the range of 600 – 4000 nm^{-1} using the attenuated total reflectance (ATR) technique, which allows direct measurement of solids or liquid samples without any further modification, as the sample is placed directly on a diamond crystal for measurement.

2.6.2 UV-Vis spectroscopy

The study of UV-Vis spectroscopy within transition metal complexes relates to the electronic structure, specifically the energy in *d-d* transitions. These effects are controlled by the ligands associated with the metal centre, in terms of the ligand field, and the geometry of the *d*-metal centre, which correspond to the crystal field splitting pattern. In effect, the measurement of the electronic spectra of transition metal complexes can give valuable information about which ligands are coordinated to the metal centre. This technique was utilised in Chapter 4, to identify the ligands associated with the nickel glutamate complex as-synthesised, and upon addition of pyridine.

The UV-Vis spectra were collected on a PerkinElmer Lambda 650 S UV-VIS spectrometer. Liquid samples were prepared by filling a cell of width 1 cm with a solution of known concentration (0.1M) Solid state samples were measured in reflectance mode, and samples were prepared by grinding into a fine powder and placing on to the cell window. The brass sample holder was then tightened to yield a thin film of powder in the window.

2.6.3 NMR spectroscopy

2.6.3.1 Nuclear magnetic resonance

NMR spectroscopy is concerned with the study of nuclei which possess angular momentum, known as spin, denoted *I*. If the spin of a nucleus is greater than 0, the nucleus is intrinsically magnetic, and can interact with magnetic fields. The amount of spin arises from unpaired protons and neutrons within the nucleus, and can be predicted from the number of protons and neutrons within the nucleus, according to the following rules:

1. If the number of protons and neutrons are both equal, the total spin will be equal to zero.
2. If the number of protons and neutrons are both odd, the spin will be a positive integer.
3. If the number of protons is even, but the number of neutrons is odd, the spin takes fractional values of $\frac{1}{2}$, or $\frac{3}{2}$, or $\frac{5}{2}$ etc...
4. If the number of protons is odd, but the number of neutrons is even, the spin takes fractional values of $\frac{1}{2}$, or $\frac{3}{2}$, or $\frac{5}{2}$ etc...

The spin angular momentum is a vector quantity and is space-quantised, only able to exist in $2I + 1$ orientations. In the absence of a magnetic field, the magnetic moment can exist in any of these orientations, and are hence degenerate. However, upon application of a magnetic field, the spin aligns in the field direction and the orientations are no longer degenerate, and are split into distinct energy levels, with the separation on the same scale as radiofrequency.

2.6.3.2 Origin of the chemical shift

In addition to the magnetic effects from the nucleus, the movements of electrons orbiting the nucleus induces a magnetic field in the opposite direction to the applied magnetic field, shielding the total magnetic field affecting the nucleus. This effect also occurs within molecules, with electrons in neighbouring atoms also affecting the magnetic field 'felt' by the nucleus. This is the origin of the chemical shift within NMR spectra, which is expressed in the dimensionless term ppm, and allows the determination of functional groups and quantitative knowledge of the structure of organic/organometallic compounds.

2.6.3.3 Anisotropy in chemical shifts

However, the distribution of electrons within most molecules is typically unsymmetrical, affecting the formation of the induced magnetic field, and is dependent upon the orientation of the molecules within the applied magnetic field. Within solution-state NMR, the random movement of molecules averages this effect out to average the orientations of the molecule, which correspond to single intense chemical shifts in the spectra. Within solid-state NMR, the molecules are fixed in space with only small vibrations possible, removing the averaging of orientations and leading to a spread of energy levels, and broad chemical shifts in the spectra. In order to counter this effect, in solid-state NMR, magic angle spinning (MAS) is used, in which the nuclei are spun around an axis inclined at an angle of 54.74° (the magic angle). This has the effect us reducing the orientation effects described above to zero, as they are controlled by the equation $3\cos^2\theta - 1$ (which when $\theta = 54.74° = 0$). Within this thesis, solid state NMR was used in the characterisation of [Zn(asp)]

within chapter 3. The technique was used to confirm the presence of multiple binding modes of aspartate within the framework, which had been determined by single crystal X-ray diffraction.

Cross polarisation (CP) was used during the data collection in order to enhance the signal of the low abundance ^{13}C nuclei present within the sample by transferring the magnetisation from the more abundant ^{1}H nuclei. Within the data collection for [Zn(asp)], this was achieved using the Hartmann-Hahn matching condition, which applies two radiofrequency pulses (one at the resonance energy for ^{1}H, and the second at the resonance energy for ^{13}C), making the energy splitting of the two nuclei equal.

Solid state NMR spectra of [Zn(asp)] and aspH_2 were recorded at 9.4T on a Bruker DSX400 spectrometer equipped with a 4mm $^{1}H/X/Y$ triple resonance probehead. Samples were spun in zirconia rotors using dry N_2 bearing gas. The ^{1}H-^{13}C CP/MAS NMR spectra were acquired at 400.16 MHz for ^{1}H and 100.56 MHz for ^{13}C at MAS rate of 10.0 kHz. A ^{1}H $\pi/2$ pulse length was 3.0 μs and the recycle delay was 10 s. Two Phase Pulse Modulation (TPPM) decoupling was used during acquisition. The CP contact time was 2.0 ms with the Hartmann–Hahn matching condition set using Hexamethylbenzene (HMB). The ^{13}C chemical shifts are quoted in ppm with respect to TMS.

The spectra were recorded and analysed by James T. A. Jones within the group of Yaroslav Khimyak in the Department of Chemistry, within the University of Liverpool.

2.7 Elemental analysis

Elemental microanalysis was performed by Steve Apter in the Department of Chemistry, within the University of Liverpool on a Carlo Erber 1106 CHN analyser.

2.8 References

(1) For a detailed account of different methods of crystallisation at ambient pressures, see http://www.nottingham.ac.uk/~pczajb2/growcrys.htm and the links therein.

(2) Hamann, S. D. *Phys. Chem. Earth* **1981**, *13/14*, 89-111.

(3) Knauth, P.; Schoonman, J. *Nanostructured Materials: Selected Synthesis Methods, Properties and Applications*; Springer, 2002.

(4) Rabenau, A. *Angew. Chem. Int. Ed. Engl.* **1985**, *24*, 1026-1040.

(5) Clegg, W. *Crystal Structure Determination*; Oxford University Press: Oxford, 1998.

(6) Giacovazzo, C.; Monaco, H. L.; Artoli, G.; Viterbo, D.; Ferraris, G.; Gilli, G.; Zanotti, G.; Catti, M. *Fundamentals of Crystallography*; Oxford University Press: Oxford, 2002.

(7) Bragg, W. L. *Proc. Camb. Phil. Soc.* **1913**, *17*, 14.

(8) Rietveld, H. M. *Acta Cryst.* **1967**, *22*, 151-152.

(9) Rietveld, H. M. *J. Appl. Cryst.* **1969**, *2*, 65-71.

(10) Lebail, A.; Duroy, H.; Fourquet, J. L. *Mater. Res. Bull.* **1988**, *23*, 447-452.

(11) McCusker, L. B.; VonDreele, R. B.; Cox, D. E.; Louër, D.; Scardi, P. *J. Appl. Cryst.* **1999**, *32*, 36-50.

(12) Rodríguez-Carvajal, J. *Commission on Powder Diffraction (IUCr)* **2001**, *26*, 12-19.

(13) Merrill, L.; Bassett, W. A. *Rev. Sci. Instrum.* **1974**, *45*, 290-294.

(14) Piermarini, G. J.; Block, S.; Barnett, J. D.; Forman, R. A. *J. Appl. Phys.* **1975**, *46*, 2774-2780.

(15) Sheldrick G. M. *CELL_NOW;* University of Gottingen: Gottingen. Germany, 2005.

(16) Dawson, A.; Allan, D. R.; Parsons, S.; Ruf, M. *J. Appl. Cryst.* **2004**, *37*, 410-416.

(17) Cernik, R. J.; Clegg, W.; Catlow, C. R. A.; Bushnell-Wye, G.; Flaherty, J. V.; Greaves, G. N.; Burrows, I.; Taylor, D. J.; Teat, S. J.; Hamichi, M. *J. Synchrotron. Rad.* **1997**, *4*, 279-286.

(18) Brunauer, S.; Deming, L. S.; Deming, W. E.; Teller, E. *J. Am. Chem. Soc.* **1940**, *62*, 1723-1732.

(19) Brunauer, S.; Emmett, P. H.; Teller, E. *J. Am. Chem. Soc.* **1938**, *60*, 309-319.

(20) Langmuir, I. *J. Am. Chem. Soc.* **1916**, *38*, 2221-2295.

(21) Beesley, T. E.; Scott, R. P. W. *Chiral Chromatography*; WileyBlackwell: Chichester, 1988.

(22) Vaidhyanathan, R.; Bradshaw, D.; Rebilly, J.-N.; Barrio, J. P.; Gould, J. A.; Berry, N. G.; Rosseinsky, M. J. *Angew. Chem. Int. Ed.* **2006**, *45*, 6495 –6499.

(23) Deacon, G. B.; Phillips, R. J. *Coord. Chem. Rev.* **1980**, *33*, 227-250.

(24) Deacon, G. B.; Huber, F. *Inorg. Chim. Acta.* **1985**, *104*, 41-45.

Chapter 3 Frameworks derived from Zn and aspartic acid

3.1 Introduction

Amino acid coordination chemistry is dominated by the formation of a five-membered bidentate N-O metallacycle.[1] Although extended structures with amino-acids have been reported previously, the frameworks formed have been 1D, or 2D if a rigid linker such as 4,4'-bipyridyl (bipy) is used within the synthesis. L-aspartic acid (L-aspH_2) is an amino-acid which contains a carboxylic acid side chain, capable of coordinating to metal centres. Coordination compounds formed from aspH_2 typically contain a tridentate chelation to a central metal ion comprised of two metallacycles, derived from the 5-membered N-O chelate motif prevalent in amino acid chemistry, and a 6-membered N-O chelation from the carboxylate side chain of aspH_2 (Figure 3.1). Divalent metals generally crystallise with asp to form 1-dimensional chains linked by the C=O oxygen atom of the carboxylate involved in the aforementioned 6-membered chelation.[2-4] However, Jacobson et al have formed two nickel aspartate materials in which both carboxylates bridge between the Ni(II) ions to generate; i) a 1-dimensional homochiral helical chain,[3] and ii) a 3-dimensional porous framework which is based upon helical chains, that possesses extended Ni–O–Ni bonding.[2]

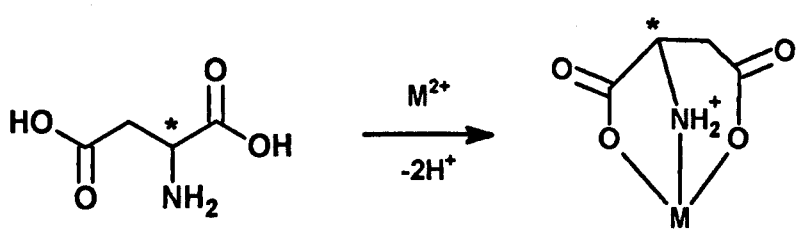

aspartic acid (aspH_2) **O-N-O tridentate chelate**

Figure 3.1. The structure of L-aspartic acid and the O-N-O tridentate chelate formed with divalent metals. The asterisk denotes the chiral centre.

3.1.1 The [Ni_2(L-asp)$_2$(bipy)] family

Recently we synthesised a homochiral metal-organic framework (MOF) based upon Ni, L-asp and the rigid polydentate linker 4,4′-bipyridyl (bipy).[5] This was achieved either by the solvothermal reaction of $NiCO_3$, L-aspH_2 and bipy in a one pot reaction of the chiral precursor [Ni(L-asp)(H_2O)$_2$]•H_2O and bipy. The formed material [Ni_2(L-asp)$_2$(bipy)]•guest (Figure 3.2) contains one-dimensional permanently porous channels and demonstrates enantioselective separation capabilities. The performance of the separation was determined to be dependent upon the length, shape and the type of functional groups within the chiral guest molecules. Other derivatives of this material were synthesised, with the pore geometry adapted by adjustment of the rigid polydentate pyridyl linker within the synthesis.[6] Analogues with different M^{2+} ions such as Cu[7] and Co[8] were also synthesised, and the post-synthetic modification of the Cu and Ni analogues by protonation were performed, with the subsequent asymmetric catalytic activity determined.[7]

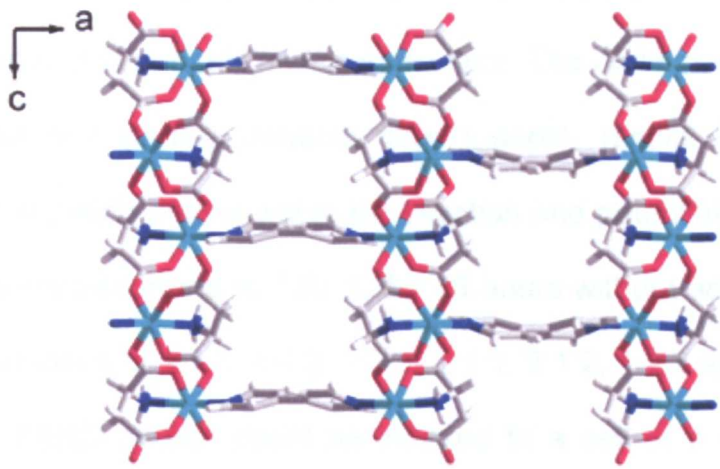

Figure 3.2. The structure of [Ni_2(L-asp)$_2$(bipy)], showing the porous 1D channels along the *b*-axis . Nickel is cyan, carbon is grey, oxygen is red, nitrogen is blue and hydrogen is white.

We were interested in synthesising the Zn analogue of the [M_2(L-asp)$_2$(bipy)] family to determine the comparative performance for enantioselectivity with the Ni analogue, and the effect of having a Lewis acidic metal centre upon the asymmetric catalytic activity of the protonated material. In addition, if the material was loaded with chirally pure guest molecules, solid state NMR could be used to demonstrate the interactions between the guest and the host material, allowing better prediction of suitable chiral guests for enantioselective separation using computational methods.

3.2 Initial syntheses

Initial work focussed upon using analogous conditions for the solvothermal synthesis of [Ni_2(L-asp)$_2$(bipy)]. However, both the $ZnCO_3$/L-aspH_2/bipy and the Zn(L-asp)/bipy methods produced solids, which were amorphous by powder X-ray diffraction (PXRD). We then instigated a synthetic search by varying the solvothermal reaction conditions for $ZnCO_3$ + L-aspH_2 + bipy in a 1:1 H_2O/MeOH *v/v* mixture at different temperatures, concentrations, pH and reaction time. The metal carbonate was used, as protonation of this starting material from L-aspH_2 results in CO_2 and H_2O, precluding any competing anions within the reaction and potential by=products. The initial reactions were performed at 130 °C for 48 hours without adjustment of pH, at Zn:asp:bipy molar ratios of 1:1:1, 1:1:2, 1:2:1, 2:1:1, 2:1:2, 1:2:2 and 2:2:1. From the ratio of 1:2:1, a PXRD pattern could be indexed to a cell of *a* = 20.818(23), *b* = 11.007(12), and *c* = 8.123(8) Å, with one unindexed line at 2 theta = 5.59° (Figure 3.3 b)). This led to a focussed search around this stoichiometry, in order to synthesise a phase pure material. The initial phase searches are summarised as phase diagrams in Figure 3.3 (a) and (c).

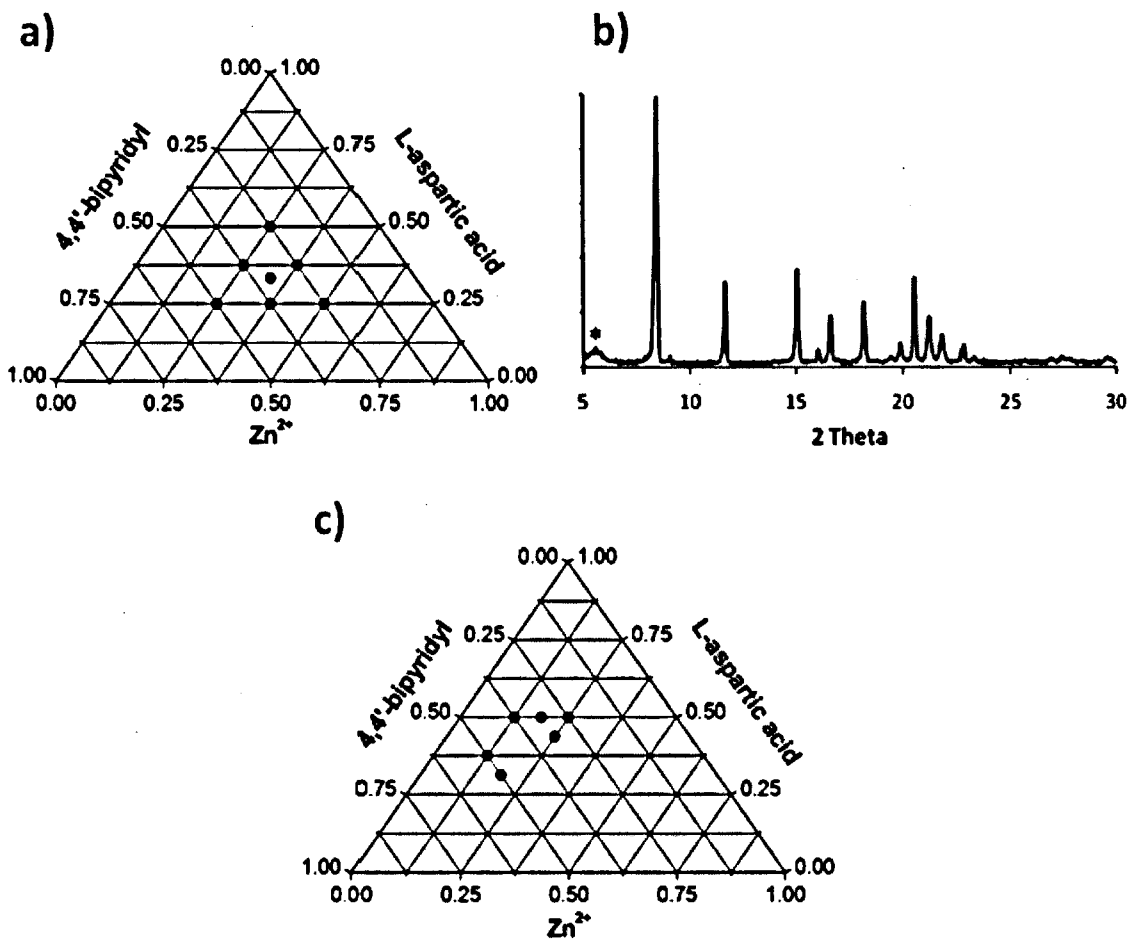

Figure 3.3. a) The initial phase space search at 130 °C for 48 hours, (b) the impure PXRD pattern with the unindexed line denoted by an asterisk, and c) Additional reactions performed at 130 °C for 72 hours. The scale of the phase diagrams are in mole fractions.

3.3 A permanently porous material comprised of Zn, iminodisuccinic acid and 4,4'-bipyridyl [Zn_2(IDS)(bipy)]

3.3.1 Synthesis

The reaction of $ZnCO_3$, aspH_2 and bipy (molar ratio = 1:2:1) in a H_2O/MeOH mixture (2.65/1.35ml respectively) under solvothermal conditions at 130 °C yielded yellow crystals with pseudo-hexagonal external morphology. Structure solution and refinement revealed the framework composition to be [Zn_2(IDS)(bipy)], with transformation of the aspH_2 to *meso*-iminodisuccinic acid (IDSH_4) (Figure 3.4).

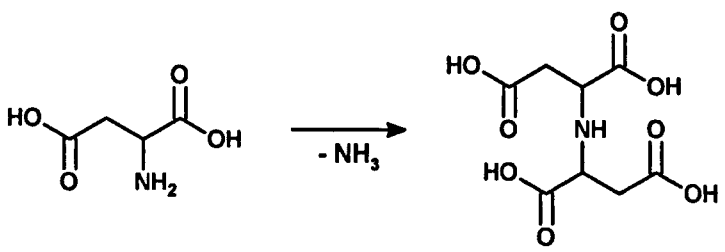

Figure 3.4. The conversion of aspH_2 to IDSH_4 resulting in the dissociation of an NH_3 molecule.

The phase purity of the bulk sample was determined by PXRD, and is consistent with the homogeneous morphology of the material under examination using scanning electron microscopy (SEM) (Figure 3.5). Elemental analysis corresponds to the bulk composition [Zn_2(IDS)(bipy)]·3H_2O for 1 (calculated (%): C 37.05, H 3.63, N 7.21; found (%): C 37.17, H 3.60, N 7.24), and is in good agreement with the crystallographically derived formula. The pH before the reaction was 5.2, increasing to 7.2 after the reaction, caused by the release of NH_3 from the *in-situ* dimerisation reaction. Yield = 11.95% based on Zn(II). Careful control of the ratio of MeOH to H_2O molecules is required to form a single phase material and any deviation from

the 2:3 ratio described above results in the production of an additional gel phase, which could not be characterized by PXRD.

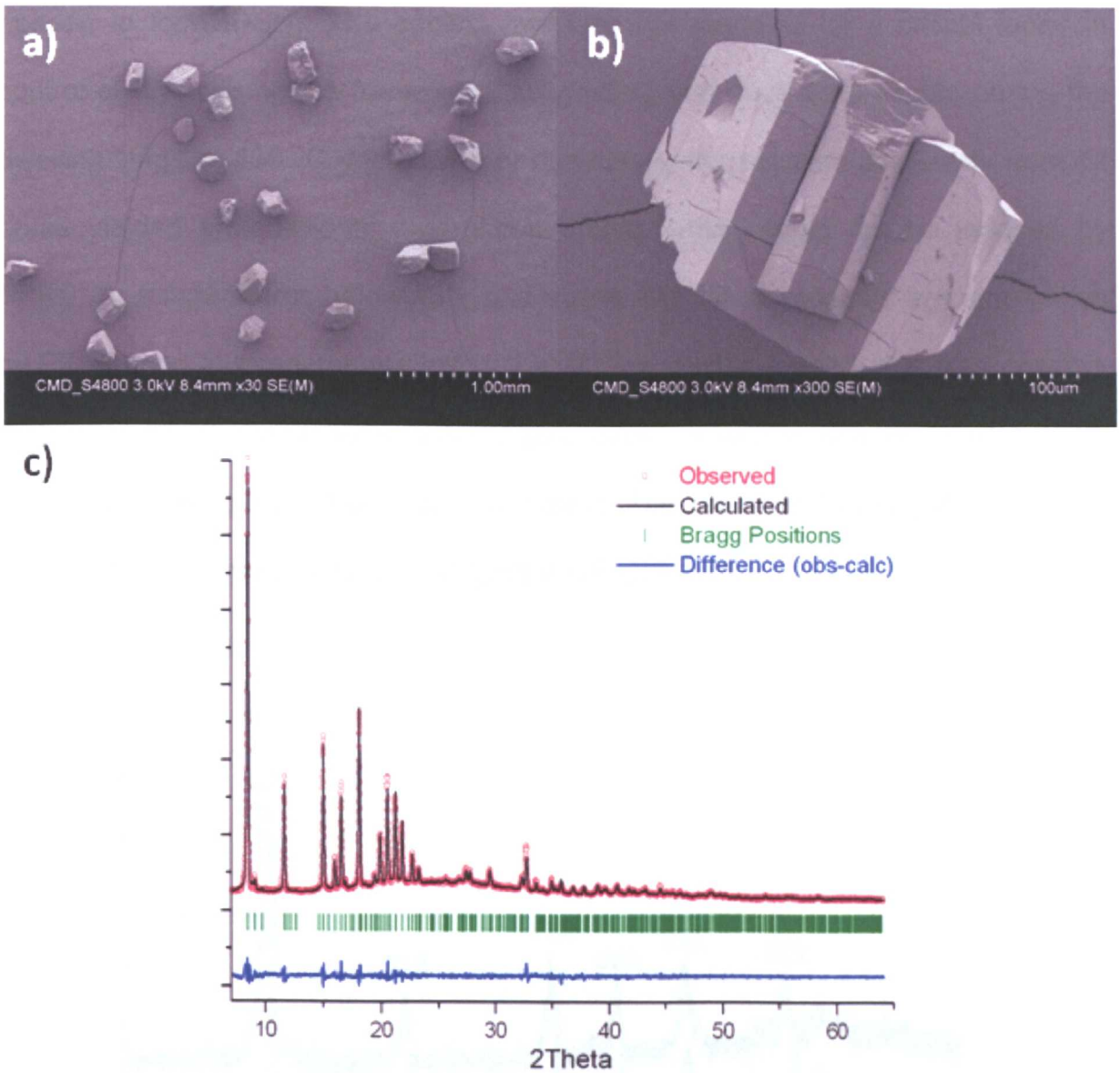

Figure 3.5. a) Homogeneous morphology of the particles of [Zn_2(IDS)(bipy)] under SEM, and b) a single twinned crystal comprised of at least two components inter-grown. c) The Le Bail fit of [Zn_2(IDS)(bipy)]. Refined cell parameters (RT): *a* = 10.0196(4), *b* = 11.0192(5), *c* = 20.8891(12). Single crystal cell parameters (150K): *a* = 10.0245(4), *b* = 10.8912(4), *c* 20.7145(8).

Precise control of the reagent ratios was also found to be critical in forming a single phase material; the molar ratio of Zn:asp:bipy required to form [Zn_2(IDS)(bipy)] is 1:2:1, whereas the expected molar ratio is 2:2:1, as two L-aspH_2 molecules are needed to form IDSH_4. The cooling rate was not found to be a critical factor in control of crystallising the framework, suggesting that nucleation occurs during the dwelling stage at 130 °C. Increasing or decreasing the reaction time away from 72 hours yielded an additional amorphous phase, which could not be indexed by PXRD. At temperatures below 130, and above 140 °C all products are amorphous by PXRD, and at temperatures below 120 °C, no solid is formed. It is also possible to make a largely amorphous material with some crystalline features using IDSNa_4 in an analogous preparation with zinc nitrate. The resulting PXRD pattern can be indexed to the same cell as [Zn_2(IDS)(bipy)] (Figure 3.6).

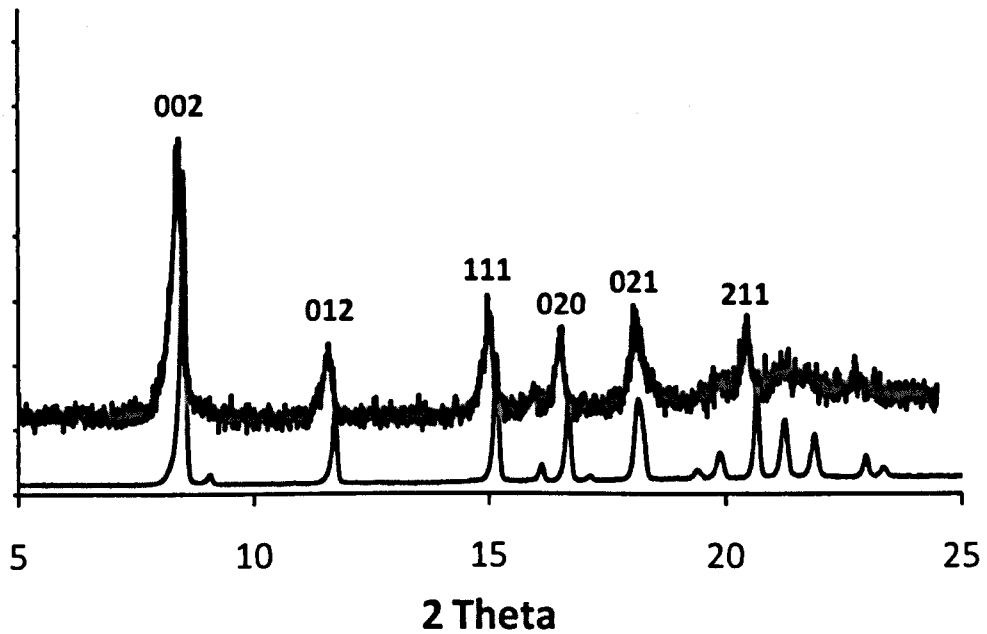

Figure 3.6. The PXRD pattern of [Zn_2(IDS)(bipy)] using the standard synthesis with $ZnCO_3$, with L-aspH_2 (light grey), and synthesised using $Zn(NO_3)_2$ with IDSNa_4 (dark grey). Note that although the pattern using IDSNa_4 is less crystalline, the peaks corresponding to the 002, 012, 111. 020, 021 and 211 reflections are still evident.

3.3.2 *X-ray Structural Studies*

Optical and scanning electron microscopy and crystallography demonstrate that these crystals are extensively twinned, and the framework structure to be globally disordered. Pseudo-hexagonal external morphology is observed (Figure 3.5b), a result of cyclical twinning: with multiple twin boundaries intersecting at 180° or 60°. A few crystals appeared to be prismatic but with opposite faces not parallel to each other. This external form is not consistent with *mmm* or *2/m* point symmetry and also indicated that these crystals are twinned.

X-ray data collection and analysis was performed on a crystal without obvious external features of twinning. X-ray intensity data were collected at Daresbury Synchrotron Radiation Source, Station 9.8 MX on a Bruker D8 diffractometer with an APEX II CCD detector with Si 111 monochromated radiation (λ = 0.671 Å). A small primitive unit cell with $a \approx 5.0$ Å could be identified from the strong reflections while doubling *a* accounted for all the discrete reflections, including the weak reflections. Final cell constants obtained from least-squares refinement on 6188 reflections corresponded to an orthorhombic cell (space group $P2_12_12_1$) with the dimensions: a = 10.0245(4) Å, b = 10.8912(4) Å, c = 20.7145(8) Å and V = 2261.6(2) Å^3. The frames were integrated with the Bruker SAINT v6.45a software package[9] using a narrow-frame integration algorithm. The integration of the data using the orthorhombic unit cell yielded a total of 16980 reflections, of which 4083 were independent (completeness = 99.0%, Rint = 5.93%). Analysis of the data showed negligible decay during data collection. The data were corrected for absorption, decay and other errors using SADABS V2007-2.[10] The structure was solved (by direct methods) and refined using SHELX.[11] As all of the crystals were extensively

twinned, the structure was solved by dividing the diffraction into two components, corresponding to two domains, which contributed 70% and 30% respectively. However, within the structural model, the two domains are translated along the *a*-axis by 5 Å, and as Zn1 and Zn2 are separated by 5.14 Å along the same axis, there exists the possibility of mixing the two zinc atoms and their respectively bound O atoms (the closest separation between O atoms from the two components is only 0.5 Å). Therefore it is hard to define which Zn and O atoms are bound together due to the overlapping of the two components, and the possibility of defining Zn-O bonds that are artificially shortened and lengthened exists. Nevertheless the connectivity is correct, but it is hard to define accurate bond distances and angles here.[12] All the representations and calculations performed on the crystal structure were realized from component 1, which corresponds to the domain that contributes to 70% of the observed diffraction. This multiple domain analysis was performed by John Bacsa at the University of Liverpool. The corresponding CIF file is located in Appendix A.

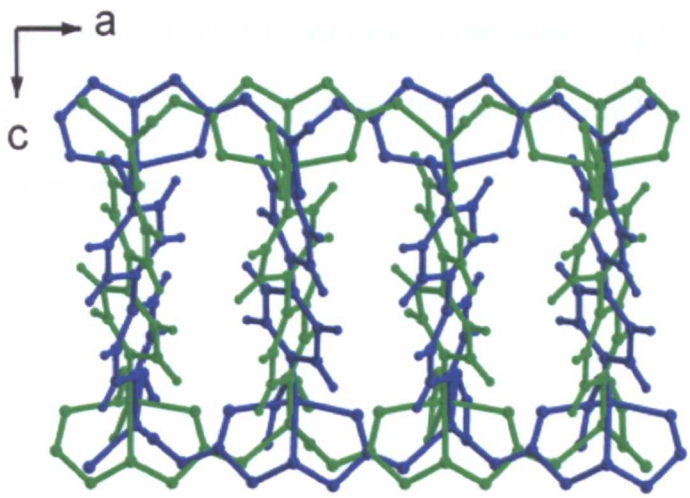

Figure 3.7. The overlapping of the two components within the structure model of [Zn_2(IDS)(bipy)]. The green moiety corresponds to component 1, which contributes to 70% of the observed diffraction. The blue moiety corresponds to component 2, which contributes to 30% of the observed diffraction.

3.3.3 *Structure of [Zn_2(IDS)(bipy)]*

Within [Zn_2(IDS)(bipy)], the IDS ligand binds to five separate Zn cations, which are present as two crystallographically independent Zn(II) centres (Zn1 and Zn2) (Figure 3.9 a)). The IDS ligand displays three distinct coordination modes; i) a central Zn1 ion is bound to two oxygen atoms and a nitrogen atom in an eight-membered O-N-O tridentate *mer* chelation, which involves monodentate binding by two of the four carboxylate groups and the single amino group of the IDS ligand, ii) the remaining oxygen atoms of the two carboxylate groups from the O-N-O chelation in i) bridge to two Zn2 centres, and iii) the two remaining carboxylate groups each chelate to a Zn centre (one chelates to Zn1, and the second chelates to Zn2). This is in contrast to the known molecular structures of IDS complexes, where the ligands are typically tetradentate, forming a 6-membered and two 5-membered metallacycles, from a central nitrogen.[13,14] However, an extended framework based upon IDS and zinc has been recently reported by Cheetham *et al* with the formula [Zn_2(IDS)],[15] in which the tetra-acid was formed by analogous *in-situ* dimerisation during solvothermal synthesis with L-aspH_2 and Zn(II) acetate. This was suggested to occur via formation of a butenedioic acid intermediate, followed by Michael addition of aspH_2 across the alkene (Figure 3.8).

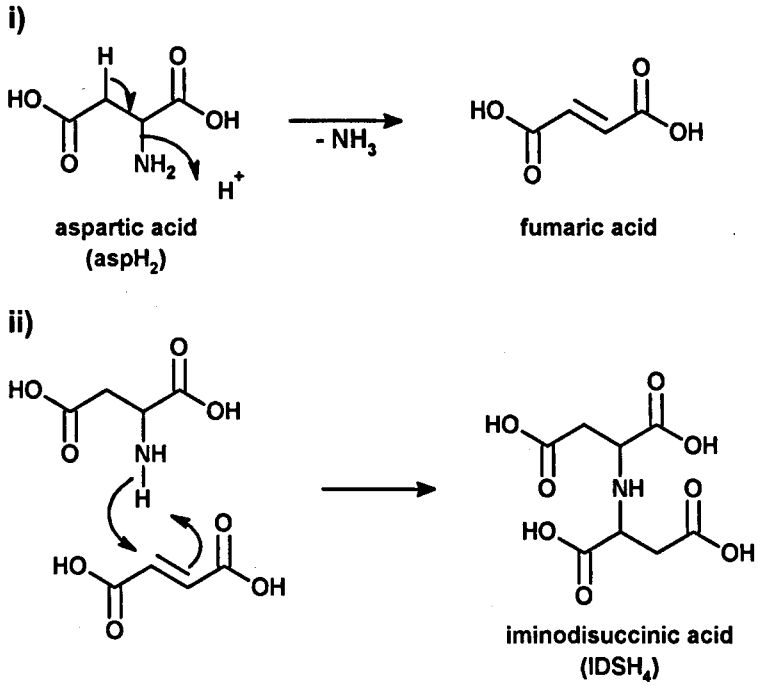

Figure 3.8. The mechanism of asp-IDS conversion as proposed by Cheetham *et al.*[15] i) Acid catalysed removal of NH_3 to yield fumaric acid. ii) Michael addition of $aspH_2$ to fumaric acid to yield iminodisuccinic acid ($IDSH_4$).

Unlike $[Zn_2(IDS)(bipy)]$, the framework $[Zn_2(IDS)]$ is two-dimensional, but displays some similar structural characteristics to $[Zn_2(IDS)(bipy)]$. There are two independent Zn sites, and $[Zn_2(IDS)]$ displays two IDS coordination modes, which are also observed in $[Zn_2(IDS)(bipy)]$; the eight-membered O-N-O tridentate *mer* chelation to Zn, and the bridging functionality of the chelating carboxylate groups. However, the key difference between the two compounds can be noted from the binding modes of the two carboxylate groups which are not involved in the central chelation. Within $[Zn_2(IDS)]$ these groups each coordinate to two Zn(II) ions (a total of four Zn), whereas in $[Zn_2(IDS)(bipy)]$ they are bound to one each (a total of two Zn) (Figure 3.9 b)). The absence of these binding modes within $[Zn_2(IDS)(bipy)]$, increases the dimensionality of the framework, from 2 to 3D and decreases the

denticity of the ligand, from hepta- to pentadentate, because bipy occupies the remaining Zn coordination sites and connects the layers.

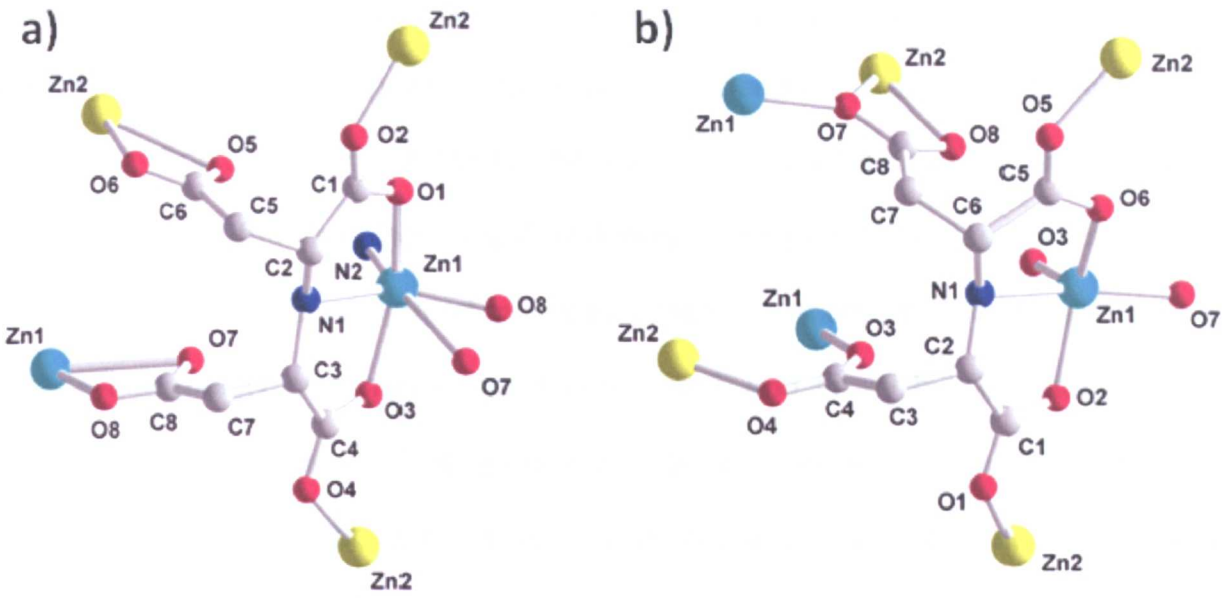

Figure 3.9. a) The three coordination modes of the IDS ligand within [Zn_2(IDS)(bipy]. The eight-membered O1-N1-O3 tridentate *mer* chelation to Zn1, the single oxygen binding to Zn2 (O2-Zn2 and O4-Zn2) and the bidentate chelation of the carboxylate moieties to the crystallographically unique Zn centres (O5-Zn2-O6 and O7-Zn1-O8). b) The coordination modes of the IDS ligand within [Zn_2(IDS)].[15] The two analogous binding modes of IDS to zinc are evident; the eight-membered O2-N1-O6 tridentate *mer* chelation to Zn1, and the single oxygen binding to Zn2 (O1-Zn2 and O5-Zn2). The remaining three coordination modes are also evident; the single binding of an oxygen to Zn (O4-Zn2 and O3-Zn1), bidentate coordination of a μ1 and a μ2 oxygen to Zn (O7-Zn2-O8), and finally the single oxygen binding from a μ2 oxygen (O7-Zn1). Carbon is grey, nitrogen is blue, oxygen is red, zinc1 is cyan and zinc2 is yellow. Hydrogen atoms are omitted for clarity.

The two independent Zn atoms in the asymmetric unit of $[Zn_2(IDS)(bipy)]$ are in irregular coordination environments. This is well-documented for zinc complexes, which adopt coordination environments that are heavily distorted away from the classical polyhedron geometries without any significant energy penalty.[16] Zn1 is six-coordinate (Figure 3.10 a)), bonding to two IDS ligands and a single pyridyl moiety from bipy. One IDS ligand binds to Zn1 via two carboxylate oxygen atoms and a nitrogen atom, forming the O-N-O tridentate chelation described above. The coordination sphere is completed by the bidentate chelation from oxygen atoms of a carboxylate moiety of a neighbouring IDS ligand, and finally by coordination of a nitrogen atom from bipy. This gives a Zn1 bond valence of 2.19. The bidentate coordination of the carboxylate group is distinctly asymmetrical, with a long Zn-O carboxylate bond (2.682(9) Å), which is partly compensated by formation of an intramolecular C=O···H-N hydrogen bond (O···N distance = 2.96(1) Å) between the carboxylate group and the central amine group in IDS. Zn2 is five-coordinate (Figure 3.10 b)), with four carboxylate oxygen donors arising from coordination from three distinct IDS ligands and one nitrogen atom from bipy. The resulting coordination geometry is a highly distorted square based pyramid, with a total bond valence of 1.94. Again, the bidentate carboxylate chelation is distinctly asymmetrical (there is one short Zn-O bond, 2.09(1) Å, and one long bond, 2.462(8) Å), with the weaker coordinating oxygen accepting an aromatic C-H···O intermolecular hydrogen bond (C···O distance = 3.39(1) Å) from a neighbouring bipy ligand. The bond valence sums at both Zn sites indicate a chemically correct description of the bonding has been deduced, despite the existence of two disordered components within the structural model.

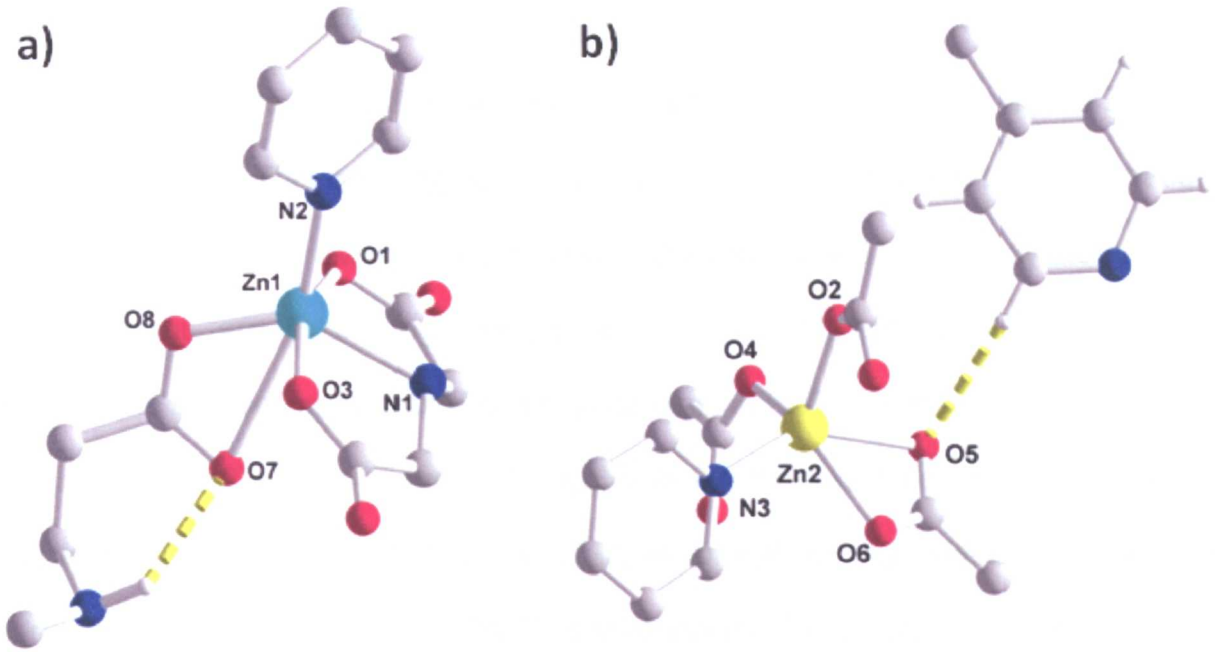

Figure 3.10. a) The distorted octahedral coordination environment of Zn1. The metal centre is bound to two IDS ligands and a single bipy ligand. The longer Zn-O distance of the more weakly coordinating O7 of the unsymmetrical bidentate carboxylate group is compensated by a C=O···H-N intramolecular hydrogen bond from the amine group in IDS, shown by a broken yellow line. b) The distorted square-bipyramidal coordination environment of Zn2. The metal centre is bound to three IDS ligands and a single bipy ligand. The weaker coordinating O5 is compensated by a C=O···H-C hydrogen bond from a neighbouring bipy ligand, as shown by a broken yellow line. Carbon is grey, hydrogen is white, nitrogen is blue, oxygen is red, zinc1 is cyan and zinc2 is yellow.

3.3.4 Extended structure

The two carboxylate groups involved in the O-N-O chelation of Zn1 bridge to Zn2, as described above. This bonding occurs along the *a*-axis, and leads to the formation of an infinite chain of alternating Zn1 and Zn2 atoms linked by carboxylate groups. These chains are linked together by two carboxylate terminated arms of IDS towards the *b* direction, with one carboxylate binding to Zn1 and the other binding to Zn2, forming a 2D layer (Figure 3.11. a)). Viewing the two-dimensional layer along the *a*-axis (orthogonal to the plane of layer formation) demonstrates it takes a corrugated shape (Figure 3.11 b)i)). This shape is due to the arc-like conformation of the IDS ligand within the structure (Figure 3.11 b)ii)), and a 180° rotation of the IDS ligand at each Zn connection along the *b*-axis. The arc-like conformation of the ligand arises from the flexible $-CH_2-$ carbons (C5 and C7) in the carboxylate arms that point along the *b*-axis, leading to an angle of 100° between the chains of alternating Zn1 and Zn2 atoms with respect to the ligand. In order to accommodate the bipy ligand, the IDS ligands coordinate *trans* to each other, rotating by 180°, and leading to the corrugated shape of the two-dimensional layer. The bipy ligand links the layers in the *c* direction through bonding between Zn1 and Zn2, at an angle of 44.8° from the plane of the layer (Figure 3.11 c))., and each successive layer is rotated by 180° about *c* in order to accommodate coordination of Zn to the bipy nitrogen. This leads to the formation of an ABA stacking pattern along *c* (Figure 3.11 d)).

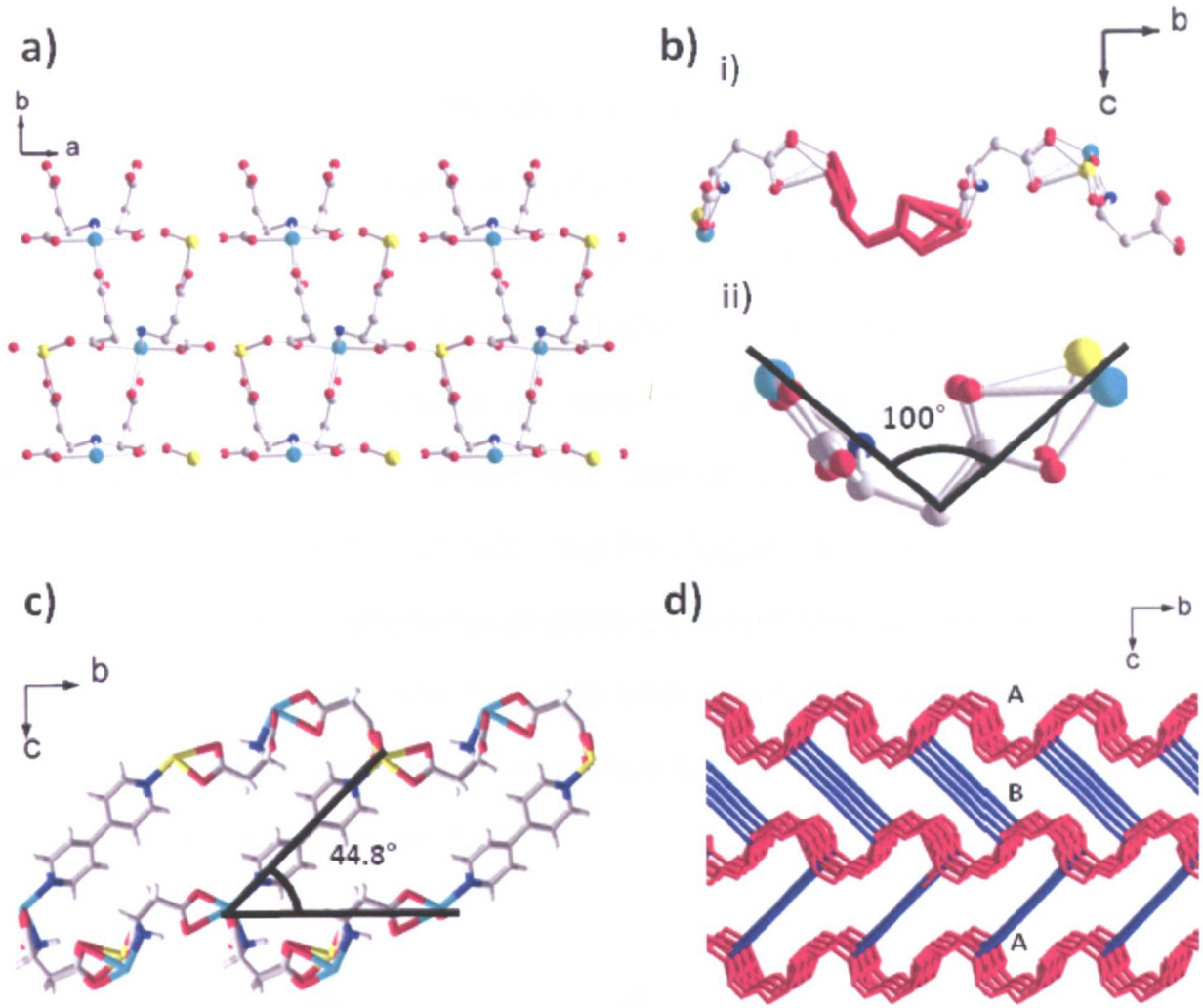

Figure 3.11. a) The connectivity of Zn with IDS in the *ab* plane. The ligand links alternating Zn atoms along the *a*-axis via the tridentate chelation and the bridging functionality of the carboxylate groups. The remaining two carboxylate groups bridge to an adjacent chain of Zn atoms, forming the 2D layer. b)i) Rotating the layer by 90° and viewing down the *a*-axis demonstrates the layer takes a corrugated shape. The red atoms/bonds highlight a single IDS ligand. ii) The angle between the Zn atoms with respect to the centre of the ligand is equal to 100°, giving the arc shape of the ligand. Propagating along *b*, the ligand is rotated by 180° at each Zn connection, leading to the corrugated shape. c) The bipy ligand is at an angle of 44.8° with respect to the layer comprised of Zn and IDS along the *b*-axis. Each successive layer of Zn and IDS along the *c*-axis is rotated by 180° to accommodate each bipy connection, leading to d) an ABA stacking pattern. Carbon is grey, hydrogen is white, nitrogen is blue, oxygen is red, zinc1 is cyan and zinc2 is yellow.

3.3.5 Topological analysis

Topological analysis is concerned with the classification of coordination polymers and supramolecular architectures as a series of nodes and edges. With MOFs which contain metal clusters and symmetrical rigid linkers, the assignment of topology is straightforward. For example, the MOF HKUST-1[17] is comprised of a copper-dimer paddlewheel, which has square C_4 symmetry, and the rigid tridentate linker benzenetricarboxylate (btc), which has trigonal C_3 symmetry (Figure 3.12). Assigning the centre of the C_4 cluster, and the C_3 ligand as nodes, and linking them together in the same arrangement as within the crystal structure of HKUST-1 leads to the network assignment, **tbo**. The three letter symbol arises from the terminology given by O'Keeffe and Proserpio and refers to naturally occurring minerals that share the network assignment.[18]

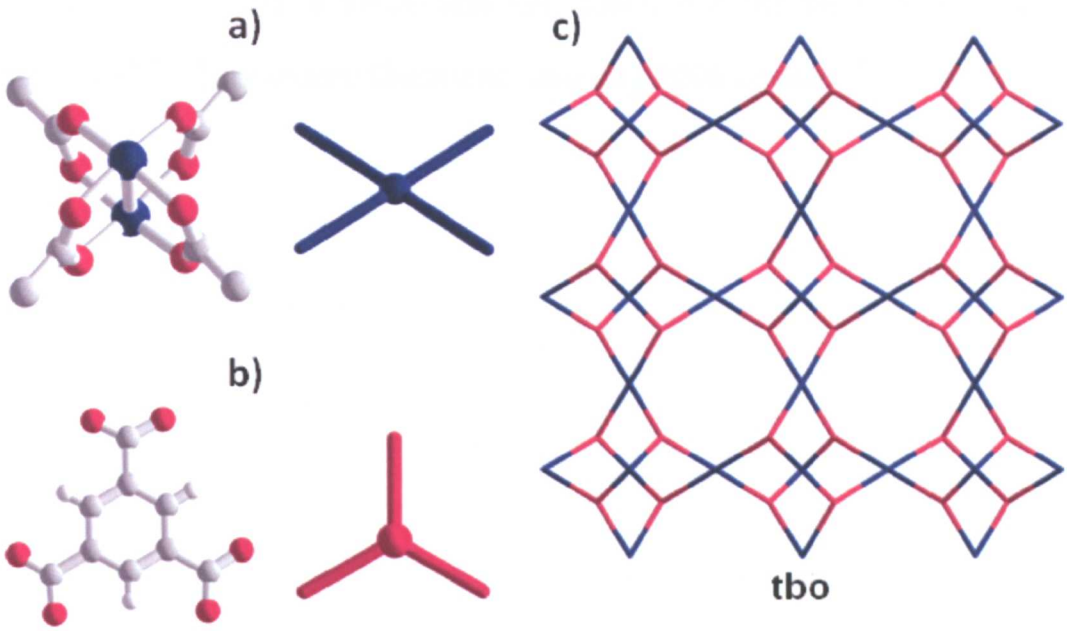

Figure 3.12. Network assignment of HKUST-1 a) The copper acetate paddlewheel dimer, which has C_4 symmetry (left), and the assigned node (right). b) The ligand btc which has C_3 symmetry (left), and the assigned node (right). c) The formed network has twisted boracite topology, designated tbo.

However, the network assignment of $[Zn_2(IDS)(bipy)]$ is not so straightforward, as the O-N-O chelation of IDS to Zn leads to a number of different choices of nodes and edges within the structure. In contrast, bipy is much simpler as it possesses C_2 symmetry and coordinates to two Zn centres in a straight line, and is therefore assigned as an edge between two nodes which correspond to Zn. When considering the network assignment, we will first define the 2D layer of Zn with IDS, and then add the bipy edge to yield the final 3D structure. If the Zn1 and Zn2 atoms are assigned as nodes, and the covalent connections made between them by the IDS ligand designated the edges (Figure 3.13 a – c)), then the resulting layer takes the form of the 3^6 hexagonal lattice **hxl** (Figure 3.13 e)), which is 6-connected and uninodal, despite the two geometrically distinct Zn atoms within the crystal structure of $[Zn_2(IDS)(bipy]$. Addition of the bipy edge to the layer leads to the 7-connected net **ose** (Figure 3.13 f)), a theoretical net, which has not been observed to date (source = TOPOS Topological Database, January 2009 update).[19]

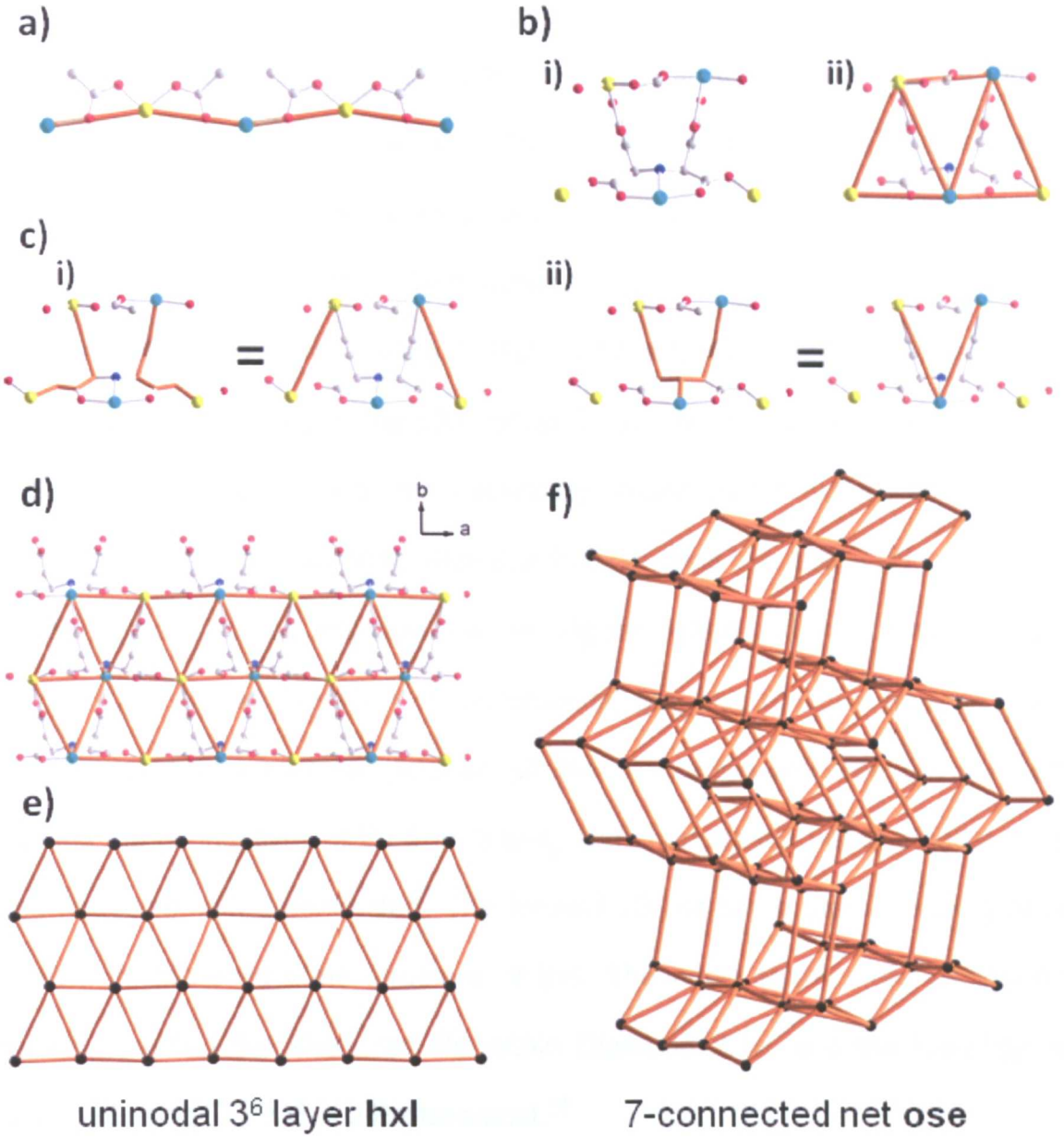

Figure 3.13. Network assignment of $[Zn_2(IDS)(bipy]$, assigning the Zn atoms as the nodes and the IDS and the bipy linkages as edges. a) The 1D chain of Zn1 and Zn2 linked by bridging carboxylates. b i) The connectivity of a single ligand, and ii) the ligand with the topological edges overlaid. c) i) The edges corresponding to the Zn2 nodes linking to Zn1 and Zn2 nodes in an adjacent layer, and ii) The edges corresponding to the links between the central Zn1 node and the Zn1/Zn2 nodes in an adjacent layer. d) The extension of the structure in the *ab* plane, leading to e) the uninodal 3^6 layer designated hxl. The black atoms correspond to the Zn nodes. f) Addition of the bipy edge in the structure leads to the network assignment of the 7-connected net ose.

However, this network assignment does not recognise the directionality of the IDS ligand, as each connection between the Zn atoms are taken as straight line linkages. An alternative method of deciding the topology of the framework is to assign nodes within the ligand. If we consider the 1D chain of alternating Zn1 and Zn2 atoms linked by carboxylates (Figure 3.14 a)), the carboxylates act as the edges between the nodes of the alternating Zn atoms. By adding of the rest of the ligand and assigning nodes on the secondary carbon atoms (where the links from the Zn atoms converge), demonstrates that IDS contains two nodes (Figure 3.14 b)), both of which are three connected. Connecting the ligand and the Zn nodes (Figure 3.14 c)), leads to the formation of the uninodal graphitic 6^3 layer **hcb**, as the Zn nodes are also 3-connected. Addition of the bipy edge between the Zn nodes increases the connectivity of Zn from 3 to 4, and changes the net to binodal, as the ligand nodes remain 3-connected. The formed 3D net takes the network type **ins**, derived from the solid state structure of InS. The node atoms were assigned by manually adapting the shelx res file within Diamond 2.1c, and the topology was determined using TOPOS 4.0 Professional.[13]

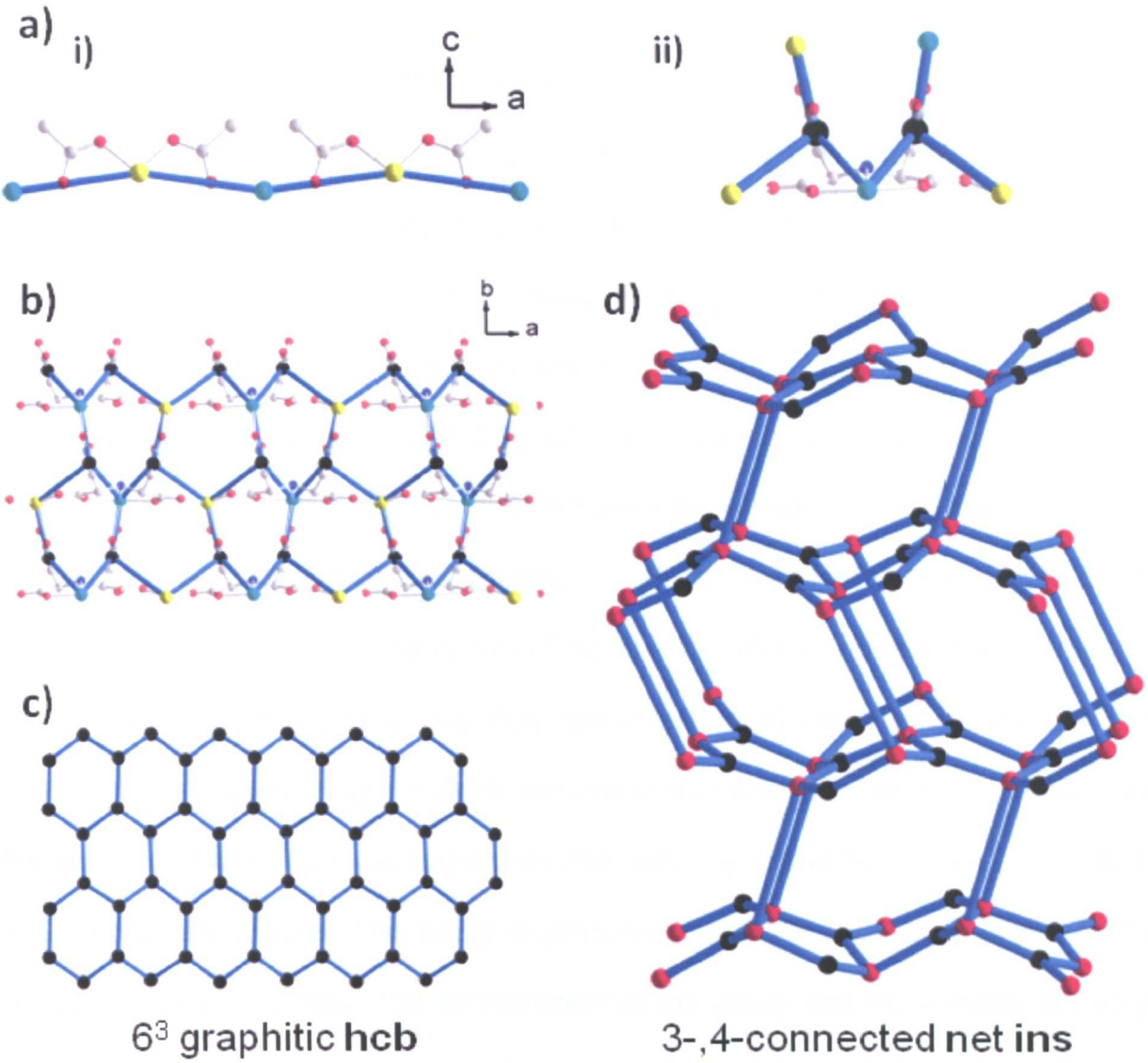

Figure 3.14. The network assignment of $[Zn_2(IDS)(bipy]$, recognising the directionality of the ligand as nodes. a) The straight chain of alternating Zn1 and Zn2 linked by carboxylates. Zn1 is cyan, Zn2 is yellow, oxygen is red and carbon is grey. Network edges are shown as blue bonds. b) The two ligand nodes are both 3-connected, as denoted by black atoms. c) The Zn nodes (now also 3-connected) link together with the ligand nodes to form, d) a 6^3 graphitic net. Both the Zn and the ligand nodes are shown in black as they are both 3-connected. e) Addition of the bipy edge between the Zn changes the connectivity of the node to 4, forming the 3-, 4-connected net ins. The 3-connected ligand nodes are coloured black, and the 4-connected Zn nodes are coloured red.

3.3.6 *Porosity studies*

The porosity arises in [Zn_2(IDS)(bipy)] from the open space in the crystal structure between the 2D layers of [Zn_2(IDS)], which are pillared by bipy. This is demonstrated by the Connolly surface,[8] where the pore surface is lined by two bipy molecules and two IDS ligands from two opposite layers, leading to one-dimensional channels along the crystallographic *a*-axis that have approximately oval-shaped windows with a cross-section of 4 *x* 3 Å (Figure 3.15 a)). These lead to larger cavities, which have a cross-section of 6 *x* 6 Å. The distance between the window opening and the centre of the cavity is 2.5 Å, which corresponds to ¼ of the cell length of the *a*-axis. Each cavity is slightly offset from the centre of the channel along *b*, due to the alternating Zn1 and Zn2 atoms along *a*, and their respective coordination environments. The Zn1 atom is surrounded by a bulky tridentate O-N-O chelation, which protrudes into the channels, taking up more room than Zn2, which is linked by oxygen atoms from IDS carboxylate groups. The cavity displacement along *b* causes the channels to adopt a sinusoidal shape. The environment of the cavity and the window are very similar, as the atom types and functional groups which line the window centre are the same as those which line the cavity (measured by inserting a 'void' atom in the centre of the cavity/window and crystallographically measuring the framework atoms which are closest to the 'void') (Figure 3.15 b)). In both cases the closest atoms are oxygen and hydrogen, creating a hydrophilic environment, which is ideally suited to the guest water molecules, as defined by the elemental analysis and thermogravimetric analysis (TGA).

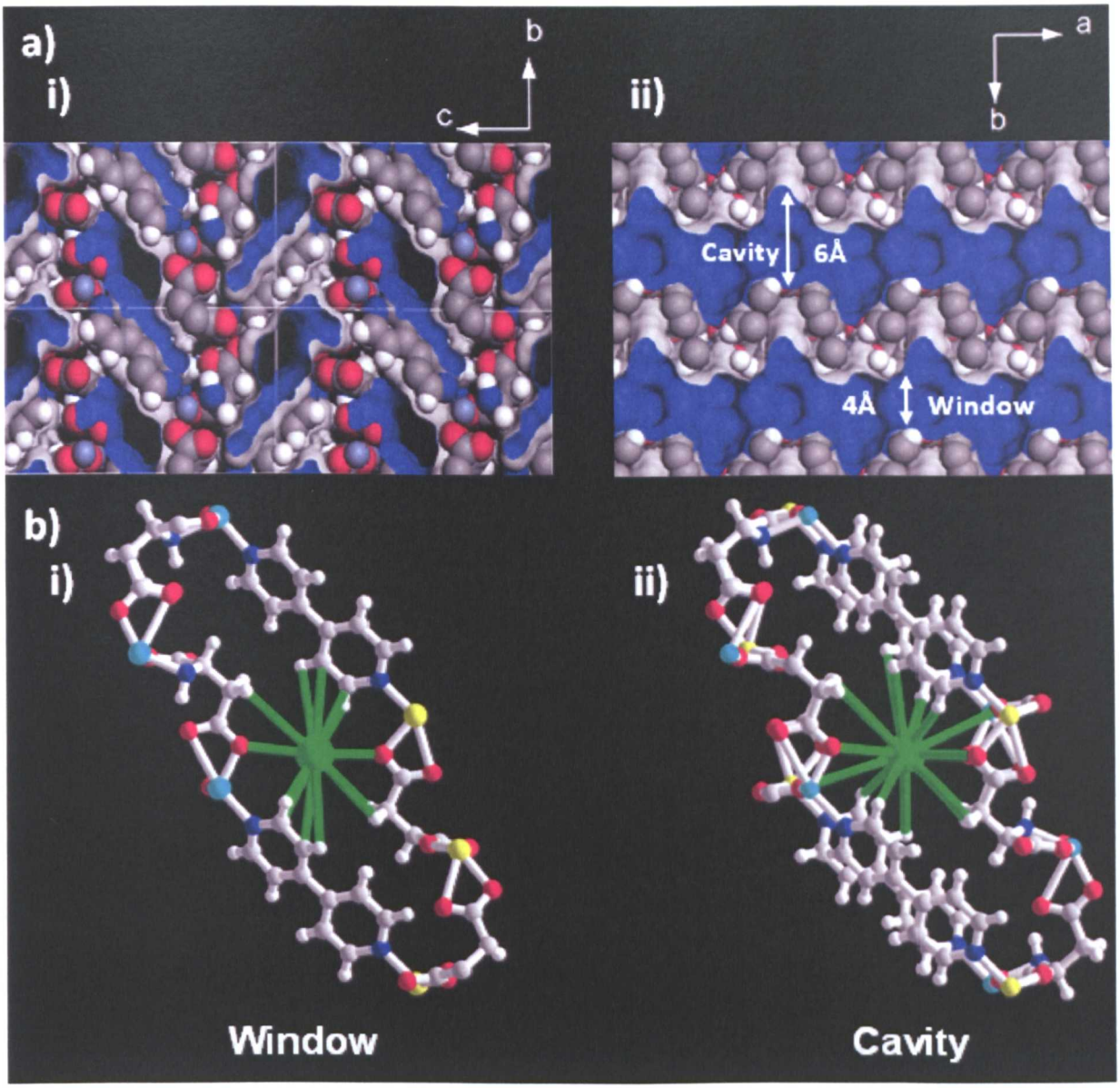

Figure 3.15. a) A view of the Connolly surface of the channels along the [100] axis of 1 (top) and perpendicular along the [010] (bottom).[8] The black spaces are open gaps within the structure. The framework atoms are shown in the space-filling style, and the calculated surface is highlighted in blue. Cavity and window are labelled in white. Carbon is grey, hydrogen is white, nitrogen is blue, oxygen is red, zinc is purple. b) The 'void' atom and the closest contacts to the framework highlighted by green bonds in the pore window, which has a cross section of 4 *x* 3 Å (left), and the 'void' atom the cavity, with the closest contacts to the framework highlighted again by green bonds. The 'void' atom is labelled green. All other atoms are labelled according to the colour scheme in Figure 3.9 a).

$[Zn_2(IDS)(bipy)]$ has 240 $Å^3$ solvent accessible volume per unit cell, which is equivalent to 11 % of the total volume of the unit cell, as determined by the SQUEEZE routine within PLATON.[20] In the as-prepared material, the channels contain three water molecules per formula unit ($[Zn_2(IDS)(bipy)]•3H_2O$ (elemental analysis (%) calculated: C 37.05, H 3.63, N 7.21; found: C 37.17, H 3.60, N 7.24), which have a combined volume of 59.1 $Å^3$.[21] As *Z* (the number of asymmetric units per unit cell) is equal to 4, the pore volume occupied by water molecules equate to 236.4 $Å^3$, demonstrating that the pores are 99 % filled. TGA of $[Zn_2(IDS)(bipy)]$ under a dynamic nitrogen flow reveals a weight loss of 8.82 % between room temperature and 150 °C, followed by a plateau and a mass loss of 63.41 % at 320 °C. The first mass loss is attributed to the removal of the three water molecules from within the pores (calculated weight loss from the analysed composition = 9.22 %), and the second mass loss accounts to the breakdown of the framework (calculated weight loss 63.02 % from the analysed composition) (Figure 3.16 a)). The similarity of the PXRD patterns of the as-synthesised, and the desolvated material demonstrates that framework $[Zn_2(IDS)(bipy)]$ is stable to guest loss, with the full width half maximum (FWHM) of the [002] peak is 0.15° in the as-synthesised material, and 0.17° post-desolvation (Figure 3.16 b)). Further evidence of the stability of the structure is provided by the elemental analysis of the desolvated material, which corresponds to the composition of $[Zn_2(IDS)(bipy)]$ without any guest molecules, $[Zn_2(IDS)(bipy)]$ (elemental analysis (%) calculated: C 40.84, H 2.86, N 7.94; found: C 41.01, H 2.79, N 8.23). The sample was prepared by heating $[Zn_2(IDS)(bipy)]•H_2O$ in a Schlenk tube overnight *en vacuo* at 100 °C.

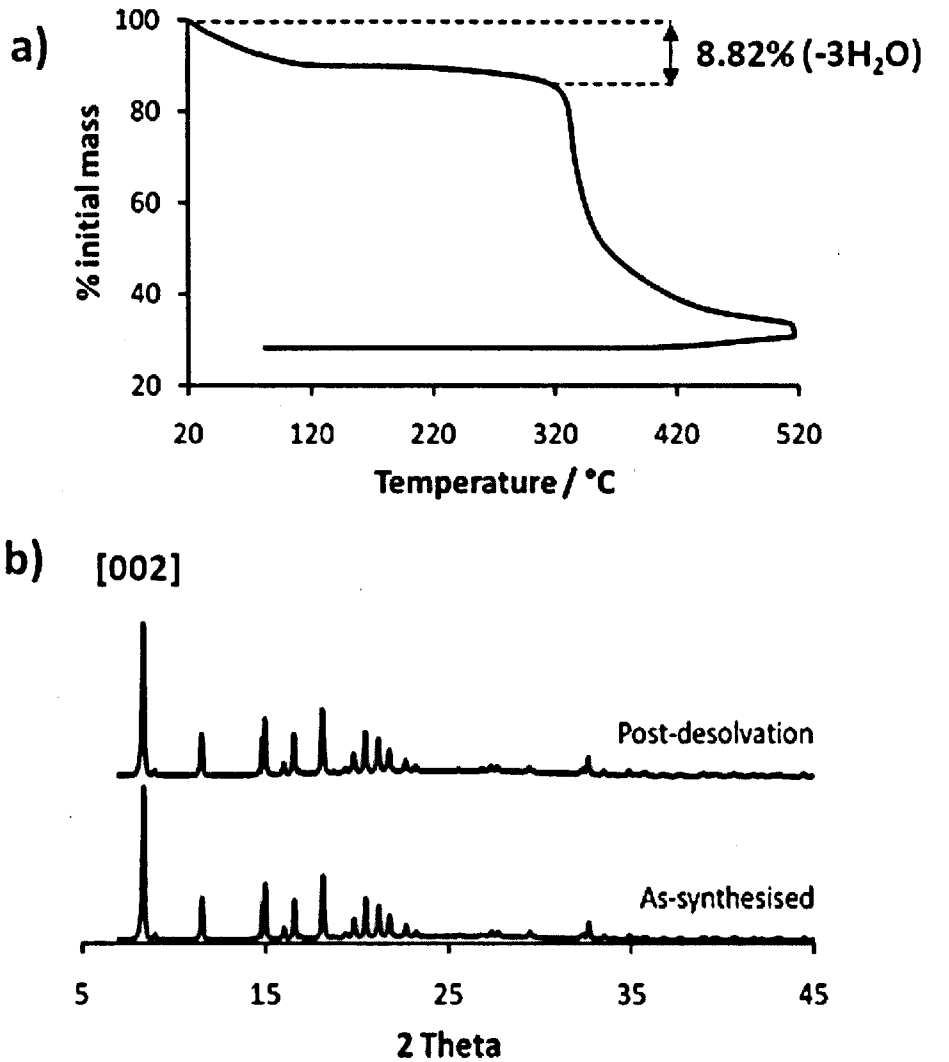

Figure 3.16. a) TGA data for 1 measured in an N_2 atmosphere. The weight loss of 8.82% between room temperature and 150 °C is attributed to the loss of the three water molecules which occupy the channels of 1. b) The PXRD pattern of $[Zn_2(IDS)(bipy)]$ as-synthesised and after the guest water molecules have been removed heating to 100 °C.

The permanent porosity of $[Zn_2(IDS)(bipy)]$ is demonstrated by a CO_2 sorption isotherm measured at 195K, in which typical type I behaviour for a microporous material is observed (Figure 3.17). The isotherm also showed that the mass uptake of CO_2 at saturation was 12%, and the BET derived surface area is 183(7) $m^2\ g^{-1}$ (determined from 26 data points in the range P/P_0 = 0.01-0.27). The observed hysteresis upon desorption of CO_2 from the framework arises from the slow

adsorption kinetics at 195 K (> 60 minutes per data point, saturation time approximately 12 hours), rather than specific structural change, as there was no evidence for this from PXRD. The final isotherm point upon desorption does not return to zero uptake due to temperature instabilities at very low relative pressures resulting from the prohibitively slow kinetics. The slow kinetics of uptake of CO_2 led to equilibration times greater than 60 minutes, which led to a saturation time of roughly 12 hours. The material was found to be non-porous to N_2, behaviour which is not uncommon in MOFs prepared with bipy with pore sizes of the scale of $[Zn_2(IDS)(bipy)]$.[22]

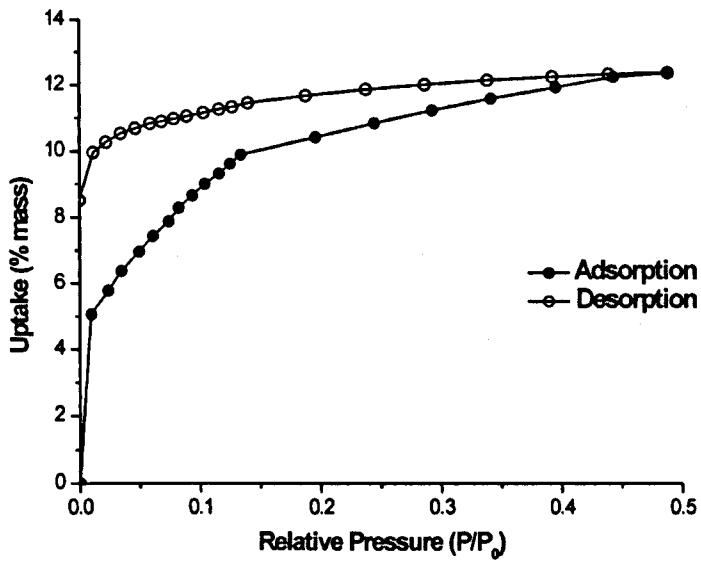

Figure 3.17. The adsorption isotherm of $[Zn_2(IDS)(bipy)]$ measured at 195K. The saturation of CO_2 corresponds to a mass uptake of 12%, and the BET surface area was determined to be 183(7) m^2 g^{-1}. The final isotherm point upon desorption does not return to zero uptake due to temperature instabilities at very low relative pressures resulting from the prohibitively slow kinetics.

In summary, we report that the combination of $ZnCO_3$, aspartic acid and bipy at a ratio of 1:2:1 under slightly acidic solvothermal conditions promotes the *in-situ* ligand transformation with the coupling of two $aspH_2$ molecules to generate the tetra-carboxylate, IDS. The formed IDS ligand is captured via metal coordination in a framework with a bipy co-ligand, generating new porous three-dimensional framework, $[Zn_2(IDS)(bipy)]$. The process is unique to Zn(II), not observed in analogous reactions with divalent cobalt, nickel or copper as evidenced by powder X-ray diffraction. This is surprising as the $[M(asp)(H_2O)_2]\cdot H_2O$ divalent salts are formed for all three metals. This may be due to the greater Lewis acidity of Zn(II), allowing conversion of aspartic acid to iminodisuccinic acid and the ability of Zn(II) to adopt distorted coordination geometries, a requirement for the formation of this framework. The structure was solved from a crystal which displayed a combination of twinning and disorder. This work highlights the crucial role rigid organic pillars play in generating porosity in metal-amino acid derived extended structures as they prevent complete filling of the available space by the highly flexible amino acid linkers.

3.4 A homochiral 3D zinc aspartate framework that displays multiple coordination modes and geometries

3.4.1 Synthesis

The solvothermal reaction of $ZnCO_3 \cdot 2ZnO \cdot 3H_2O$, L-asp$H_2$ and bipy in a water/methanol mixture yields X-ray quality crystals of the homochiral framework, [Zn(L-asp)]•guests. The material crystallises in the chiral monoclinic space group $P2_1$, with a Flack parameter close to zero, demonstrating that the structure contains only one enantiomer of asp. The structure is 3-dimensionally connected, and is comprised of three zinc centres in distinct coordination geometries that are linked together by three symmetry inequivalent asp molecules, all of which are in different conformations (Figure 3.19). This feature is novel, as all previous examples of metal-asp structures within the CSD only display one type of asp conformation (the tridentate O-N-O chelate), and a single coordination geometry (an octahedron). The final product of the solvothermal reaction was also found to contain an amorphous gel phase, which could not be characterised by PXRD, therefore a second method of synthesising a single phase bulk sample was achieved by refluxing aspH_2 with $ZnCO_3$ in a 1:1 molar ratio, in a water/methanol mixture (2:3 volumetric ratio). The phase purity of the resulting material was confirmed by elemental analysis (analysis (%): found (calc. for Zn_3(L-asp)$_3$•$2H_2O$) C = 23.21 (23.04), H = 2.91 (3.06) N = 6.68 (6.72)), and a Le Bail fit of the PXRD. The material also displays homogeneous platelet morphology of the material under examination using SEM (Figure 3.18), a feature which is consistent with the mosaicity of the crystals used in single crystal X-ray diffraction.

a)

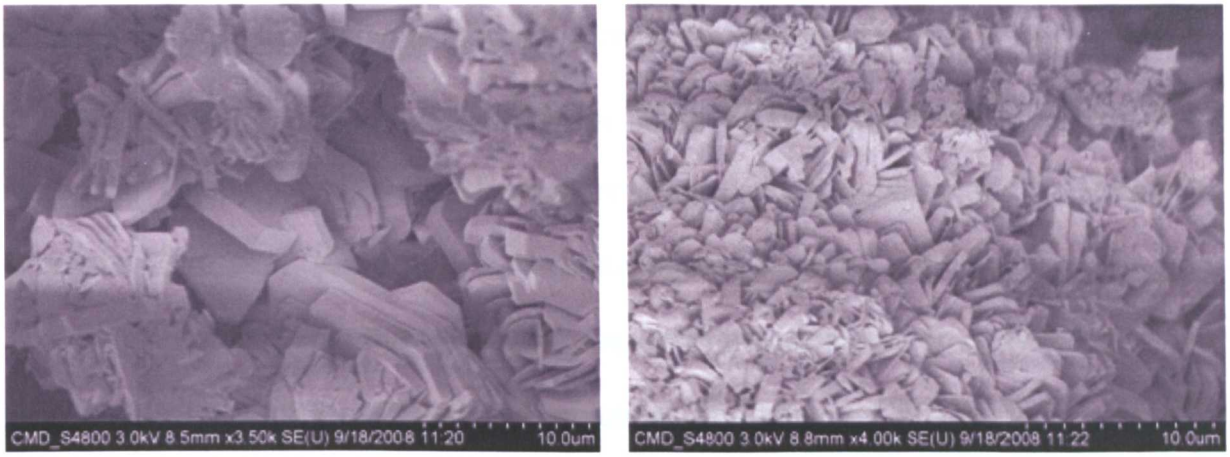

b)

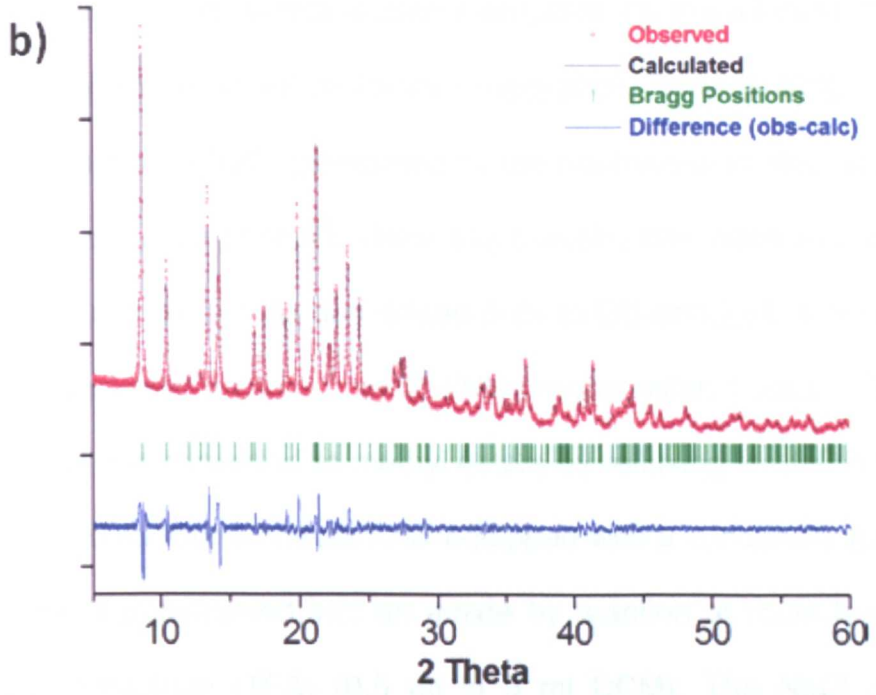

Figure 3.18. a) SEM pictures of [Zn(asp)] materials synthesised using the reflux method. b) The Le Bail fit of the bulk material. Refined cell parameters: *a* = 8.4909(4), *b* = 10.4995(5), *c* = 10.2201(6), *β* = 95.8782(44). Single crystal cell parameters (150K): *a* = 8.4655(61), *b* = 10.4763(77), *c* = 10.1813(75) *β* = 93.531(12).

The bulk enantiopurity of the reflux synthesis of [Zn(L-asp)] was determined by isolating $aspH_2$, and derivatisated for chiral gas-chromatography (GC), using the following method developed for assessing the bulk chirality of the $[M_2(L\text{-}asp)_2(bipy)]$ materials.[5] Firstly, $aspH_2$ was extracted from the bulk material by adding 1M NaOH (4 ml) to [Zn(L-asp)] (~ 30 mg), and removing the resulting precipitate by filtration. The addition of NaOH to the framework results in the precipitation of $Zn(OH)_2$, which is insoluble in weak basic aqueous solution, and removal of the solid leaves L-$aspNa_2$ in the filtrate. The filtrate is then neutralised by the addition of 1M HCl, and the aqueous solvent removed by rotary evaporation. The resulting white solid is a mixture of L-$aspH_2$ and NaCl (generated by the neutralisation step) as confirmed by elemental analysis and ^1H NMR. Once the L-$aspH_2$ has been recovered from the bulk framework sample, it was derivatised prior to GC analysis, a necessary step to prevent damage to the column from OH/NH groups within L-$aspH_2$. The carboxylic acid groups are first converted to methyl esters by refluxing in MeOH (4ml) and HCl (4M, 1ml) in a 20 ml round-bottom flask equipped with a condenser for 4 hours. The primary amine is transformed into an amide by reaction at room temperature with trifluoroacetic anhydride (TFA) (0.5 ml in 5 ml DCM). The NaCl present in the mixture does not interfere with either of the two steps of the derivatisation procedure and is not removed until the very end, when the Asp(OMe/TFA) derivative is dissolved in dichloromethane (DCM) and the NaCl is simply filtered off. The solution concentration for GC analysis is 0.5% (w/v) Asp(OMe/TFA) in DCM, and is carried out using a Lipodex-E capillary-GC column at 120°C.

3.4.2 *Structure of [Zn(L-asp)]*

The asymmetric unit of [Zn(L-asp)] contains three distinct Zn(II) ions that are 6-, 5- and 4-coordinate, and are distorted away from the ideal geometries of an octahedron (Zn1), a trigonal-bipyramid (Zn2), and a tetrahedron (Zn3) respectively (Figure 3.19). The coordination sphere of Zn1 contains 3 L-asp ligands, one bound *via* a tridentate O-N-O chelation, the second *via* a bidentate N-O chelation and the third by a single oxygen coordination from an L-asp side chain carboxylate group. The coordination sphere of Zn2 contains 4 L-asp ligands. One bound *via* a bidentate N-O chelation and the others *via* single oxygen coordination from 3 distinct L-asp side chain carboxylate groups. Zn3 contains 4 L-asp ligands, all coordinated *via* single oxygen coordination from 4 distinct L-asp side chain carboxylate groups .Although the coordination range of zinc is well established,[16] there are currently only 6 examples of single ligand extended structures in the CSD, which contain 4-, 5- and 6-coordinate Zn(II) ions within the same compound. However, [Zn(L-asp)] is the first example of a chiral, amino acid-derived compound with this structural motif.

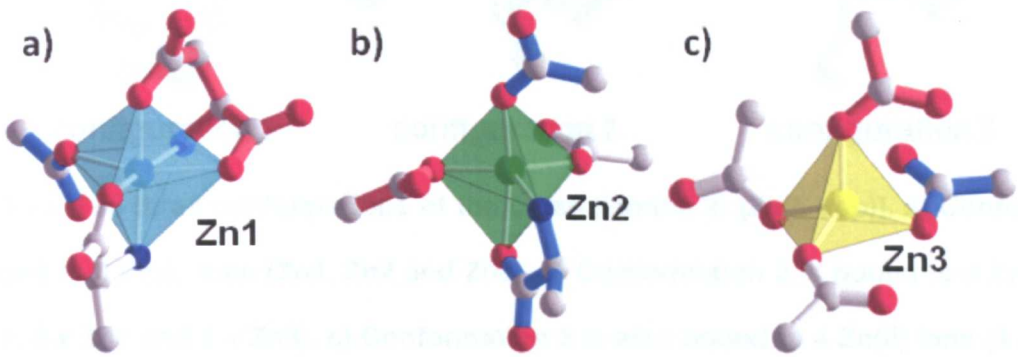

Figure 3.19. The three coordination geometries of Zn in [Zn(L-asp)]. a) The octahedral Zn1, b) the trigonal-bipyramidal Zn2, and c) the tetrahedral Zn3. Zinc1 is cyan, zinc2 is green, zinc3 is yellow, carbon is grey, oxygen is red and nitrogen is blue. The different coloured bonds within the L-asp molecules correspond to different conformations within the crystal structure. Hydrogen bonds are removed for clarity.

In [Zn(L-asp)], there are three crystallographically inequivalent L-asp molecules, which exist in three conformations that bind to Zn(II) in three different modes (Figure 3.20). Conformation 1 is bound to 3 Zn(II) ions, and displays two types of coordination; i) a tridentate chelation comprised of a 5- and a 6-membered N-O metallacycle, commonly reported with metal-asp structures, and ii) where the oxygen atoms not involved in the chelation to Zn bridge to neighbouring ions. Conformations 2 and 3 are both bound to 4 Zn(II) ions, and displays three types of coordination; i) the five-membered N-O metallacycle that is ubiquitous in metal-amino acid chemistry, ii) a pendant carboxylate group which bridges to other Zn(II) atoms, a feature noted with glutamic acid based materials[23-26] and iii) where the oxygen atoms not involved in the chelation to Zn bridge to neighbouring ions, analogous to conformation 1.

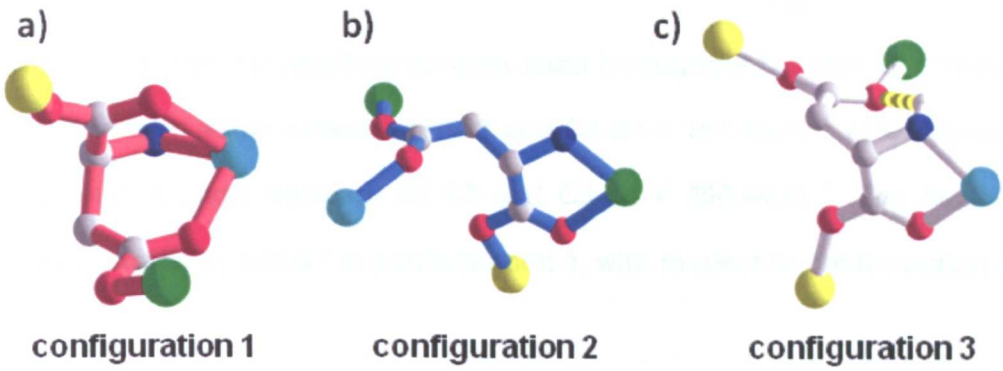

Figure 3.20. The three conformations of the L-asp ligands in [Zn(L-asp)]. a) Conformation 1 is bound to 3 Zn(II) ions (Zn1, Zn2 and Zn3). b) Conformation 2 is bound to 4 Zn(II) ions (1 *x* Zn1, 2 *x* Zn2 and 1 *x* Zn3). c) Conformation 3 is also bound to 4 Zn(II) ions (1 *x* Zn1, 1 *x* Zn2 and 2 *x* Zn3), and also displays an N-H···O intramolecular hydrogen bond, denoted by a dashed yellow line. Zinc1 is cyan, zinc2 is green, zinc3 is yellow, carbon is grey, oxygen is red and nitrogen is blue. The different coloured bonds within the L-asp molecules correspond to different conformations within the crystal structure. Hydrogen atoms not involved in hydrogen bonding are removed for clarity.

The difference in the shape of conformation 2 and 3 arises from the clockwise rotation of 144.9° in the -CH_2- carbon, C3, measured by the difference in the torsion angles between N1-C2 and C3-C4 within conformation 2 and 3. The rotation leads to the creation of an N-H···O intemolecular hydrogen bonding interaction within conformation 2 arising from the amine group and the side chain carboxylate group (Figure 3.21).

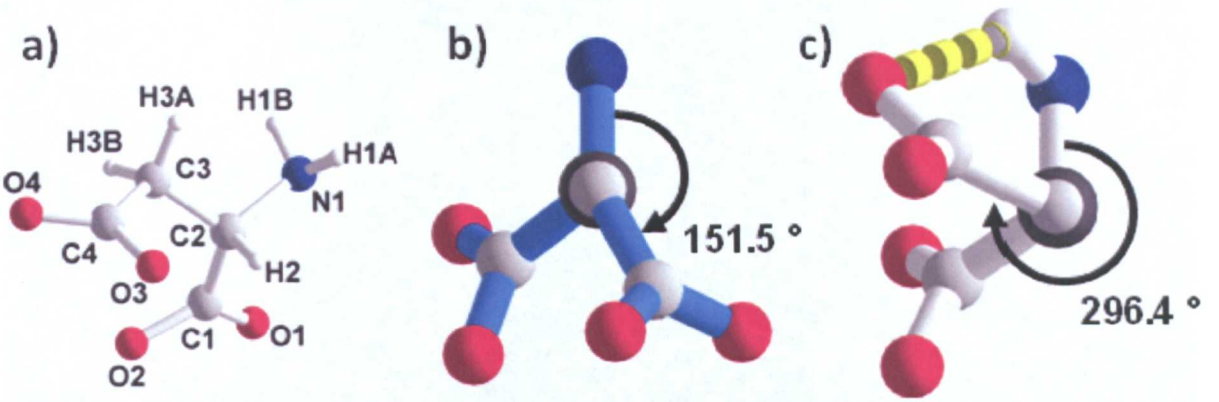

Figure 3.21 a) L-asp, and the labelling scheme used throughout the text. b) Conformation 2, which has a torsion angle between N1-C2 and C3-C4 = 151.49(4) °. c) Conformation 3, which has a torsion angle between N1-C2 and C3-C4 = 296.44(6) °. The flexible -CH_2- carbon, C3 has rotated by 144.9 ° in conformation 3, with respect to conformation 2.

The connectivity of the framework can be demonstrated by dissecting the crystal structure, to view the individual conformations of L-asp, and understanding how they connect *via* the different Zn(II) ions. Conformation 2 and Zn2 link together to form 1D chains along the *b* direction (Figure 3.22 a)). These chains are linked together by conformation 1 and Zn1, leading to the formation of a 2D layer in the *ab* plane (Figure 3.22 b)). Finally this is connected in the third dimension by conformation 3 and Zn3, leading to the 3D framework (Figure 3.22 d)).

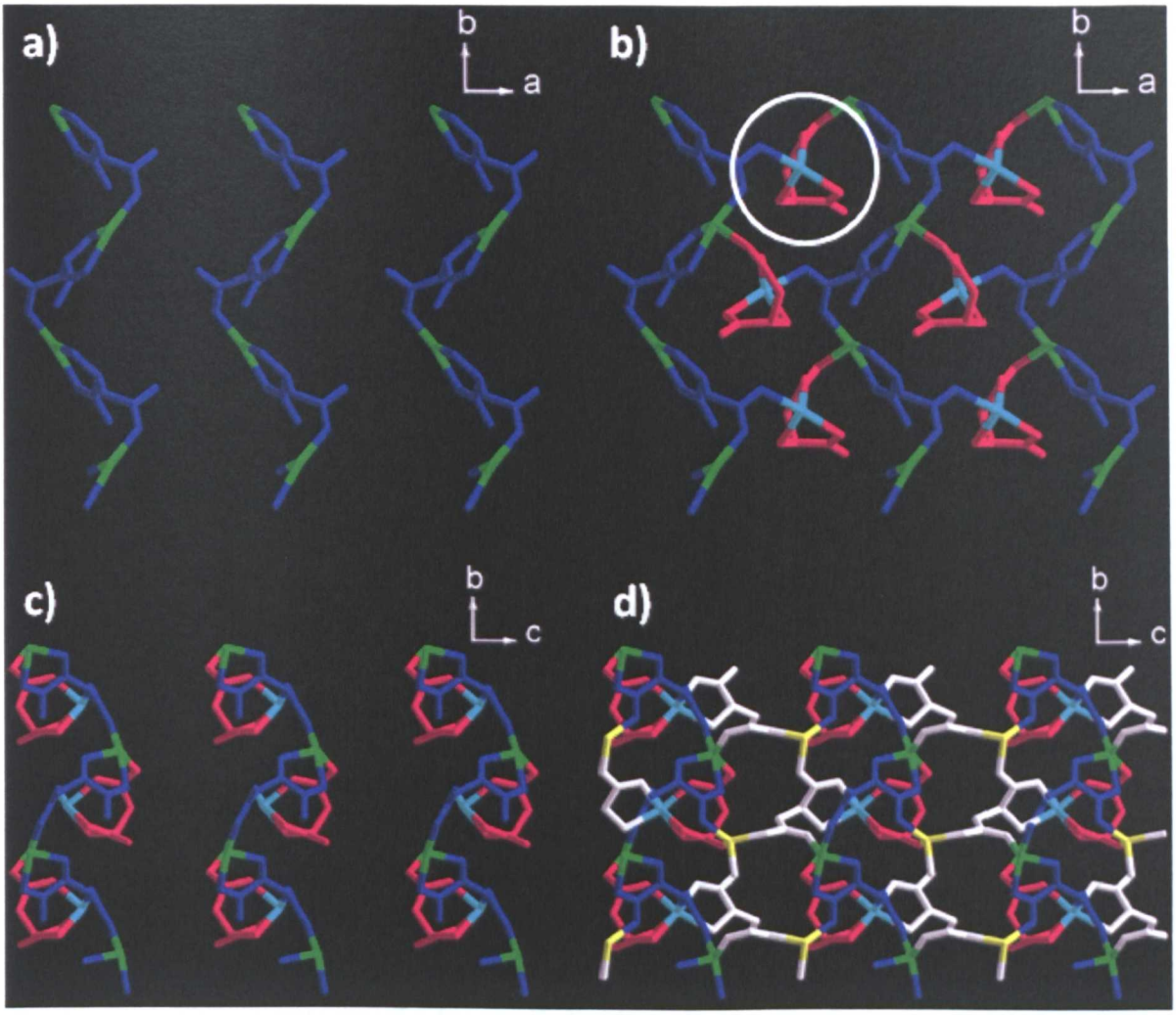

Figure 3.22 a) Conformation 2 (blue) chelates to Zn2 (green), *via* a 5-membered N-O metallacycle, and bridges to a second Zn2 through the carboxylic acid side chain of L-asp. This leads to the formation of infinite 1D chains along the *b* direction. b) These chains are linked along the *a* direction by tridentate chelation of conformation 1 (red) with Zn1 (cyan). Conformation 2 binds to Zn1 through the carboxylic acid side chain of L-asp, and conformation 1 is bound to Zn2 *via* the oxygen atom of the carboxylate group of the acidic side chain of L-asp (circled). This yields a 2D layer in the *ab* plane. c) Viewing three layers along [100] demonstrates that they are non-connected. d) The 3D network is completed by conformation 3 (white) and Zn3 (yellow). Conformation 3 chelates to Zn1, with the oxygen atom of the carboxylate bridging to Zn3 along *b*. The carboxylic acid side chain of asp from conformation 3 provides a bridge between Zn2 and Zn3 along *c*. Zn3 also provides links between conformation 1 and conformation 2 *via* oxygen atoms of the carboxylate groups that chelate to Zn1 and Zn2 respectively.

As noted previously, the Zn atoms within the structure are linked to either 3 (in the case of Zn1), or 4 (Zn2 and Zn3) asp moieties. Combined with the differing number of Zn atoms linked to conformations 1, 2 and 3 (3, 4 and 4 Zn atoms respectively), leads to the classification of this framework to be a 3,4-connected net. The application of topological analysis introduced in section 3.3.5 was unsuccessful in this case, as the structure contains six individual nodes (3 Zn, and 3 asp), and there are no other examples found in any of the available databases (Source = TOPOS Topological Database, version January 2009).[19]

3.4.3 NMR spectroscopy

The ^{1}H-^{13}C CP/MAS spectrum of aspartic acid (Figure 3.23) displays four resonances at 38.2, 54.2, 175.1 and 176.4 ppm with the peak assignment shown in the figure. The spectrum of [Zn(asp)] displays the same four resonances however, splitting of the lines and changes in chemical shift have been observed due to coordination to the zinc centres. The splitting of the resonances indicates the presence of crystallographically inequivalent conformations of asp, and the significant change of the chemical shift of the carbonyl resonances to higher ppm is due to strong binding to zinc.[27] The -CH- resonance is split into a ratio of 2:1 which is consistent with the presence of two different types of binding of asp to zinc in the same ratio, i.e. conformations 2 and 3 compared to 1. The more populated binding mode corresponds to the asp containing a pendant carboxylate group (ca. 51.5 ppm) and the less populated environment corresponds to the asp that contains a tridentate chelation comprised of a 5- and a 6-membered metallacycle. Further work is in progress to fully elucidate the exact assignment of the peaks.

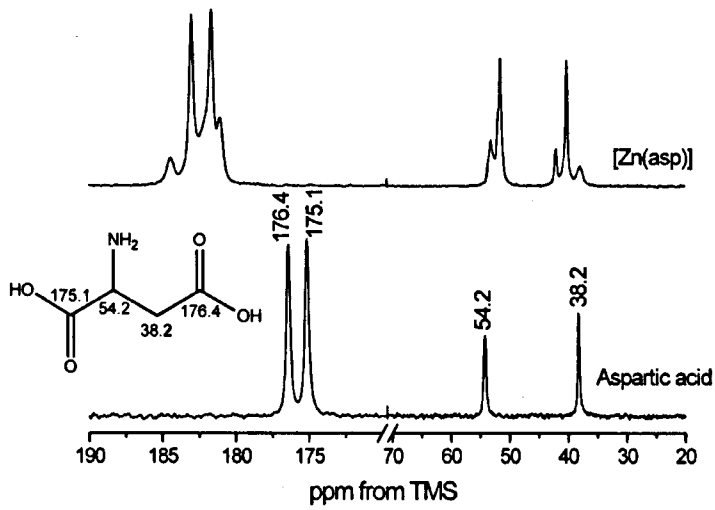

Figure 3.23. ^{1}H-^{13}C CP/MAS NMR spectra of aspartic acid and [Zn(asp)] recorded at a MAS rate of 10 kHz.

The crystal structure of [Zn(L-asp)] demonstrates that there are is one type of non-connected cavity, containing an encapsulated water molecule. Using the SQUEEZE routine within PLATON[20] establishes that the cavity has a volume of 33 $Å^3$, giving a total solvent accessible volume of 7.3%. The determined electron count of the structure without the water molecules included in the structural model is in good agreement with a crystallographic formula of $[Zn_3(L\text{-}asp)_3]\cdot H_2O$, which implies that the crystal is partially desolvated compared to the bulk analysis of the reflux sample, which elemental analysis determined to contain 2 water molecules. The stability of [Zn(L-asp)] was followed by TGA under a nitrogen flow (Figure 3.24). The framework displays a mass loss of 6.3% between 25 and 350 °C, which can be attributed to the release of the two encapsulated water molecules (calculated mass loss = 5.76%, found = 5.39%). Heating the framework beyond 350 °C results in a large mass loss, corresponding to the breakdown of the framework to ZnO and organic fragments, as confirmed by PXRD.

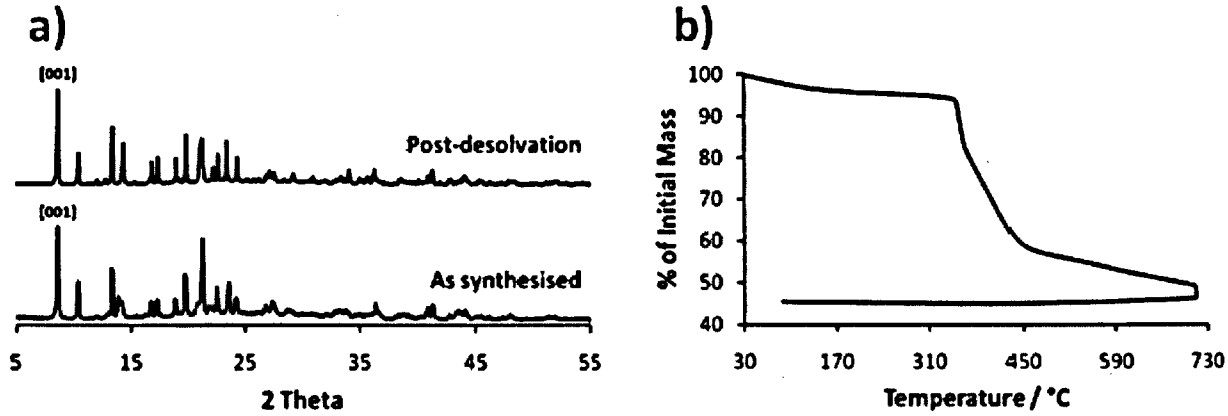

Figure 3.24. a) PXRD patterns for [Zn(L-asp)] showing the as synthesised experimental pattern (cell parameters (RT); *a* = 8.53, *b* = 10.58, *c* = 10.28, *β* = 93.6°) and after desolvation at 120 °C *en vacuo* (cell parameters (393K); *a* = 8.49, *b* = 10.49, *c* = 10.24, *β* = 96.5°). b) TGA of $[Zn_3(L\text{-}asp)_3]\cdot 2H_2O$. Initial mass loss in the temperature range 25-350 °C corresponds to that of the two encapsulated water molecules; expected (%) = 5.76, found (%) = 5.39. Second mass loss n the temperature range 350-700 °C corresponds to decomposition of the framework to ZnO + (organics); expected (%) = 60.96, found (%) = 53.40.

The removal of guests upon heating is surprising as the aperture of the windows to the cavities that contain the guest molecules are smaller than the van der Waals (vdW) radius of an oxygen atom (pore windows = 1.3 *x* 1.0 Å, oxygen vdW radii = 1.52 Å) (Figure 3.25 a and b)). In order for the guest molecules to leave the framework, it must rearrange and widen the pores. The narrow channels are further confirmed by a plot of the Connolly surface (Figure 3.25 c and d)), revealing one-dimensional channels containing cavities with cross-section = 3.10 *x* 2.5 Å, that are connected by narrow apertures of cross-section 1.3 *x* 1.0 Å. Despite this structural rearrangement upon desolvation, the crystallinity of the framework is retained upon removal of the guest molecules, as determined from PXRD of an evacuated sample

(*en vacuo* 120 °C, 12h) (FWHM [001]) as-synthesised = 0.123°, post-120 °C = 0.084°) (Figure 3.24).

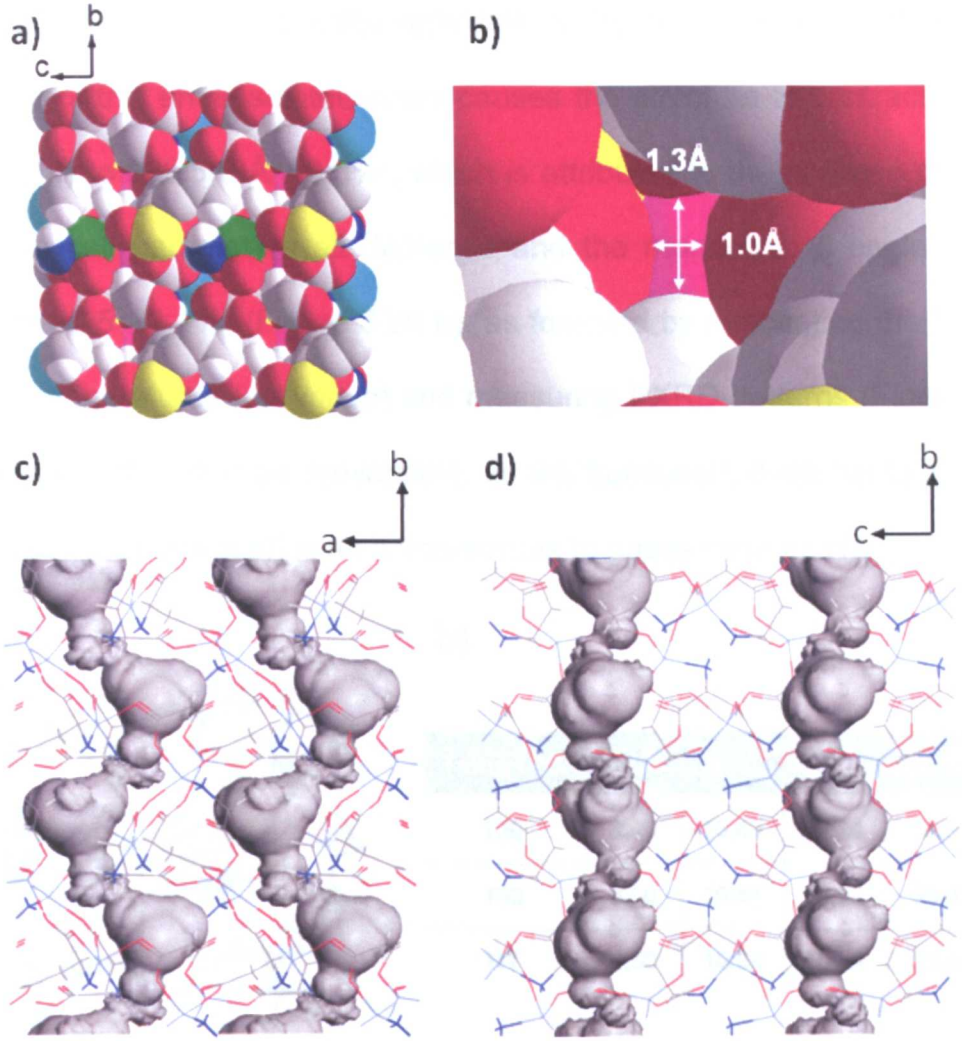

Figure 3.25. a) Space-filling plot of [Zn(L-asp)] along the *a*-axis, with the open space from the one-dimensional channels labelled in magenta. b) The aperture of a single channel, with dimension 1.0 *x* 1.3 Å. Atom labelling is the same as Figure 3.19. c) The Connolly surface plot of [Zn(L-asp)] viewed along the *c*-axis and along the *a*-axis (d). The channels are one-dimensional, sinusoidal in shape, with large cavities linked by narrow apertures Connolly surfaces created with a rolling ball radius of 1.52Å, equivalent to the van der Waals radius of an oxygen atom. The wireframe structure represents the framework of 1, the shaded grey region represents the Connolly surface.

The environment of the cavity is ideally suited for the guest water molecules, as it is lined by hydrogen and oxygen atoms, forming seven independent O···H hydrogen bonding interactions with the water molecule in the cavity centre (Figure 3.26 a). The removal of this encapsulated water causes the structure to contract in volume from 926.4(14) to 905.5(9)Å^3 (2.3%), which is attributed to the collapse of the open cavities. The cell parameters all decrease and the monoclinic β angle increases from 93.6 to 96.5° (3.1%) (Figure 3.26 b), as followed by evacuating the framework at different temperatures (*en vacuo*) and measuring PXRD patterns (Figure 3.26 c). The process was found to be irreversible, as the framework does not take up water or methanol vapour [Zn(asp)] is also non-porous to gases such as H_2.

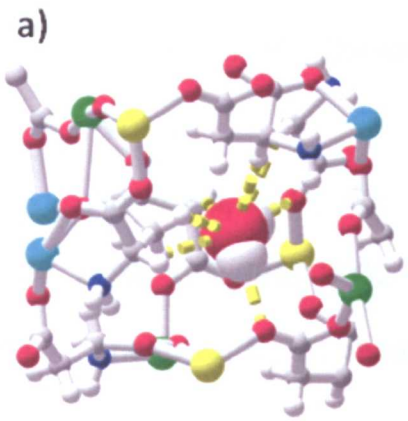

b)

Temp / °C	a / Å	b / Å	c / Å	β / °
120	8.49	10.49	10.24	96.5
100	8.50	10.51	10.22	95.8
RT	8.53	10.58	10.28	93.6

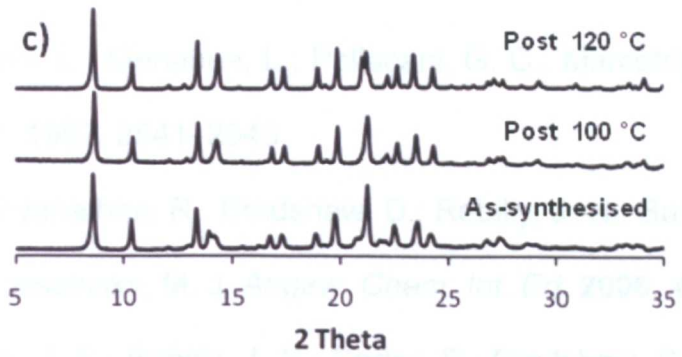

Figure 3.26. a) The environment of a single cavity within [Zn(L-asp)]. The central water molecule guest is held within the cavity by 7 O···H hydrogen bonding interactions (denoted by a broken yellow line) from the host framework. b) Cell parameters from variable temperature PXRD measurements, and c) PXRD patterns showing the change in cell parameters.

In summary, we report a novel homochiral zinc based material derived from aspartic acid. The framework contains multiple coordination geometries of zinc, which are distorted, multiple binding modes of aspartate to zinc, and three conformations of the ligand within the structure. The framework contains encapsulated water molecules which can be removed upon heating without loss in crystallinity, despite the guest size being larger than the cavity aperture. The release of the encapsulated guest results in irreversible collapse of the one-dimensional channels, as followed by PXRD.

3.5 References

(1) Laurie, S. H. *Comprehensive Coordination Chemistry*; Pergamon: Oxford, 1987; Vol. 2.

(2) Anokhina, E. V.; Go, Y. B.; Lee, Y.; Vogt, T.; Jacobson, A. J. *J. Am. Chem. Soc.* **2006**, *128*, 9957-9962.

(3) Anokhina, E. V.; Jacobson, A. J. *J. Am. Chem. Soc.* **2004**, *126*, 3044-3045.

(4) Antolini, L.; Menabue, L.; Pellacani, G. C.; Marcotrigiano, G. *J. Chem. Soc., Dalton Trans.* **1982**, 2541–2543.

(5) Vaidhyanathan, R.; Bradshaw, D.; Rebilly, J.-N.; Barrio, J. P.; Gould, J. A.; Berry, N. G.; Rosseinsky, M. J. *Angew. Chem. Int. Ed.* **2006**, *45*, 6495 –6499.

(6) Barrio, J. P.; Rebilly, J.-N.; Carter, B.; Bradshaw, D.; Bacsa, J.; Ganin, A. Y.; Park, H.; Trewin, A.; Vaidhyanathan, R.; Cooper, A. I.; Warren, J. E.; Rosseinsky, M. J. *Chem. Eur. J.* **2008**, *14*, 4521-4532.

(7) Ingleson, M. J.; Barrio, J. P.; Bacsa, J.; Dickinson, C.; Park, H.; Rosseinsky, M. J. *Chem. Commun.* **2008**, *11*, 1287-1289.

(8) Barrio, J. P.; Rosseinsky, M. J. *unpublished results.*

(9) Siemens *SAINT* **1995**, Siemens Analytical X-ray Instruments Inc., Madison,

Wisconsin, USA.

(10) Sheldrick, G. M. *SADABS* **2007**, Version 2007/2. University of Gottingen, Germany.

(11) Sheldrick, G. M. *Acta Crystallogr.* **2008**, *A64*, 112-122.

(12) Ferey, G. *Dalton Trans.* **2009**, *23*, 4400-4415.

(13) Polynova, T. N.; Chuklanova, E. B.; Porai-Koshits, M. A. *Dokl. Akad. Nauk* **1985**, *283*.

(14) Poznyak, A. L.; Antsishkina, A. S.; Sadikov, G. G.; Sergienko, V. S. *Russ. J. Inorg. Chem.* **1998**, *43*, 182-186.

(15) Feller, R. K.; Forster, P. M.; Wudl, F.; Cheetham, A. K. *Inorg. Chem.* **2007**, *46*, 8717-8721.

(16) Archibald, S. J. *Comprehensive Coordination Chemistry II*; Pergamon: Oxford, 2004; Vol. 6.

(17) Chui, S. S.-Y.; Lo, S. M.-F.; Charmant, J. P. H.; Orpen, A. G.; Williams, I. D. *Science* **1999**, *283*, 1148-1150.

(18) Ockwig, N. W.; Delgado-Friedrichs, O.; O'Keefe, M.; Yaghi, O. M. *Acc. Chem. Res.* **2005**, *38*, 176–182, and the Reticular Chemistry Structure Resource website at http://rcsr.anu.edu.au.

(19) Blatov, V. A.; Shevchenko, A. P.; Serezhkin, V. N. *Acta Crystallogr.* **2000**, *A33*, 1193. See also http://www.topos.ssu.samara.ru.

(20) Spek, A. L. *J. Appl. Cryst.* **2003**, *36*, 7-13.

(21) Webster, C. E.; Drago, R. S.; Zerner, M. C. *J. Am. Chem. Soc.* **1998**, *120*, 5509-5516.

(22) Fletcher, A. J.; Cussen, E. J.; Prior, T. J.; Rosseinsky, M. J.; Kepert, C. J.; Thomas, K. M. *J. Am. Chem. Soc.* **2001**, *123*, 10001-10011.

(23) Flook, R. J.; Freeman, H. C.; Scudder, M. L. *Acta Crystallogr.* **1977**, *B33*, 801-809.

(24) Gramaccioli, C. M. *Acta Crystallogr.* **1966**, *21*, 600–605.

(25) Gramaccioli, C. M.; Marsh, R. E. *Acta Crystallogr.* **1966**, *21*, 594–600.

(26) Zhang, Y.; Saha, M. K.; Bernal, I. *CrystEngComm* **2003**, *5*, 34–37.

(27) Ingleson, M. J.; Barrio, J. P.; Jean-Baptiste Guilbaud; Khimyak, Y. Z.; Rosseinsky, M. J. *Chem. Commun.* **2008**, 2680–2682.

Chapter 4 Glutamic acid-derived frameworks

4.1 Introduction

As noted within the previous chapter, transition metal-amino acid coordination compounds can display multiple structures depending upon the reaction conditions, and coordination preferences of the metal used within the synthesis. We were interested in using glutamic acid ($gluH_2$) as a building block for chiral frameworks, because it contains an acidic side chain analogous to aspartic acid ($aspH_2$) (Figure 4.1), allowing us to test the generality of our approach of incorporating amino acids into permanently porous metal-organic frameworks (MOFs) by reaction with rigid linkers such as 4,4'-bipyridyl (bipy). If the carboxylate group within the side chain could be utilised for additional connectivity, as with the M(asp) based structures, then it should be possible to synthesise a family of frameworks based upon this amino acid. $GluH_2$ contains an additional $-CH_2-$ group in the side chain, compared to $aspH_2$, which could be used to increase the flexibility of the structure, giving a greater degree of chiral recognition, or the extra length could generate larger pore sizes, yielding a wider range for chiral separation.

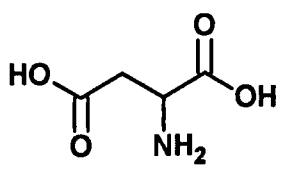

aspartic acid ($aspH_2$)

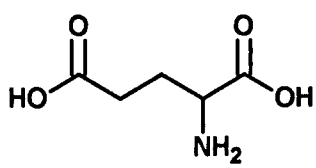

glutamic acid ($gluH_2$)

Figure 4.1. The structures of aspartic and glutamic acid.

Although the molecular structures of L-aspH_2 and L-gluH_2 are similar, the coordination chemistry of the two amino acids are very different. M(L-asp) compounds are dominated by the formation of a tridentate O-N-O chelate to a central metal ion comprised of a 5- and a 6-membered metallocycle.[1-6] However, with gluH_2 the formation of a 6-membered metallocycle is not possible, due to the additional -CH_2- within the side chain. Similar coordination would lead to the formation of a thermodynamically unfavourable 7-membered metallocycle, which is not found within any reported structures of M(L-glu) within the Cambridge Structural Database (CSD)[7] (version = CSDupdateMay09, 6 entries).[8-13] To date, four isostructural crystal structures of [M(L-glu)(H_2O)]•H_2O, (M = Cd,[9] Zn,[10] Cu,[11] and Co[13]) have been reported, and the magnetic properties of the Co framework have been explored. Within the structure of M(L-glu), L-glu displays the following three coordination modes; i) the 5-membered N-O metallocycle that is prevalent within metal-amino acid compounds,[14] ii) single oxygen binding to a neighbouring metal centre from the carboxylate group within the metallocycle, and iii) where the two oxygen atoms of the acidic side chain form a 4-membered bidentate chelation to M (Figure 4.2). This leads to the formation of a three-dimensional framework with coordinated water and a single water molecule within one-dimensional channels.

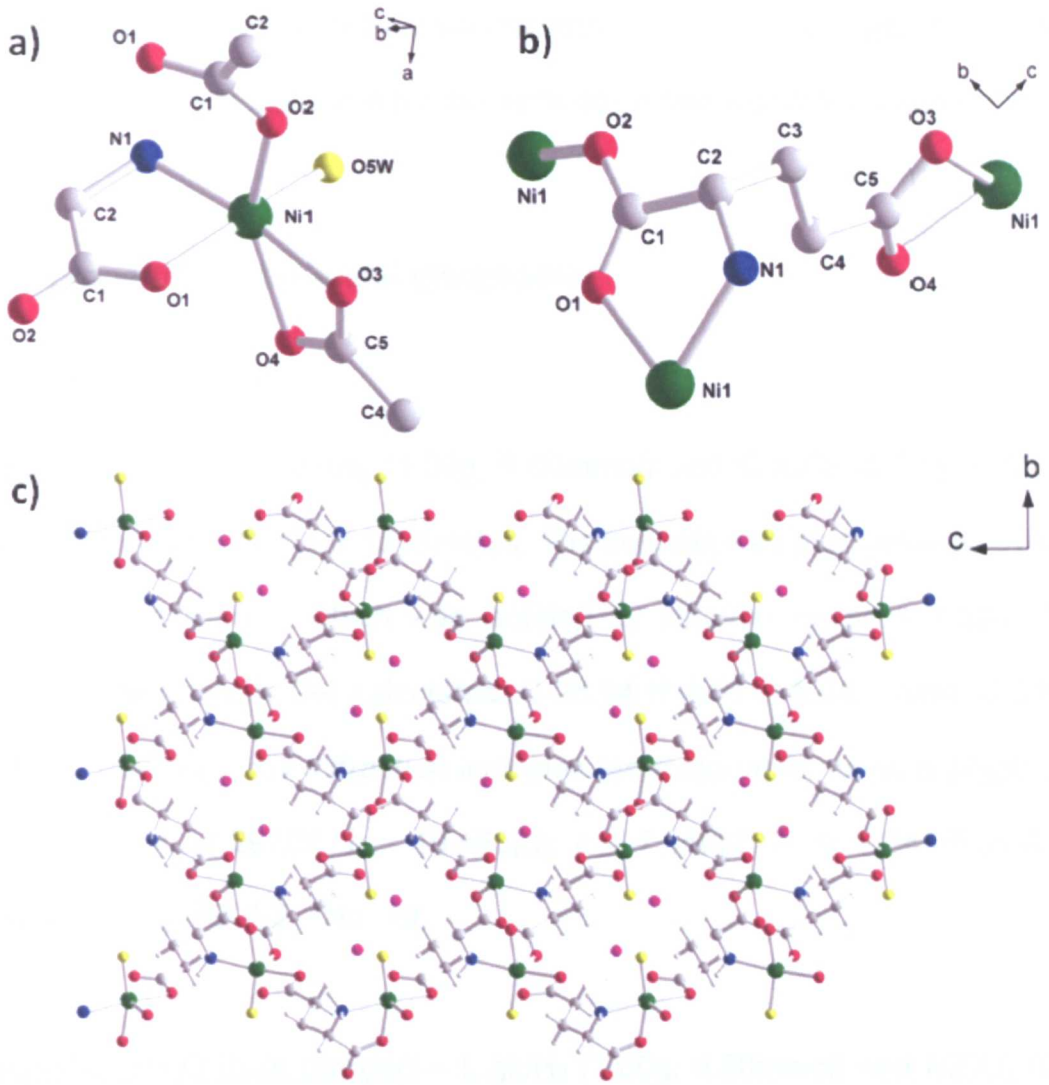

Figure 4.2. a) The coordination sphere of Ni within [Ni(L-glu)(H_2O)]•H_2O. Ni is bound to 3 glu ligands and a single water molecule, adopting a distorted octahedral geometry with angles between ligand atoms ranging from 60.05(0) (O3-Ni1-O4) to 113.91(1)° (O4-Ni1-N1). Hydrogen atoms are removed for clarity. b) The three binding modes of glu to Ni. i) 5-membered N-O metallocycle, ii) the second oxygen atom from the carboxylate (O2) in the metallocycle bridges to a second metal centre, resulting in a *syn-anti* carboxylate bridging mode, and finally iii) bidentate chelation from the two oxygen atoms of the second carboxylate (O3 and O4) to Ni. Hydrogen atoms are removed for clarity. c) The extended structure of [Ni(L-glu)(H_2O)]•H_2O viewing along the *a*-axis. The coordinated and the encapsulated water molecules (yellow and magenta respectively) can be noted within the structure. Ni is dark green, oxygen is red, nitrogen is blue and carbon is grey. Hydrogen atoms are white. Hydrogen atoms removed from water molecules for clarity.

The properties of the M(L-glu) frameworks and the formation of glu based mixed-ligand MOF materials is the basis for the work described within this chapter.

4.2 The properties of the metal glutamates

4.2.1 Synthetic protocols

[Co(L-glu)(H_2O)]•H_2O – L-gluH_2 (1.00g, 6.80mmol) and $CoCO_3$ (0.81g, 6.80mmol) were stirred in water (30ml) for 10 minutes. The solution was then refluxed overnight to yield a burgundy solid, which was isolated by filtration (mass = 1.22g, 74.5% yield). Elemental analysis (%) calculated: C 25.54 H 4.51 N 5.64; found: C 24.88 H 4.57 N 5.74. Powder X-ray diffraction indicates the material forms as a single phase orthorhombic, a = 11.297(3), b = 10.468(3), c = 7.150(2) Å, V = 845.5(3) Å^3, T = 298K, space group $P2_12_12_1$ (No. 19).

[Ni(L-glu)(H_2O)]•H_2O (bulk powder) – L-gluH_2 (1.00g, 6.80mmol) and $NiCO_3$ (0.81g, 6.80mmol) were stirred in a water/methanol solution (1:1, 50ml) for 30 minutes. The solution was then refluxed overnight and yielded a lime green solid, which was isolated by filtration (mass = 1.20g, 73.7% yield). Elemental analysis (%) calculated: C 25.04 H 4.62 N 5.84; found: C 25.15 H 4.63 N 5.79. Powder X-ray diffraction indicates the material forms as a single phase orthorhombic, a = 11.165(3), b = 10.393(3), c = 7.159(2) Å, V = 830.8(6) Å^3, T = 298K, space group $P2_12_12_1$ (No. 19).

[Zn(L-glu)(H_2O)]•H_2O – L-gluH_2 (2.00g, 13.60mmol) was dissolved in H_2O (50ml) by heating to 90 °C. To this solution, basic zinc carbonate (1.54g, 4.4mmol) was added, immediately causing a white precipitate to form, which was isolated by filtration

(mass = 3.272g, 97.6% yield). Elemental analysis (%) calculated: C 24.36 H 4.50 N 5.68; found: C 23.88 H 4.35 N 5.58. Powder X-ray diffraction indicates the material forms as a single phase orthorhombic, a = 11.173(2), b = 10.464(2), c = 7.213(2) Å, V = 843.3(5) Å^3, T = 298K, space group $P2_12_12_1$ (No. 19).

[Ni(L-glu)(H_2O)]•H_2O (single crystals) – L-gluH_2 (0.100g, 0.68mmol) and $NiCO_3$ (0.081g, 0.680mmol) were stirred in a water/methanol solution (1:1, 5ml) for 30 minutes. The solution was then transferred to a 23ml Teflon lined solvothermal vessel, and heated at 100 °C overnight. Heating rate = 2 °C min^{-1}, time at 100 °C = 18 hours, cooling rate = 1 °C min^{-1}. This yielded green single crystals, suitable for X-ray diffraction. *Crystal data* for [Ni(L-glu)(H_2O)]•H_2O: $Ni(C_5H_7NO_4)(H_2O)_2$, M = 239.86, green prisms, 0.10 × 0.10 × 0.10 mm^3, orthorhombic, a = 7.139(1), b = 10.343(2), c = 11.135(2) Å, V = 822.2(3) Å^3, T = 100(2)K, space group $P2_12_12_1$ (No. 19), Z = 4, 4322 reflections collected, 1858 unique (R_{int} = 0.0364). Final *GooF* = 0.785, *R1* = 0.0257, *wR2* = 0.0363, *R* indices based on 1858 reflections with I>2sigma(I) (refinement on F^2), absolute structure parameter = -0.002(13).

4.2.2 Porosity studies

As noted from the crystal structure of [Ni(L-asp)(H_2O)]•H_2O in Figure 4.2 and the elemental analysis, M(L-glu) materials contain two water molecules: one bound to the central metal ion, and a second held within the cavities of the framework. Measuring the mass loss upon heating using thermogravimetry in flowing N_2, demonstrates that the encapsulated and the coordinated H_2O molecules within the structure are removed prior to decomposition, as signified by a plateau after a mass loss of approximately 15% for all the materials. A large mass loss follows at higher

temperature (M = Co: T = 250 °C, Ni: T =350 °C, Zn: T = 250 °C), corresponding to the decomposition of the structure to the metal oxide + organics. However, another feature of the M(L-glu) materials is the behaviour upon H_2O removal from the frameworks, which is dependent upon which metal is in the structure. When M = Co or Zn, the associated mass loss from the coordinated water molecule and the encapsulated guest is lost within a single step. However, with the Ni analogue, the mass loss for the coordinated and the encapsulated guest are distinctly different, implying that the encapsulated water can be removed from the structure with the coordinated water intact (Figure 4.3). Additionally, a second mass loss is observed within the Co and the Zn based materials that correspond to a third water molecule. This could be due to an intermolecular rearrangement of the L-glu within the structure, leading to the formation of L-pyroglutamic acid (see section 4.3.1), however any attempts to isolate the material after the removal of a third water molecule was unsuccessful.

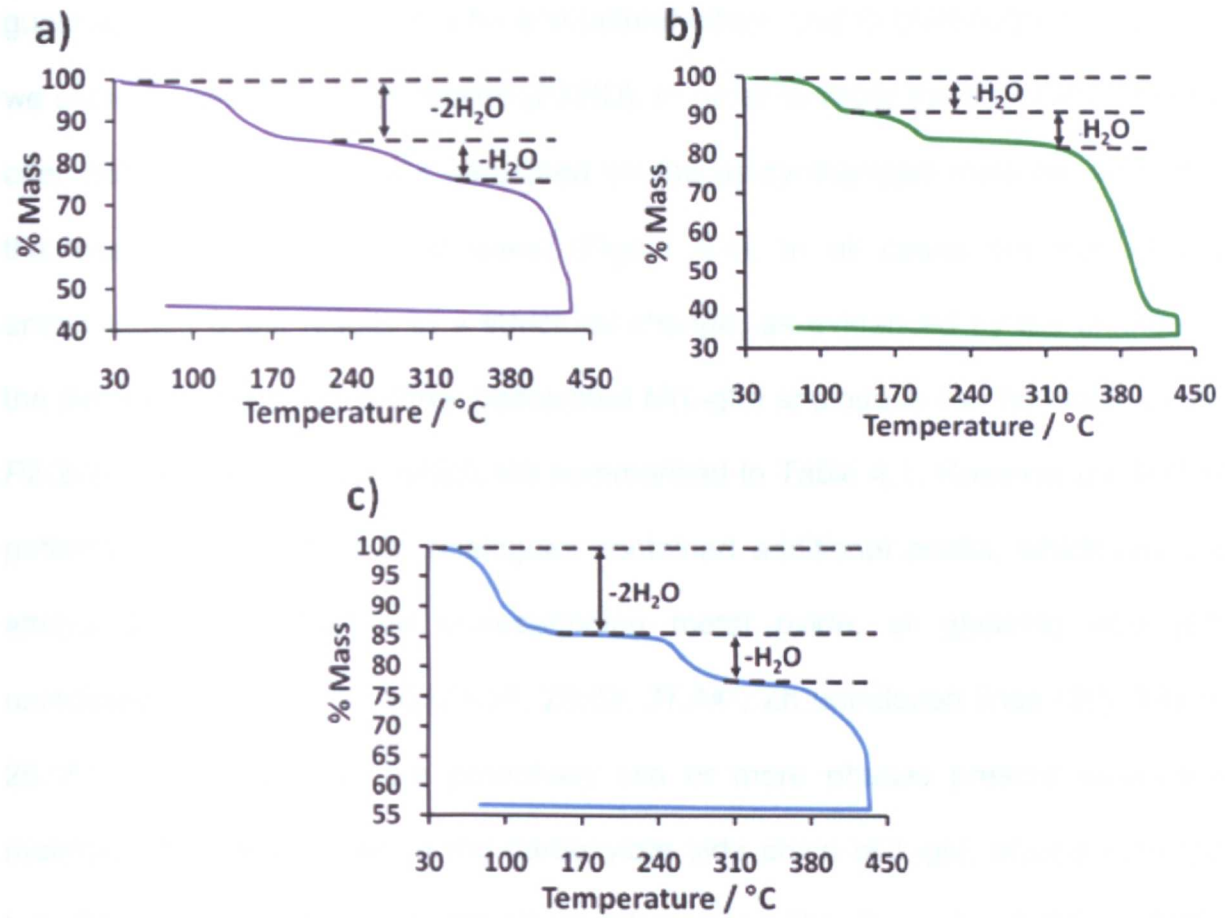

Figure 4.3. Thermogravimetric analysis of a) Co(L-glu)(H_2O)]•H_2O, b) Ni(L-glu)(H_2O)]•H_2O and c) Zn(L-glu)(H_2O)]•H_2O in N_2. Both the encapsulated and coordinated water molecules are lost together in one step within the Co and the Zn based structure. However, for the Ni analogue, there are two clear steps within the mass loss profile, corresponding to distinct removal of the encapsulated and the coordinated water molecules.

This result is not consistent with other Ni based MOFs with coordinatively bound H_2O, such as CPO-27, which can be synthesised as either a Ni[15] or a Co[16] analogue. Comparative to M(L-glu), H_2O is coordinated to a metal centre, and is also located within the pores of the open framework, but in contrast to M(L-glu), heating the material under flowing N_2 results in the removal of the solvent within the pores concurrent with the removal of coordinatively bound H_2O in both the Ni and Co analogues. This effect of the stepwise removal of encapsulated and coordinated

guest molecules must therefore be a structural effect, and to investigate this further, we utilised powder X-ray diffraction (PXRD). In order to verify the structural integrity after desolvation, PXRD was measured on the as-synthesised material, and after the loss of the encapsulated guest (Figure 4.4). In all cases the loss of the encapsulated guest results in a structural change, as evidenced by the change in the diffraction patterns. All three desolvated M(L-glu) analogues can be indexed to a $P2_12_12_1$ cell, the results of which are summarised in Table 4.1. However the PXRD patterns for the Co and Zn analogues contained additional peaks, which are not attributed to M(L-glu), the corresponding metal oxide, or glutamic acid (Co unindexed lines (2θ): 19.10, 21.19, 26.62, 37.44°; Zn unindexed lines (2θ): 13.80, 26.35°), indicating there are potentially two or more phases present within the material. The flexibility within the carboxylate side chain of L-glu, arising from the two -CH_2- groups is the key to the structural change within the material. Within CPO-27, the polydentate organic linker is 2,5-dihydroxyterephthalate (dhtp), containing only carbons that are sp^2 hybridised, incapable of rotations to adjust torsion angles within the ligand, and allow the structure to change to uptake or release, which is evident upon the small change in cell parameters upon desolvation (as-synthesised: rhombohedral, a = 25.79, b = 25.79, c = 6.77 Å, γ = 120°; post-desolvation: rhombohedral, a = 25.98, b = 25.98, c = 6.69 Å, γ = 120°). In contrast within L-gluH_2, the bidentate carboxylate chelation, which serves as a bridge between metal centres, contains two sp^3 hybridised carbons that can rotate and change the torsion angles within the ligand, allowing the structure to contract upon guest removal. This effect, combined with the change in coordination geometry upon guest loss, allows significant degrees of movement with the M(L-glu) materials, and accounts for the change in lability in Ni, compared to Co and Zn. Co(II) is d^7, and can adopt a range

of geometries due to little preference in the ligand field stabilisation energies within this configuration. Therefore, changing the geometry, and the configuration to either pseudo-square pyramidal, or pseudo-trigonal bipyramidal (upon loss of the H_2O ligand), will have no major effect upon the stabilisation of the ion. Similarly for d^{10} Zn(II), for which the coordinative flexibility was already established in the previous chapter, a change in the geometry to pseudo-square pyramidal, or pseudo trigonal pyramidal does not have a large effect upon the stability of the ion, since the energy barrier for this change is low and easily overcome at the temperature required to remove the encapsulated H_2O. In contrast, d^8 Ni(II) is most stable in octahedral or square planar environments. Although, Ni(II) does adopt 5-coordinate geometries,[17-20] the ligands involved are typically bulky and chelating, with the choice between square pyramidal, and trigonal pyramidal geometries is dependent upon the steric and electronic effects of the complex. One possible explanation for the stepwise removal of the encapsulated and coordinated H_2O, is that upon desorption of the guest, the structure rearranges, causing a change in the geometry of the metal, and increasing the lability of the H_2O ligand, allowing its removal.

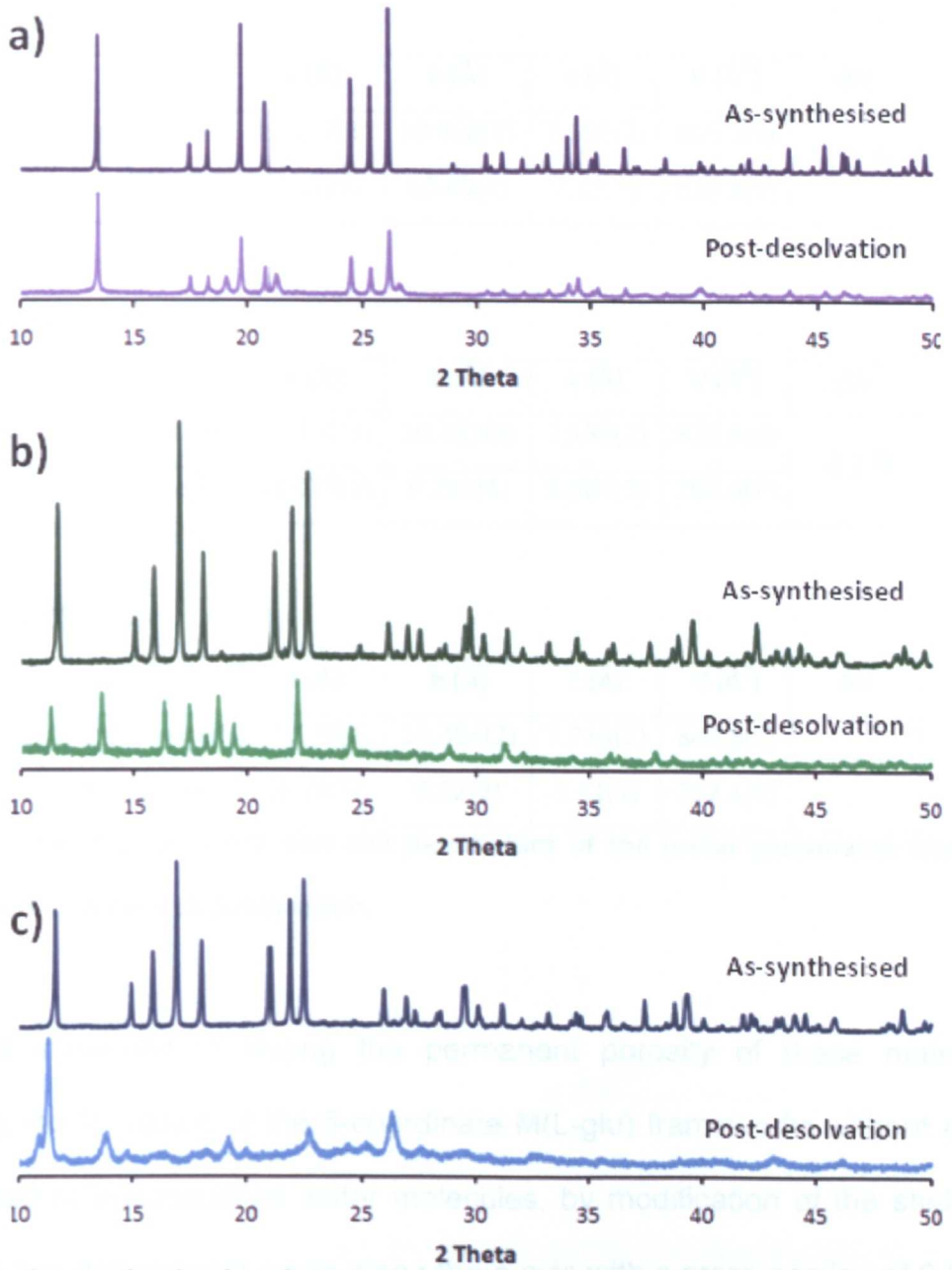

Figure 4.4. As-synthesised and post-desolvation PXRD of a) Co(L-glu)(H_2O)]•H_2O, b) Ni(L-glu)(H_2O)]•H_2O and c) Zn(L-glu)(H_2O)]•H_2O. With each material the loss of encapsulated guest is coupled with a change in the structure, as evidenced by the change in the powder patterns.

[Co(L-glu)(H_2O)]•H_2O

	a (Å)	b (Å)	c (Å)	V (Å^3)	ΔV
As-synthesised	11.297(3)	10.468(3)	7.150(2)	845.5(3)	-0.7 %
Desolvated	11.26(5)	10.45(4)	7.13(3)	839.3(9)	

[Ni(L-glu)(H_2O)]•H_2O

	a (Å)	b (Å)	c (Å)	V (Å^3)	ΔV
As-synthesised	11.165(3)	10.393(3)	7.159(2)	830.8(6)	-8.2 %
Desolvated	13.070(5)	9.783(4)	5.964(3)	762.6(7)	

[Zn(L-glu)(H_2O)]•H_2O

	a (Å)	b (Å)	c (Å)	V (Å^3)	ΔV
As-synthesised	11.173(2)	10.464(2)	7.213(2)	843.3(5)	-5.5 %
Desolvated	15.76(5)	9.52(2)	5.31(1)	797.1(5)	

Table 4.1. The change in the unit cell parameters of the metal glutamates from the as-synthesised materials to desolvation.

We were interested in testing the permanent porosity of these materials, as modelling the formation of the 5-coordinate M(L-glu) frameworks without either the coordinated or encapsulated water molecules, by modification of the shelx res file results in one-dimensional pores along the *a*-axis with a cross-section of 6.25 *x* 1.63 Å, leading to 12% solvent accessible volume (calculated using the SQUEEZE routine within PLATON[21]). In order to test the permanent porosity of these materials, the N_2 isotherms of the Ni and the Zn analogues were measured to 1 bar at 77K. Each sample was activated by heating at 100 °C at 10^{-7} mbar until constant mass was reached, typically overnight, ([Ni(L-glu)(H_2O)]•H_2O: 15.32%, [Zn(L-glu)(H_2O)]•H_2O: 15.25%). However, each sample displayed IUPAC type II isotherm behaviour, indicating that N_2 sorption only takes place on the external surface of the

materials (Figure 4.5). The reduction in the cell volume upon removal of the guest appears to cause collapse of the internal cavities. This is most likely due to the flexible -CH_2- groups within the side chain of glu rearranging to minimise the open space within the framework in accordance with the structural change discussed previously. In order to produce a permanently porous framework, we attempted to synthesise a M-glu material, incorporating a rigid linker such as 4,4′-bipyridyl (bipy). As the shape of the ligand is held in place by the aromatic sp^2 carbons, removal of guests would preclude framework collapse, rendering a permanently porous material.

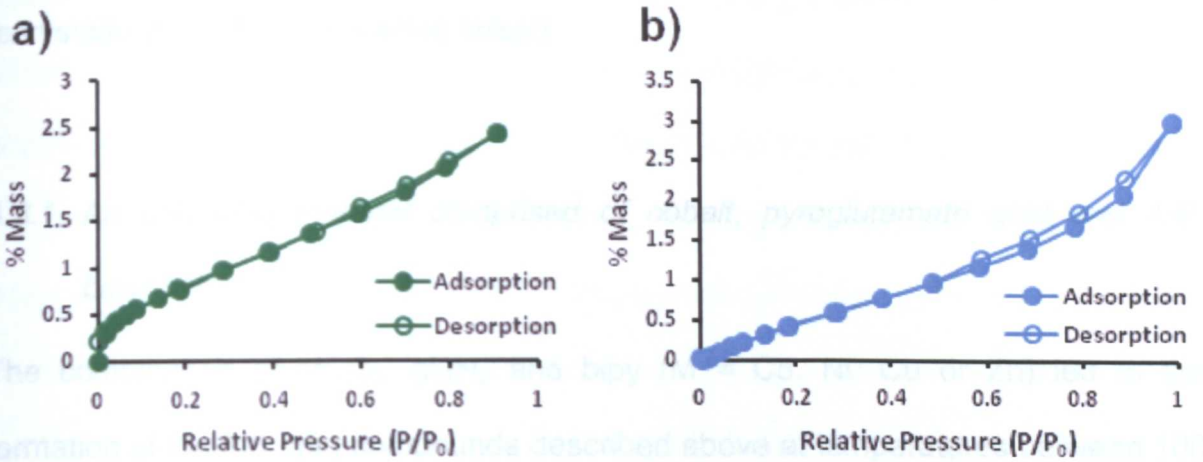

Figure 4.5. N_2 isotherms of a) Ni(L-glu)(H_2O)]•H_2O and b) Zn(L-glu)(H_2O)]•H_2O measured to 1 bar at 77K.

4.3 Coordination polymers based upon L-glutamic acid and 4,4'-bipyridyl

In order to synthesise a glutamic acid based material that displays permanent porosity, we investigated the reactivity of divalent metals with L-gluH_2 and bipy. Initial work focused upon solvothermal synthesis, using metal carbonates, L-glu and bipy in one-pot reactions. The carbonate salts were used as reaction with acids produces CO_2, reducing the amount of competing species within the reaction mixture, which we hoped would aid the formation of the desired material. H_2O was found to be an essential component of the reaction; the absence of H_2O lead to the recrystallisation of unreacted L-gluH_2, additionally alcoholic solvent, ROH was required for dissolution of bipy (again, absence of this solvent leads to recrystallisation of the unreacted linker).

4.3.1 An extended material comprised of cobalt, pyroglutamate acid and 4,4'-bipyridyl

The combination of MCO_3, gluH_2 and bipy (M = Co, Ni, Cu or Zn) led to the formation of the M(L-glu) compounds described above at temperatures between 100 and 120 °C. Reactions above this temperature range produced amorphous material, (M = Ni and Zn), or metal-oxide formation (M = Cu). However, the solvothermal reaction of $CoCO_3$ with glu and bipy in H_2O/MeOH at 150 °C yields orange crystals, which single crystal X-ray diffraction has determined to be $[Co(pyroglu)_2(bipy)(H_2O)_2]\cdot H_2O$, where pyroglu is deprotonated pyroglutamic acid (pyrogluH), the product of an *in-situ* internal cyclisation of gluH_2, (Figure 4.6).

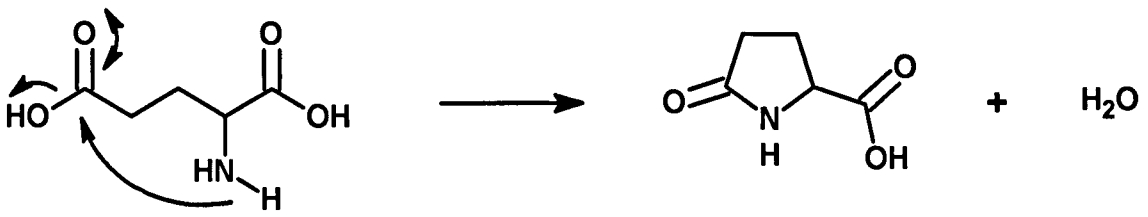

glutamic acid ($gluH_2$)

pyroglutamic acid (pyrogluH)

Figure 4.6. The internal cyclisation reaction of $gluH_2$, which yields pyroglutamic acid (pyrogluH).

This *in-situ* internal cyclisation reaction has been noted in the literature previously, in the combination of $MnCl_2$[22] or ZnO[23] with $gluH_2$. In each case, the chirality of the ligand is preserved during the cyclisation, with L-$gluH_2$ yielding L-pyrogluH. Within the Mn derived compound, $[Mn(L\text{-pyroglu})_2]$, L-pyroglu acts as a tridentate ligand, coordinating to three separate octahedral Mn(II) ions through the oxygen atoms of the carboxylate and amide functionalities, forming an infinite 1D coordination polymer. The Zn derived compound, $[Zn(L\text{-pyroglu})_2(H_2O)_2]$, exists as an isolated complex, with the L-pyroglu ligand coordinating in a monodentate fashion to a tetrahedral Zn(II) via the deprotonated carboxylate functionality (Figure 4.7 a and b). The Zn system has been isolated as both a homochiral, and a racemic mixture, depending upon the chiral purity of the starting materials, and can be synthesised using $gluH_2$[23] via the *in-situ* dimerisation of $gluH_2$ described above, or using pyrogluH directly as a starting material.[24,25] However, within $Co(pyroglu)_2(bipy)(H_2O)_2$ the two pyroglu moieties exist as opposite enantiomers despite the use of homochiral starting materials. This indicates that racemisation occurs during solvothermal synthesis, a feature we noted previously when using amino acids in solvothermal synthesis.[26]

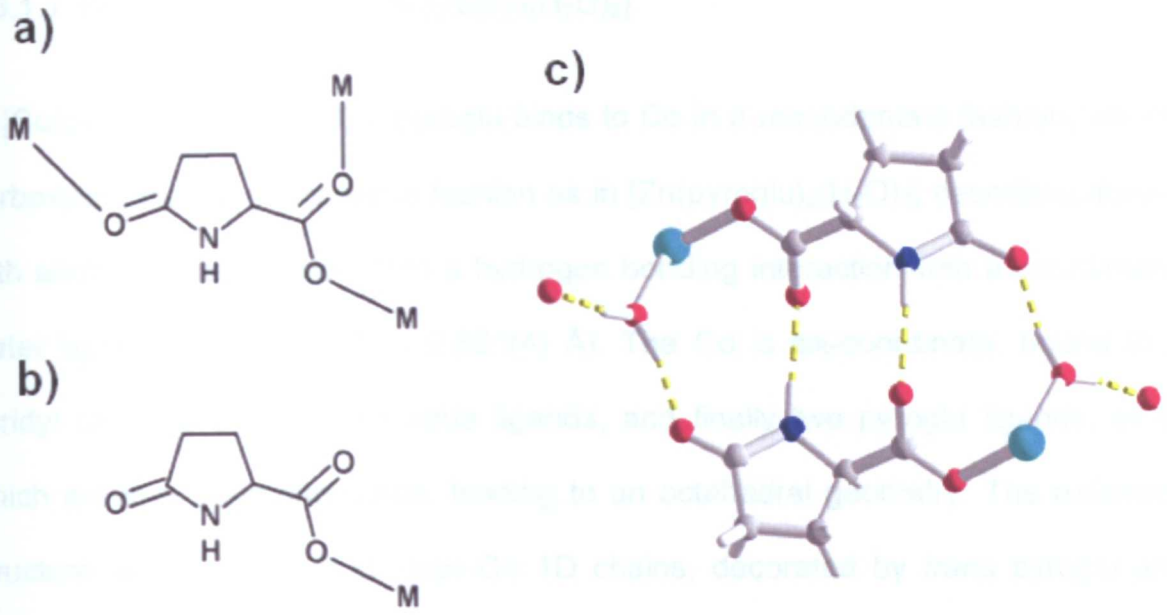

Figure 4.7. The coordination of pyroglu in a) $[Mn(pyroglu)_2]$[22] and b) $[Zn(pyroglu)_2(H_2O)_2]$.[23-25] c) The hydrogen bonding interactions within $[Zn(pyroglu)_2(H_2O)_2]$, denoted by broken yellow lines, which form a 2D supramolecular architecture. Zn is cyan, oxygen is red, nitrogen is blue and carbon is grey. Hydrogen atoms are white

The Zn based compound also displays significant supramolecular interactions between the complexes, arising from hydrogen bonding between the hydrogen atoms of the Zn-coordinated water molecules and the C=O oxygen atoms of the carboxylate and the amide of pyroglu. An additional interaction can be noted between the hydrogen from the amide N-H, and the oxygen from the C=O carboxylate group, leading to a 2D supramolecular architecture (Figure 4.7 c). Similar interactions are not noted within the Mn compound due to the bonding of all the available pyroglu oxygen atoms to Mn.

4.3.1.1 Structure of $[Co(pyroglu)_2(bipy)(H_2O)_2]$

In $[Co(pyroglu)_2(bipy)(H_2O)_2]$, pyroglu binds to Co in a monodentate fashion, via the carboxylate moiety in the same fashion as in $[Zn(pyroglu)_2(H_2O)_2]$ described above, with additional stabilisation from a hydrogen bonding interaction with a coordinated water ligand (C1=O3···O1W = 2.651(4) Å). The Co is six-coordinate, bound to 2 pyridyl moieties of bipy, two aqua ligands, and finally two pyroglu ligands, all of which are in a *trans* orientation, leading to an octahedral geometry. The extended structure is comprised of Co-bipy-Co 1D chains, decorated by *trans* pyroglu and H_2O ligands (Figure 4.8). Pyroglu is coordinated to Co via monodentate carboxylate bonding, leaving the amide N-H and O functionalities free.

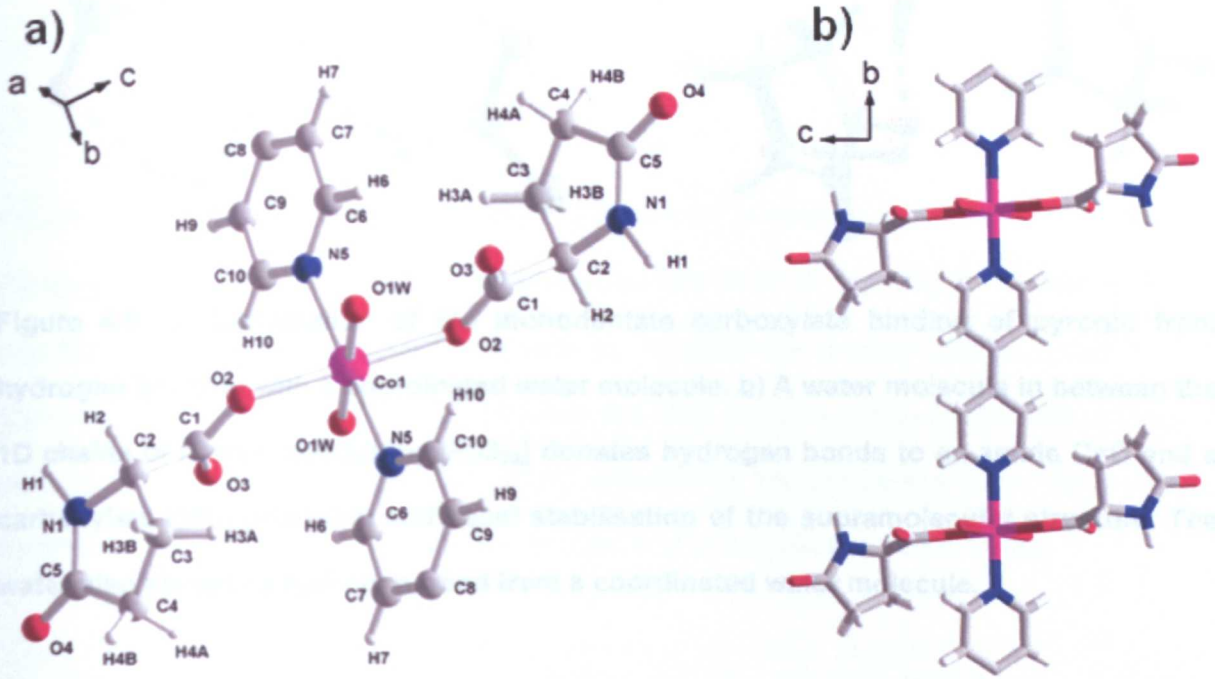

Figure 4.8. a) The coordination sphere of Co within $[Co(pyroglu)_2(bipy)(H_2O)_2]$, and b) the 1D coordination polymer formed by bipy along the *b*-axis. Co is purple, oxygen is red, nitrogen is blue, carbon is grey and hydrogen atoms are white. Hydrogen atoms from coordinated water are removed for clarity

4.3.1.2 Hydrogen bonding interactions within $[Co(pyroglu)_2(bipy)(H_2O)_2]$

As noted previously, the coordinated water molecules hydrogen bond to the C=O oxygen, stabilising the monodentate coordination of pyroglu. The presence of a water molecule in between the 1D chains of Co-bipy-Co also gives additional stability to the structure, donating two hydrogen bonds, to two distinct pyroglu moieties (O···O=C (amide) = 2.737(3), O-H···O=C (carboxylate) = 2.816(3) Å), and accepting a hydrogen bond from a coordinate water molecule. (O-H···O-H = 2.612(3) Å) (Figure 4.9).

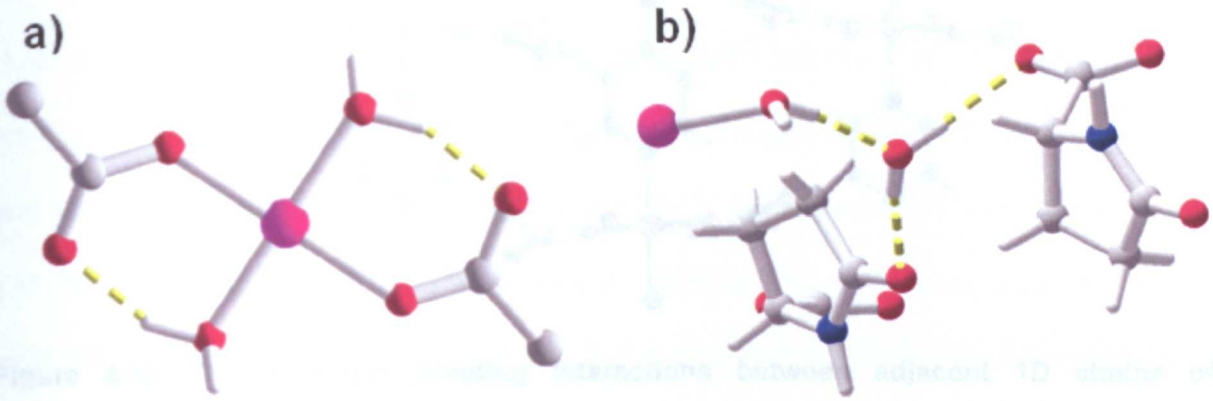

Figure 4.9. a) Stabilisation of the monodentate carboxylate binding of pyroglu from hydrogen bonding with a coordinated water molecule. b) A water molecule in between the 1D chains of $[Co(pyroglu)_2(bipy)(H_2O)_2]$ donates hydrogen bonds to an amide C=O and a carboxylate C=O, providing additional stabilisation of the supramolecular structure. The water also accepts a hydrogen bond from a coordinated water molecule.

The structure is held together in the second and third dimensions by strong hydrogen bonds arising from complementary N-H···O interactions between two adjacent pyroglu moieties along the *c*-axis, the hydrogen atoms of bipy, and the non-coordinated oxygen atom of pyroglu carboxylate along the *a*-axis (Figure 4.10).

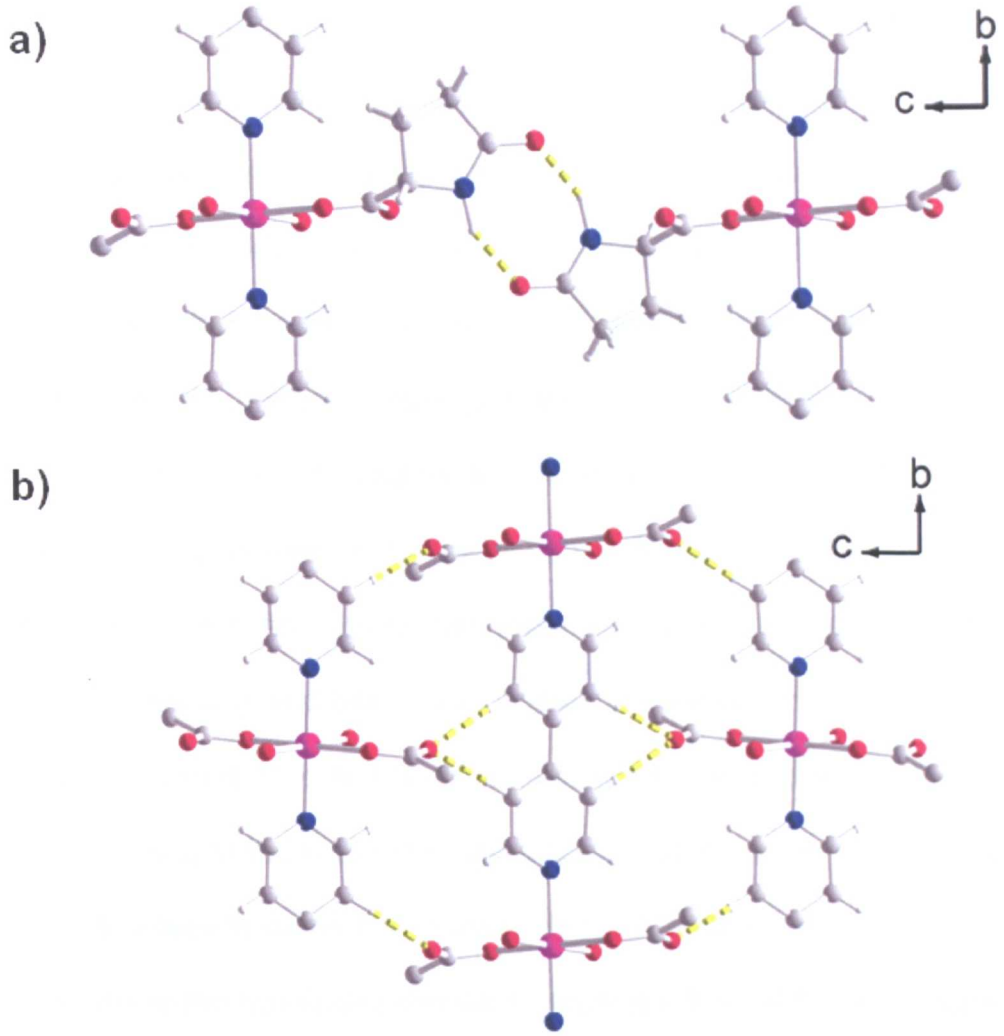

Figure 4.10. The hydrogen bonding interactions between adjacent 1D chains of $[Co(pyroglu)_2(bipy)(H_2O)_2]$. a) The complementary N-H···O hydrogen bonds between adjacent amide groups along the *c*-axis in, denoted by broken yellow lines. b) The aromatic C-H···O hydrogen bonds between the C=O oxygen of the carboxylate group of pyroglu and adjacent bipy moieties, again denoted by broken yellow lines. Co is purple, oxygen is red, nitrogen is blue, carbon is grey and hydrogen atoms are white

The 3D architecture of the structure is best understood by dissecting into two distinct 2D layers comprised solely of one of the hydrogen bonding connections and the covalent connections. First we consider the 2D layer comprised of the 1D bipy chains and the complementary N-H···O hydrogen bonds. The bipy binding forms a 1D chain along *b*. These chains are linked together by hydrogen bonding between

two adjacent pyroglu moieties along *c*, and are rotated by 180° with respect to each other, in order to maximise the directionality, and the strength of the hydrogen bonds. These two bonding interactions (covalent and hydrogen bonding) lead to a square grid-like layer, taking the nodes as the cobalt atoms (Figure 4.11 a and b). The second layer is formed from the bipy Co alternating chains, linking together by H-bonds between the uncoordinated oxygen of the carboxylate group and two hydrogen atoms from bipy. The chains are offset by 5.73Å (½*b*), demonstrating that a node exists in the centre of the bipy molecule, as it gives two-dimensional directionality within the layer. The formed layer is a square grid, and despite the fact there are two nodes (Co and bipy), they impart the same connectivity, making the layer uninodal (Figure 4.11 c and d). The two layers intersect at an angle of 29.9° via the nodes relating to the Co atoms, forming a 4-,6-connected binodal net. The 6-connected node arises from the Co connectivity; in both layers it is 4-connected, and it is the point where the two layers intersect, yielding a total of 6 connections. The 4-connected node is situated in the centre of the bipy ligand, arising from the aromatic C-H···O hydrogen bonding interactions with the carboxylate group of pyroglu. The resulting topology was determined using TOPOS 4.0,[27] and is designated the symbol **fsc** by the RCSR,[28] of which there are currently 33 examples in the literature (Figure 4.12). The 3D structure is dense, and upon removal of the water molecules by modifying the shelx file, contains 65 $Å^3$ solvent accessible volume (equivalent to 5.5% of the total cell) as determined using the SQUEEZE routine within PLATON.[21]

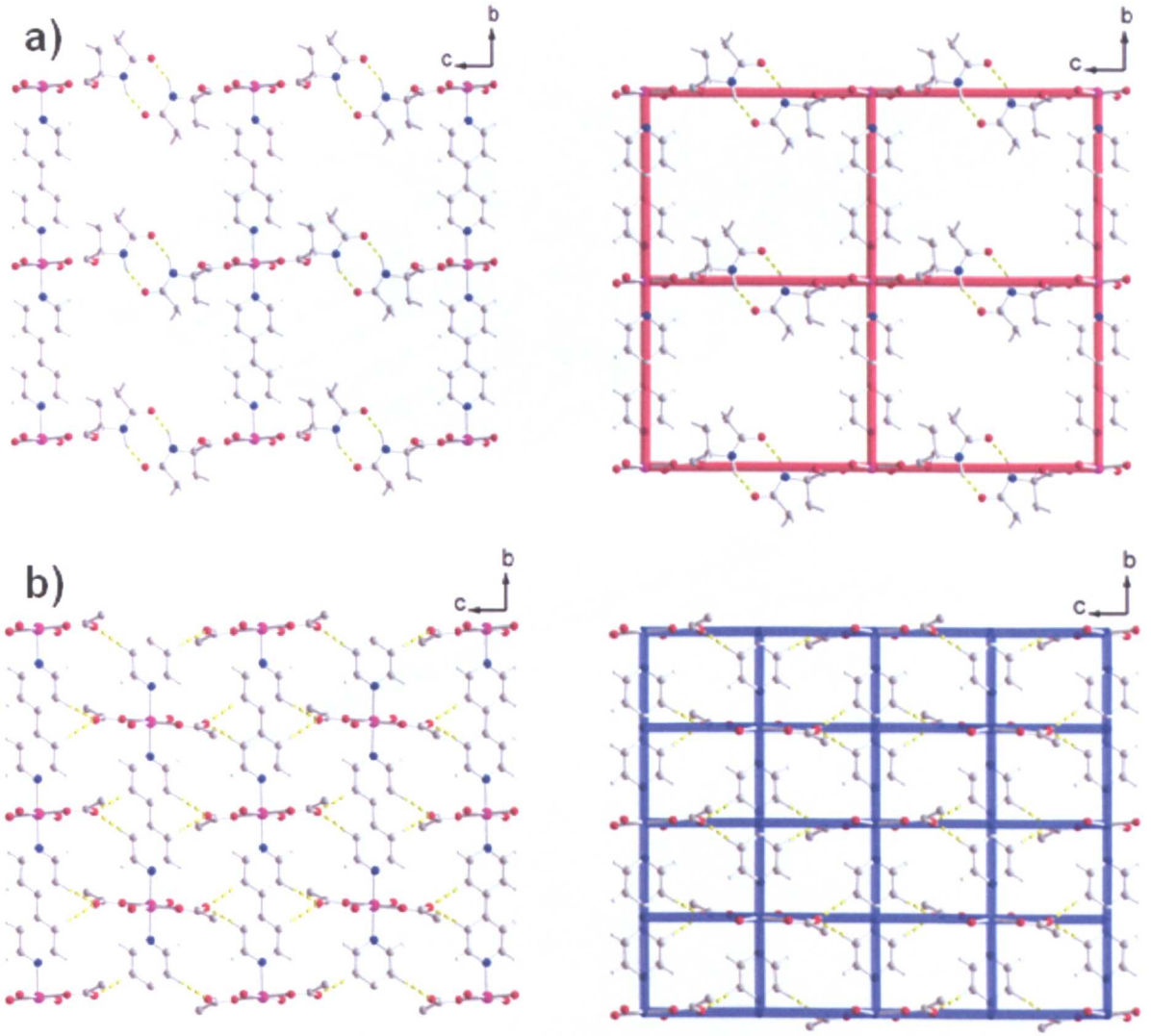

Figure 4.11. a) The 2D layer comprised of the infinite 1D Co-bipy chains and the complementary N-H···O hydrogen bonds, and b) the square 4^4 topology of the layer, where the Co atoms correspond to nodes. c) The 2D layer comprised of the infinite 1D Co-bipy chains and the C=O··H hydrogen bonding between the carboxylate of the L-pyroglu ligand and two aromatic C-H hydrogen atoms, and d) the 4^4 topology of the layer, where the Co atoms and the centre of the bipy ligands are nodes.

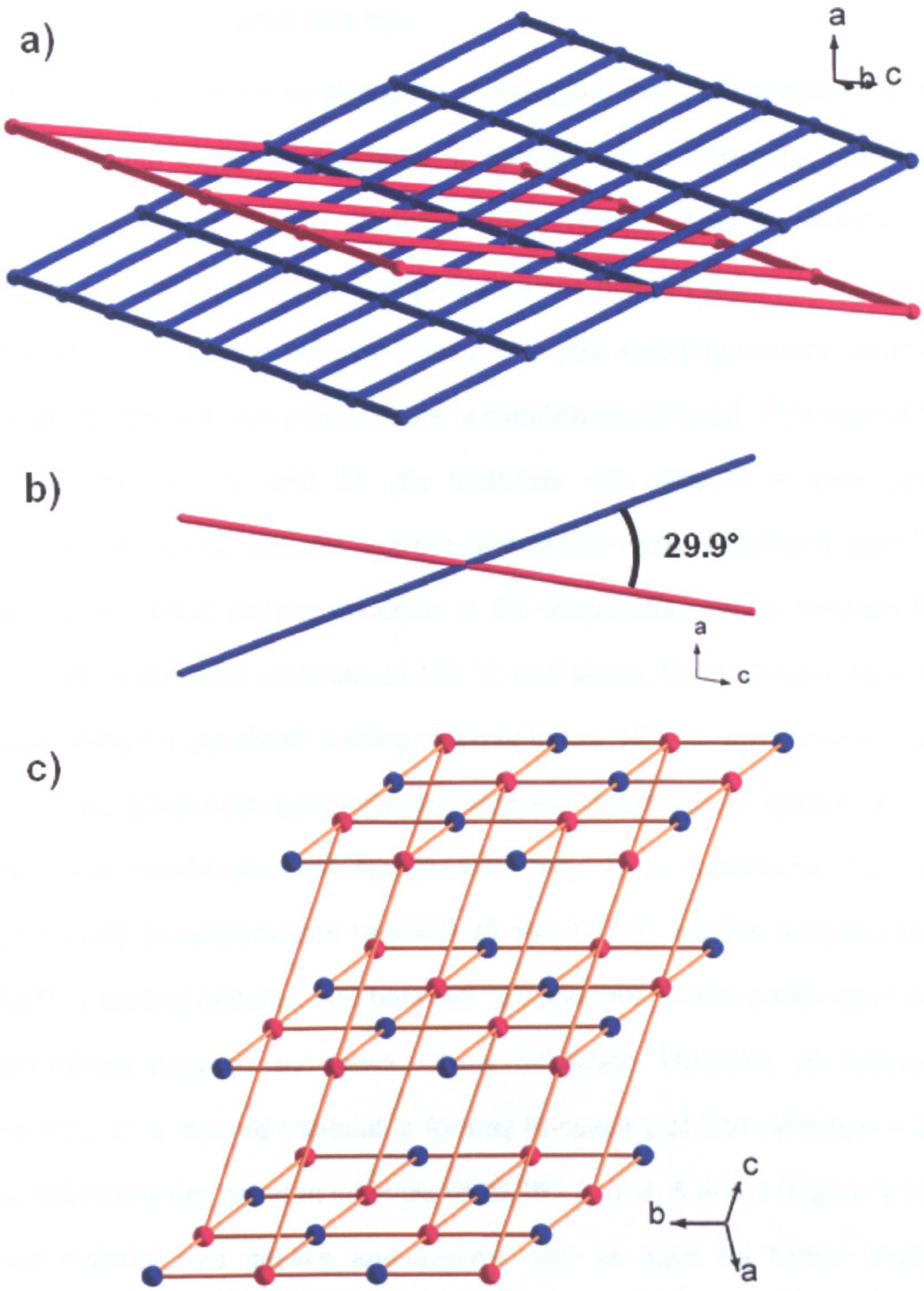

Figure 4.12. a) The intersecting layers of Co-bipy/N-H···O (red) and Co-bipy/C=O···H (blue), b) The angle between the two layers, which is equal to 29.9°, and c) The fsc toplogy of the formed 3D net. Red atoms correspond to the 6-connected nodes from the Co-bipy/N-H···O layer and blue atoms correspond to 4-connected nodes Co-bipy/C=O···H layer.

4.3.2 Reactions of M(L-glu) with bipy

An alternative approach to synthesise a mixed-ligand metal-glu based material is to use the M(L-glu) materials described in section 4.2 as a starting material, and directly combine with bipy in a solvothermal reactor. The advantages of this approach are that there are no competing anions present within the reaction, the number of components is reduced from 3 to 2 (not including solvent parameters), and therefore the reaction phase space is significantly reduced. This approach was used with the Co, Ni and Zn glu materials with bipy in a wide range of stoichiometries, concentrations, solvent and temperature. Reactions with Zn(glu) yielded recrystallised starting materials in the temperature range between 80 and 120 °C, and amorphous materials at 130 °C and above. Using Co(glu) as a starting material yields recrystallised starting material below 150 °C, and between 150 and 160 °C, the $[Co(pyroglu)_2(bipy)(H_2O)_2]$ material described in section 4.3.1 was formed. The combination of Ni(glu) with bipy in a water/butan-1-ol mixture solvothermally at temperatures between 80 and 110 °C, causes recrystallisation of the Ni(Glu) starting material, and between 120 and 140 °C, the combination only led to amorphous products by powder X-ray diffraction. However, at temperatures above 150 °C, a layered material is formed (d-spacing of first reflection = 20.5Å). Other reflections are noted at intervals of 20.45 / 2, 3, 4, 5 and 7 (Figure 4.13). The formed material was gel-like and impure, and as such no further analysis is presented.

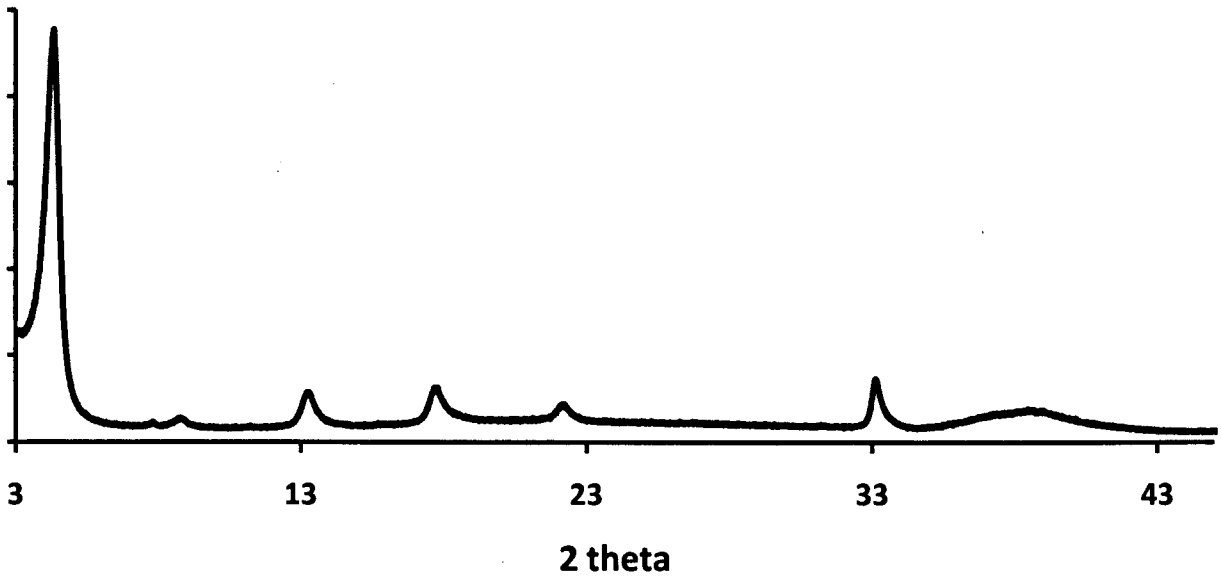

Figure 4.13. The powder X-ray diffraction pattern of the product of the solvothermal reaction of Ni(glu) + bipy at 150 °C in H_2O/Butan-1-ol.

4.3.2.1 The reactivity of $NiCO_3$ with glutamic acid

In order to fully understand the reactivity of the metal glutamates with bipy, we studied the effect of combining the starting materials at ambient pressure. The reflux reaction of L-gluH_2 with $NiCO_3$ leads to the formation of two products, depending upon the solvent used in the synthesis. If the solvent used is a H_2O/MeOH mixture, crystalline [Ni(L-glu)(H_2O)]•H_2O is precipitated. However, when the solvent is H_2O, the result is a green solution, which upon slow evaporation leads to a glassy green, free flowing solid that is amorphous by PXRD. Elemental analysis reveals the composition of the material to be Ni(L-glu)(H_2O)$_3$, indicating that the solid contains L-glu. UV-Vis and IR spectroscopy was performed on the two materials and the results were compared to elucidate the difference in structure of two Ni(L-glu) compounds. The UV-Vis spectrum of crystalline [Ni(L-glu)(H_2O)]•H_2O shows three bands, the first and second are in the UV range, with λ_{max} = 221 and 399 nm, corresponding to the

$^3T_{1g}(P) \leftarrow {}^3A_{2g}$ and the $^3T_{1g}(F) \leftarrow {}^3A_{2g}$ transitions respectively. The third is in the visible range, with λ_{max} = 683 nm, corresponding to the $^3T_{2g} \leftarrow {}^3A_{2g}$ transition. Within the UV-Vis spectrum of amorphous Ni(L-glu)$(H_2O)_3$, the ligand field bands maxima are shifted in energy, with the UV bands of $^3T_{1g}(P) \leftarrow {}^3A_{2g}$ and $^3T_{1g}(F) \leftarrow {}^3A_{2g}$ transitions shifting to λ_{max} = 210 and 391 nm respectively, and the visible $^3T_{1g}(F) \leftarrow {}^3A_{2g}$ transition shifting to λ_{max} = 656 nm (Figure 4.14).

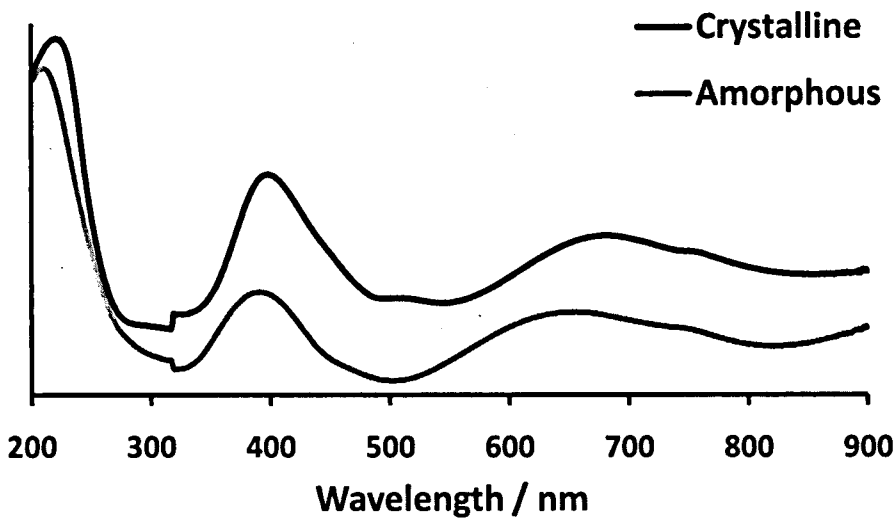

Figure 4.14. The UV-Vis spectra of crystalline [Ni(L-glu)(H_2O)]•H_2O (top) and amorphous Ni(L-glu)$(H_2O)_3$ (bottom).

This data indicates that there is only a minor difference in the coordination environment of the two compounds, and that L-glu is coordinated to Ni in both.

4.3.3 An extended material comprised of nickel, glutamic acid and 4,4'-bipyridyl

As an alternative starting material, amorphous Ni(L-glu)$(H_2O)_3$, was dissolved in H_2O at concentrations between 0.1 and 0.5 mol L^{-1}, and reacted solvothermally with bipy. However, the use of this alternative starting material led to complications, as solvothermal reaction in H_2O yields recrystallised bipy in reactions up to 130 °C, and amorphous materials in reactions above that temperature. We then proceeded to investigate the addition of other solvents, which cause bipy dissolution into the reaction mixture. At ambient temperature and pressure, the addition of the following miscible solvents all lead to the precipitation of a green solid, which PXRD determined to be [Ni(L-glu)(H_2O)]•H_2O; ethanol, methanol, dimethylformamide, dioxane and acetone. If immiscible solvents are added to an aqueous Ni(L-glu) solution, such as DCM, toluene, or hexane, the solutions separate and no precipitation is observed. Addition of bipy to the immiscible solvents prior to mixing with aqueous Ni(L-glu) solution, also shows the same result, with no mixing observed. Biphasic solvothermal synthesis[29] using the immiscible solvent mixtures described above was attempted, however all reactions between 100 and 150 °C led to the formation of amorphous products. Similarly, reactions with the miscible solvents at temperatures between 100 and 150 °C also led to the formation of amorphous products. In order to get a successful reaction to occur, it was decided that the precipitation of the amorphous solid upon addition of alcoholic solvents needed to be avoided (we focussed initially on alcoholic solvents as the [M_2(asp)$_2$(bipy)] family of materials is formed in a H_2O/MeOH mixture).[26] Therefore the use of capping ligands to prevent the formation of [Ni(L-glu)(H_2O)]•H_2O material were explored. It was found that by adding one equivalent of pyridine (py) to the aqueous Ni(L-glu)$(H_2O)_3$ solution, the coordination of the nitrogen of py to Ni caused

the colour of the solution to change from green to blue, which is further exemplified by the UV-Vis solution spectra of Ni(glu) and Ni(glu)(py) (Figure 4.15).

In order to test whether the formed Ni(glu)(py) solution could be used in solvothermal synthesis without the initial precipitation of Ni(L-glu)(H_2O)]•H_2O, MeOH was added to a 0.25M solution of Ni(glu)(py), followed by addition of 1 equivalent of bipy. Upon addition of MeOH, no colour change was observed, and no precipitate was present by optical microscopy. Addition of bipy to this solution caused the bipy to dissolve, without any colour change apparent, indicating that there was no change in coordination sphere of Ni(II).

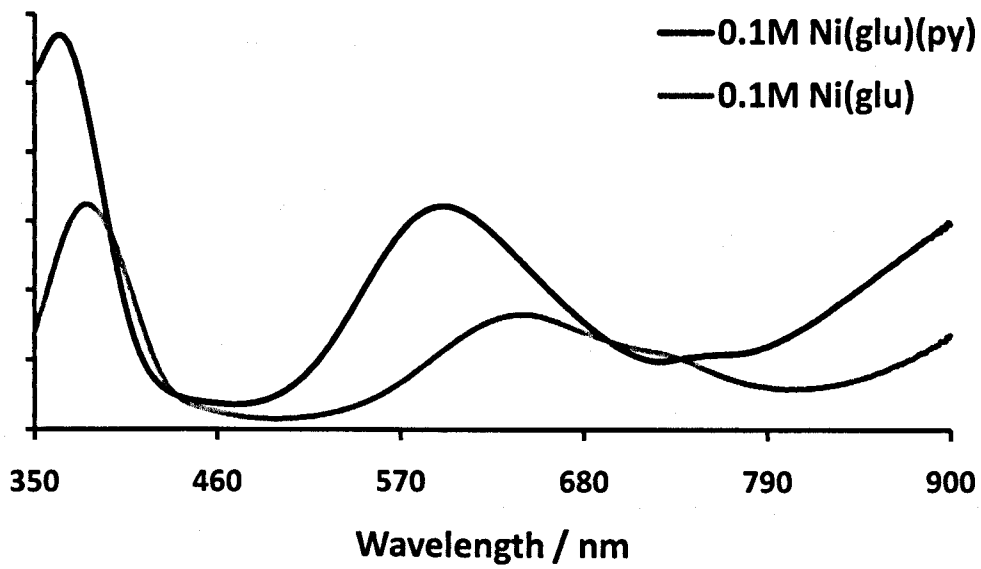

Figure 4.15. UV-Vis solution spectra of [Ni(glu)(py)] (top), and Ni(glu) (bottom).

4.3.3.1 Structure of [Ni(glu)(bipy)(H_2O)]

The solvothermal reaction of an aqueous solution of Ni(glu)(py) and bipy (molar ration = 2:1) in a H_2O/MeOH mixture (2/2ml respectively) at 100 °C leads to the formation of blue/green single crystals, of [Ni(L-glu)(bipy)(H_2O)], and an additional gel that could not be analysed using PXRD. [Ni(L-glu)(bipy)(H_2O)] crystallises in the monoclinic spacegroup $P2_1$, with the following crystallographic parameters; a = 9.2879(12) Å, b = 18.8495(23) Å, c = 11.3502(14) Å, β = 90.899(2) °, and V = 1986.87(73) Å^3. The structure was solved at Station 9.8 MX at the Darebury Synchrotron radiation source from a non-merohedral twinned crystal by Dr. Tim Prior. Refinement showed [Ni(L-glu)(bipy)(H_2O)] crystallises with a low Flack parameter 0.049(13), demonstrating that only one enantiomer of glu is present within the structure. The final structure is comprised of 1-dimensional chains of Ni(L-glu) linked together with bipy to form a 2-dimensional net, which has H_2O intercalated between the layers.

Within [Ni(L-glu)(bipy)(H_2O)], L- glu binds to Ni via two distinct coordination modes; i) through the ubiquitous bidentate 5-membered N-O chelation noted within amino acid coordination compounds, and ii) where the second oxygen atom of the carboxylate group involved in the chelation to Ni, bridges to a second metal ion, leading to the formation of an infinite one-dimensional chain of Ni(glu). The carboxylic acid side chain of glu is not involved in coordination to Ni(II), and is held in the solid state in two configurations; one where the carboxylate is involved in intramolecular hydrogen bonding the amine group (N21···O23 = 2.877(2) Å), and the second, where the carboxylate is pointing away from the amino group (Figure 4.16).

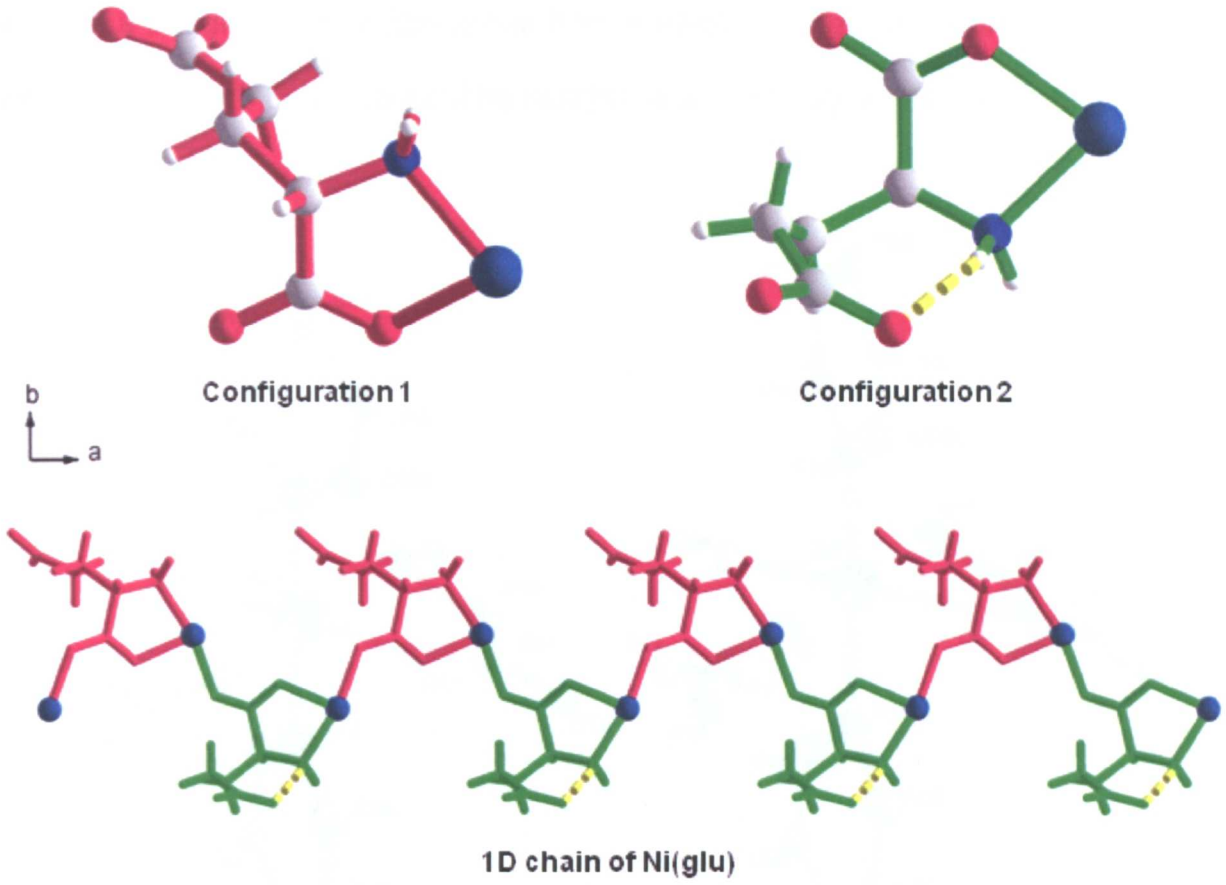

Figure 4.16. The structures of configuration 1 (red, top left) and configuration 2 (green, top right). The two configurations are rotated by 180° with respect to each other and propagate along the *a*-axis as a 1D chain (bottom) nickel is dark blue, hydrogen bonds are noted by a dashed yellow line. Ligands other than glu coordinated to Ni are excluded for clarity.

The existence of two crystallographically unique L-glu moieties within the structure of [Ni(L-glu)(bipy)(H_2O)] indicates that two unique Ni atoms must exist within the structure as each L-glu chelates one Ni ion, and the ratio of Ni:L-glu = 1:1. In addition, there must also be two inequivalent bipy molecules within the structure as again, one is bound per Ni. The two Ni centres within the structure both display identical coordination spheres, and are six-coordinate, bound to two L-glu ligands, two nitrogen atoms of bipy and finally by one molecule water. The equatorial sites of Ni are occupied by the N-O chelation of L-glu, the water molecule and an oxygen

atom of a bridging carboxylate group from a neighbouring L-glu moiety. Finally, the axial positions are both occupied by nitrogen atoms of bipy (Figure 4.17).

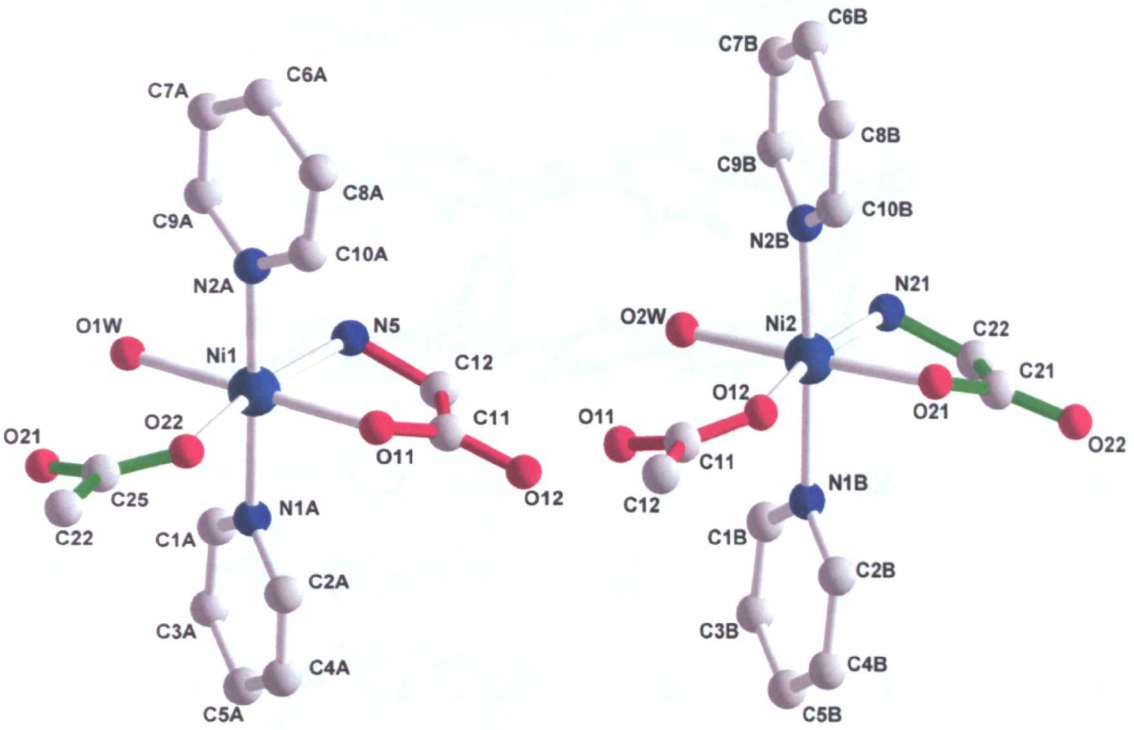

Figure 4.17. The coordination spheres of Ni1 (left) and Ni2 (right). Conformers 1 and 2 of glu are highlighted by red and green bonds respectively. Hydrogen atoms are removed for clarity.

The axial bipy ligand coordination to Ni leads to the formation of infinite Ni-bipy-Ni chains along the *c* direction. Coupled with the bridging functionality of L-glu described earlier, increases the dimensionality of the material to a 2D layer. Assigning the topology by connecting the Ni atoms that are linked together by bridging from L-glu or bipy ligands yields a uninodal 4^4 grid designated the symbol **sql** within the RCSR[28] (Figure 4.18).

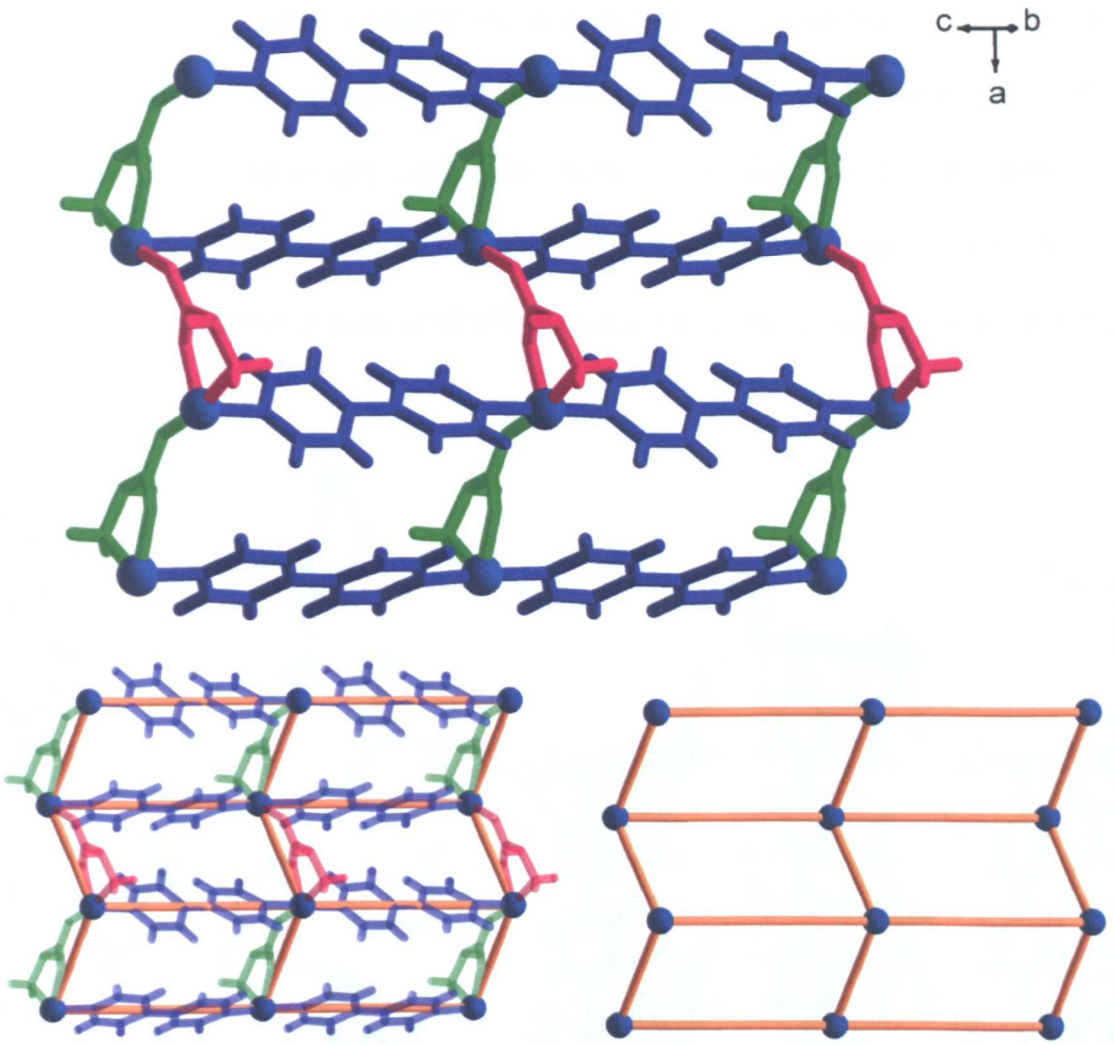

Figure 4.18. The two-dimensional layer of [Ni(L-glu)(bipy)(H_2O)]. Each Ni(L-glu) chain is pillared by bipy along the *c* direction (top). Connecting the Ni atoms, which are connected by either L-glu or bipy (bottom left) leads to the 4^4 square grid (bottom right). The vertices of the layer are orange, the two L-glu configurations, 1 and 2 are red and green respectively, bipy is blue, and Ni is dark blue. Coordinated water and the uncoordinated side chains of L-glu are removed for clarity.

The layers are held together in the third dimension by N-H···O hydrogen bonding between the side chain carboxylate of configuration 1 and the amine group of configuration 2 (Figure 4.19a). Configuration 1 also forms the internal NH···O hydrogen bond between the side chain carboxylate and the secondary amine described earlier, which adds rigidity to the structure. Configuration 2 does not

contain an internal hydrogen bond from its side chain, causing the carboxylate group to point into the space between the hydrogen bonded layers, ensuring efficient packing, and reducing empty space. In order to ensure the directionality of the NH···O hydrogen bonds between the two configurations, the layers are rotated by 180° with respect to the *b*-axis, and offset along the *c*-axis by 6.18Å (Figure 4.19).

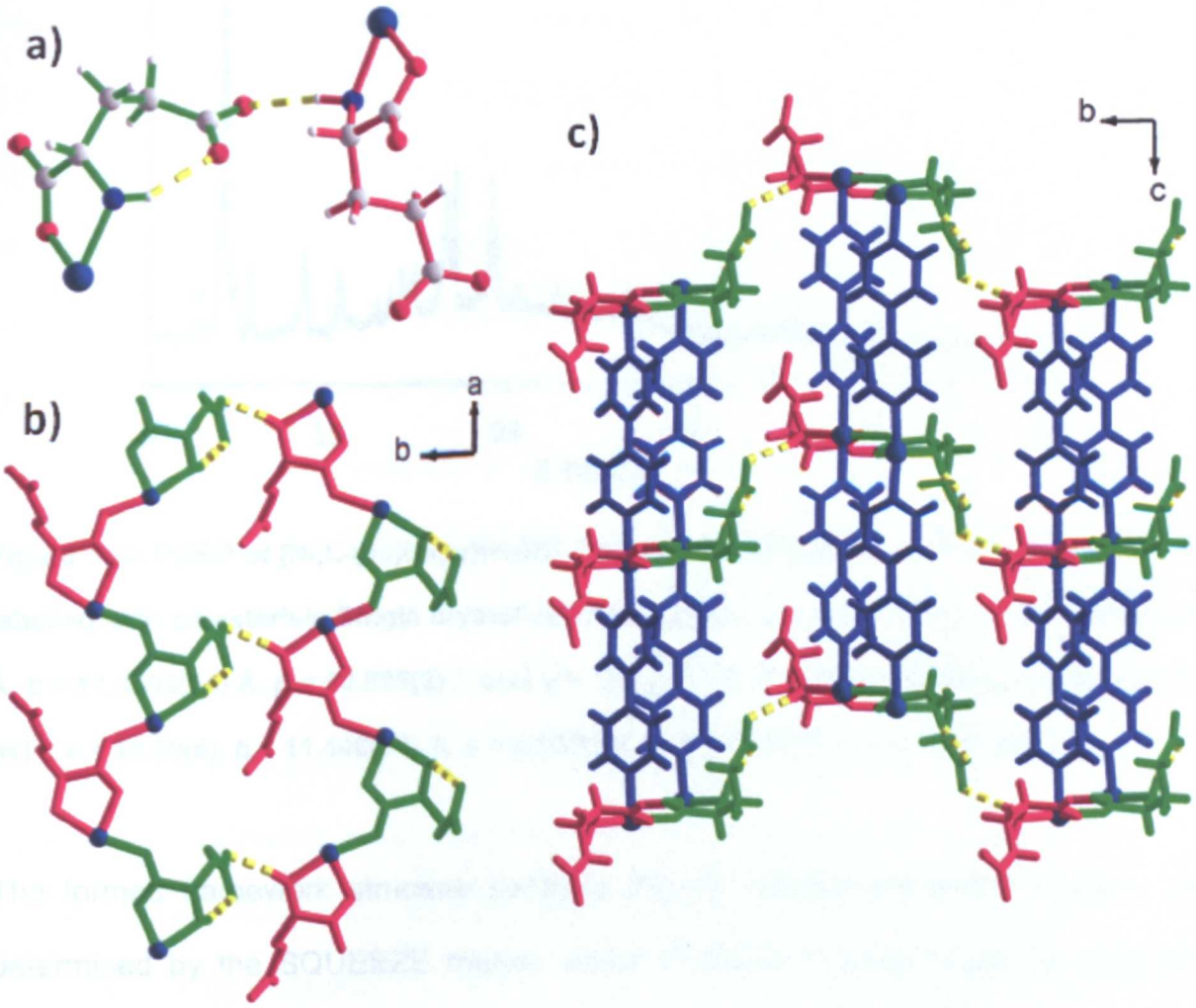

Figure 4.19. The build up of the 3D net through supramolecular bonding between the covalently bound layers. a) The hydrogen bonding interaction between two adjacent glu ligands from two separate layers. b) The interactions which hold the layers together along the *b*-axis. c) The hydrogen bonding directionality and packing of the layers lead to a 180° rotation about *b* and a displacement of 6.18Å along the *c*-axis. Glu configurations, 1 and 2 are red and green respectively, bipy is blue, and Ni is dark blue.

PXRD of the formed material indicates the presence of an impurity phase, with an unindexed peak at 2 theta = 7.702 °. The remaining 34 peaks in the diffraction pattern can be indexed to the monoclinic $P2_1$ cell; a = 18.08(5), b = 11.440(24) Å, c = 9.330(14) Å, β = 90.60(8) °, V = 1929(9) Å^3.

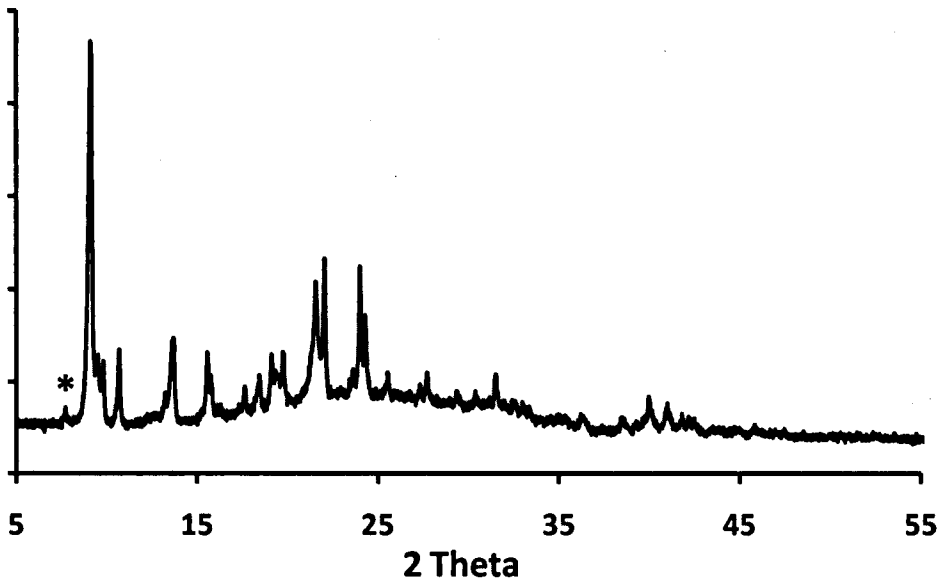

Figure 4.20. PXRD of [Ni(L-glu)(bipy)(H_2O)]. The one unindexed peak at 2theta = 7.702 °, is labelled with an asterisk. Single crystal cell parameters: a = 9.2879(12) Å, b = 18.8495(23) Å, c = 11.3502(14) Å, β = 90.899(2) °, and V = 1986.87(73) Å^3; PXRD refined cell parameters (RT): a = 18.08(5), b = 11.440(24) Å, c = 9.330(14) Å, β = 90.60(8) °, V = 1929.3(91) Å^3.

The formed framework structure contains 253 Å^3 solvent accessible volume, as determined by the SQUEEZE routine within PLATON,[21] which could be used for guest loading. However, due to the impurity phase, which could not be avoided within the synthesis of [Ni(L-glu)(bipy)(H_2O)], despite using different reaction times, temperatures, pH, and pyridine compounds within the reaction, the porosity studies could not be explored with this framework.

4.4 Conclusions

The structures of the transition metal-glu coordination compounds are dominated by the five-membered N-O metallocycle, and the bidentate CO_2^- chelation to M. Although the formed 3D structures contain channels which encapsulate water guest molecules, removal causes collapse of the structure and the resulting materials are non-porous. We aimed to circumvent this effect by forming a glu-bipy mixed ligand framework, and succeeded in forming the Co based framework, [Co-pyroglu)$_2$(bipy)(H_2O)$_2$] that contained pyroglu; the racemic product of an internal cyclisation reaction within L-glu. The framework displays 1D connectivity, and is held in the second and third dimensions by intermolecular hydrogen bonds from a complementary N-H···O interaction from the amide groups, and aromatic C-H···O=C between bipy and the carboxylate group of pyroglu. The formed framework contained 65 Å^3 solvent accessible volume, which is equivalent to 5.5% of the total unit cell. Through a detailed understanding of the reactivity of Ni with L-glu, we were able to isolate the Ni based framework, [Ni(L-glu)(bipy)(H_2O)], in which the carboxylate side-chain of L-glu is uncoordinated. This was achieved by using pyridine as a capping ligand, precluding formation of extended [Ni(L-glu)(H_2O)]•H_2O upon addition of MeOH, which was required in the reaction for bipy dissolution. The formed framework was 2D, held together in the third dimension by strong N-H···O hydrogen bonds between the layers, and contained 253 Å^3 solvent accessible volume. However a gel impurity within the product could not be avoided, despite a wide range of conditions attempted, and guest storage capabilities could not be further explored. The results of this chapter highlights the problems associated with introducing flexibility within MOFs, as the formed products can collapse upon desolvation, and the importance of understanding the chemistry of the starting

materials in solvothermal conditions, with regards to developing the reactivity. It was only through a detailed understanding of Ni(glu) chemistry, and the wide range of conditions used that allowed us to successfully isolate the described materials.

4.5 References

(1) Anokhina, E. V.; Go, Y. B.; Lee, Y.; Vogt, T.; Jacobson, A. J. *J. Am. Chem. Soc.* **2006**, *128*, 9957-9962.

(2) Anokhina, E. V.; Jacobson, A. J. *J. Am. Chem. Soc.* **2004**, *126*, 3044-3045.

(3) Antolini, L.; Menabue, L.; Pellacani, G. C.; Marcotrigiano, G. *Dalton Trans.* **1982**, 2541–2543.

(4) Doyne, T. H.; Pepinsky, R.; Watanabe, T. *Acta Cryst.* **1957**, *10*, 438-439.

(5) Kryger, L.; Rasmussen, S. E. *Acta Chem. Scand.* **1973**, *27*, 2674-2676.

(6) Schmidbaur, H.; Bach, I.; Riede, J.; Muller, G.; Helbig, J.; Hopf, G. *Chem. Ber.* **1988**, *121*, 795-797.

(7) Allen, F. H. *Acta Cryst.* **2002**, *B58*, 380-388.

(8) Antolini, L.; Marcotrigiano, G.; Menabue, L.; Pellacani, G. C.; Saladini, M.; Sola, M. *Inorg. Chem.* **1985**, *24*, 3621-3626.

(9) Flook, R. J.; Freeman, H. C.; Scudder, M. L. *Acta Crystallogr B* **1977**, *B33*, 801-809.

(10) Gramaccioli, C. M. *Acta Cryst.* **1966**, *21*, 600–605.

(11) Gramaccioli, C. M.; Marsh, R. E. *Acta Cryst.* **1966**, *21*, 594–600.

(12) Lu, T.; Li, X.; Mao, Z.; Qiu, W.; Ji, L.; Yu, K. *Polyhedron* **1998**, *17*, 75–79.

(13) Zhang, Y.; Saha, M. K.; Bernal, I. *CrystEngComm* **2003**, *5*, 34–37.

(14) Laurie, S. H. *Comprehensive Coordination Chemistry*; Pergamon: Oxford, 1987; Vol. 2.

(15) Dietzel, P. D. C.; Panella, B.; Hirscher, M.; Blom, R.; Fjellvåg, H. *Chem. Commun.* **2006**, 959-961.

(16) Dietzel, P. D. C.; Morita, Y.; Blom, R.; Fjellvåg, H. *Angew. Chem. Int. Ed.* **2005**, *44*, 6354-6358.

(17) Ball, R. J.; Genge, A. R. J.; Radford, A. L.; Skelton, B. W.; Tolhurst, V.-A.; White, A. H. *J. Chem. Soc., Dalton Trans.* **2001**, 2807-2812.

(18) Nielson, D. O.; Larsen, M. L.; Willett, R. D.; Legg, J. I. *J. Am. Chem. Soc.* **1971**, *93*, 5079-5082.

(19) Santana, M. D.; Garcia, G.; Rufete, A.; Sanchez, G.; Ramirez-de-Arellano, M. C.; Lopez, G. *Inorg. Chem. Commun.* **1998**, *1*, 267-269.

(20) Shim, C. B.; Kim, Y. H.; Lee, B. Y.; Dong, Y.; Yun, H. *Organometallics* **2003**, *22*, 4272–4280.

(21) Spek, A. L. *J. Appl. Cryst.* **2003**, *36*, 7-13.

(22) Gutschke, S. O. H.; Price, D. J.; Powell, A. K.; Wood, P. T. *Inorg. Chem.* **2000**, *39*, 3705-3707.

(23) Schmidbaur, H.; Bach, I.; Wilkinson, D. L.; Muller, G. *Chem. Ber.* **1988**, *121*, 1441–1444.

(24) Loireau-Lozach, A. M.; Ceolin, R.; Solans, X.; Font-Bardia, M. *Acta Cryst.* **1998**, *C54*, 1571-1573.

(25) Rodier, N.; Ceolin, R.; Plat, M.; Zumbihl, H. *Acta Cryst.* **1990**, *C46*, 324-326.

(26) Vaidhyanathan, R.; Bradshaw, D.; Rebilly, J.-N.; Barrio, J. P.; Gould, J. A.; Berry, N. G.; Rosseinsky, M. J. *Angew. Chem. Int. Ed.* **2006**, *45*, 6495 –6499.

(27) Polynova, T. N.; Chuklanova, E. B.; Porai-Koshits, M. A. *Dokl. Akad. Nauk* **1985**, *283*.

(28) Ockwig, N. W.; Delgado-Friedrichs, O.; O'Keefe, M.; Yaghi, O. M. *Acc. Chem. Res.* **2005**, *38*, 176–182, and the Reticular Chemistry Structure Resource website at http://rcsr.anu.edu.au.

(29) Forster, P. M.; Thomas, P. M.; Cheetham, A. K. *Chem. Mater.* **2002**, *14*, 17-20.

Chapter 5 The effect of high-pressure on a nickel aspartate framework

5.1 Introduction

The ability of metal-organic frameworks (MOFs) to respond to external stimuli is well documented, albeit from the introduction of guest molecules, changes in temperature, pressure, pH, or chemical transformations by combination with reactive species. All can have a pronounced effect upon the structure of the parent material and therefore an effect upon the inherent properties of the materials. We were interested in applying high-hydrostatic pressures on the crystal structures of amino-acid derived frameworks, as the flexible structure of these materials could be influenced greatly under pressure, potentially leading to new polymorphs, which cannot be accessed under normal synthetic conditions. To date, there have only been two studies of MOF single crystals at high pressure; $[Zn(C_3H_3N_2)_2]$ (ZnIm)[1], and $[ZnC_6H_6N_2)_2]$ (ZnMeIm, ZIF-8)[2], although recently a high-pressure study on two isostructural supramolecular metal-organic networks has been performed.[3] The two MOF studies were both performed on frameworks of the structural type, known as zeolitic imidazolate frameworks (ZIFs),[4,5] containing a single metal and an imidazolate moiety which demonstrates a similar connectivity to zeolites due to the metal-imidazolate-metal bond angle being similar to the Si-O-Si bond angle within zeolites (145°). These materials also have high thermal and chemical stability compared to most other MOFs, retaining their structure after heating to as high as 450 °C, or refluxing in dilute aqueous base. The study of ZnIm demonstrated that under the influence of hydrostatic pressure, ZnIm undergoes a phase transition at 0.8 GPa involving a cooperative bond rearrangement generating a previously

unknown phase (as-synthesised space group = $I4cd$, post-transformation = $I4_1$). The parent material (ZnIm-α) contains one-dimensional pores along the *c*-axis, which, after post-transformation to ZnIm-*β*, no longer exist due to the bond rearrangement minimising the volume of the unit cell (ZnIm-α, volume at ambient pressure = 6883.1(2) Å^3, ZnIm-*β*, volume at ambient pressure, post-compression = 6735.9(2) Å^3. The cooperative bond rearrangement also results in a change in the topology of the structure, with an edge (imidazolate) moving to link to a different vertex (Zn(II)) (Figure 5.1).

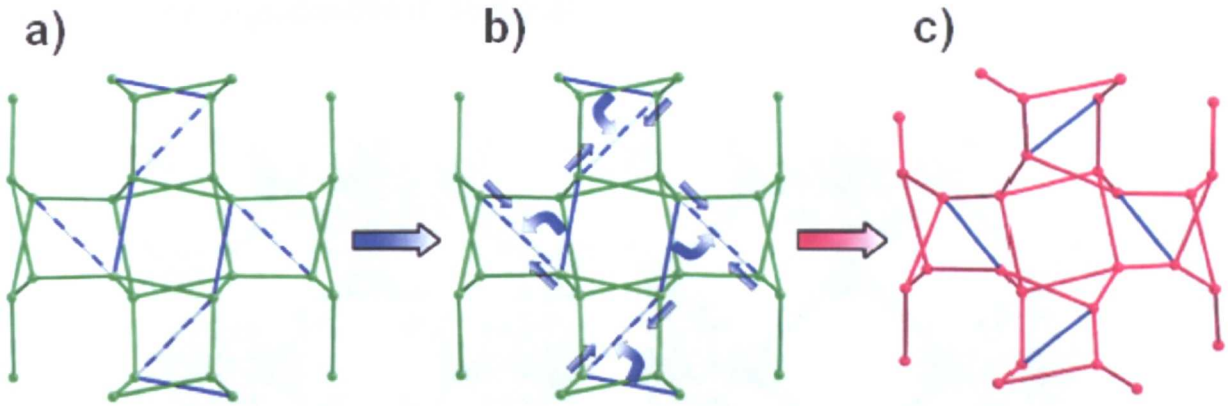

Figure 5.1. a) Ball-and-stick representation of the ZnIm α-phase; the Zn(II) cations are shown as balls and the imidazolate ions as sticks. The diagram also shows the cooperative bond rearrangement that occurs during the α→*β* phase transition. The solid blue lines are the links that are broken during the transition, and the blue and white stripped lines show the locations where the imidazolate links are reformed. (c) The ZnIm *β*-phase. The blue lines show the new positions for the imidazolate links that moved during the transition. Figure is reproduced from ref 1.

ZIF-8 crystallises in the cubic space group $I\bar{4}3m$, and contains a 3-dimensional pore network, with large central cavities with a volume of 2465 Å^3 linked by eight smaller channels. The material displays different behaviour under pressure compared to

ZnIm, with the initial application of pressure up to 0.18 GPa causing the volume of the unit cell to increase (from 4900.5(8) to 4999.6(2) $Å^3$) as the hydrostatic medium used is forced into the central cavities of the pore network. Further application of pressure results in decrease of the cell volume, until the pressure is increased to 1.47 GPa causing a phase change, as demonstrated by a second increase in cell volume (from 4893.5(2) to 4974.8(9) $Å^3$). The new phase, ZIF-8-II, maintains the same space group symmetry, and also the same topology (in contrast to the ZnIm study), with the change in phase occurring by a rotation in the methylimidazolate (MeIM) ligands between the Zn atoms, causing an increase in size of the channels, which link the large cavities (Figure 5.2).

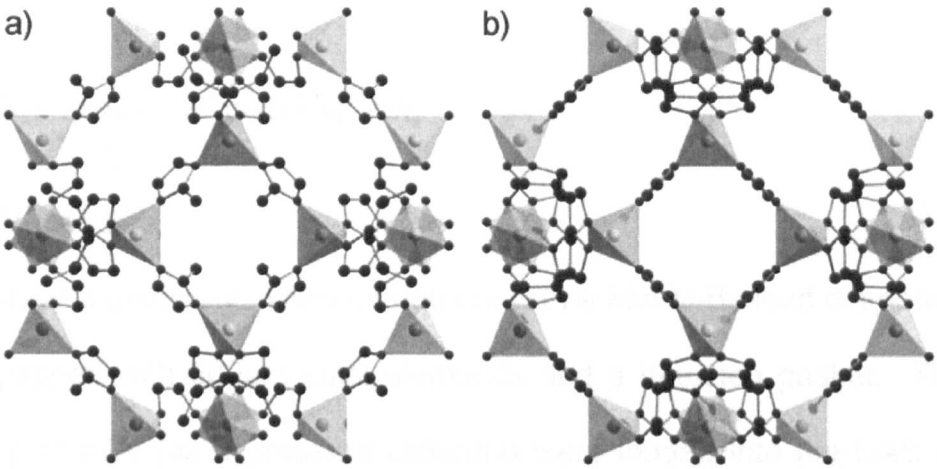

Figure 5.2. The structure of a) ZIF-8 at ambient pressure and b) ZIF-8-II at 1.47 GPa. ZnN_4 tetrahedra are drawn as rigid polyhedra. Hydrogen atoms are removed for clarity.

Here, we will discuss the effect of high pressure on the metal-aspartate coordination polymer [Ni(L-asp)$(H_2O)_2$], and its transition to a new high pressure phase ([Ni(L-asp)$(H_2O)_2$]-II).

5.2 The Effect of Pressure on the Crystal Structure of [Ni(L-asp)(H_2O)$_2$]-I to 8.8 GPa, and the structure of [Ni(L-asp)(H_2O)$_2$]-II at 1.26-6.07 GPa

5.2.1 Experimental

5.2.1.1 Synthesis

[Ni(L-asp)(H_2O)$_2$]•H_2O-I was synthesised by solvothermal synthesis of $NiCO_3$ (0.089g, 0.751mmol) and L-aspartic acid (0.100g, 0.751mmol) in a 1:1 water:methanol mixture (4ml) at 100 °C for 18h. This yielded green block-shaped crystals suitable for single crystal X-ray diffraction.

5.2.1.2 High-Pressure Crystallography

General Procedures

High-pressure experiments were carried out with a Merrill-Bassett diamond anvil cell (DAC) equipped with 600μm culet diamonds and a tungsten gasket. The sample and a chip of ruby (as a pressure calibrant) were loaded into the DAC with a 4:1 mixture of methanol and ethanol as a hydrostatic medium. The ruby fluorescence method was utilised to measure the pressure.[6]

Data Collection, Reduction and Refinement

A sphere of data was collected on a crystal of [Ni(L-asp)(H_2O)$_2$]•H_2O at ambient temperature and pressure in order to provide data for comparison with the high pressure studies, which were also performed at ambient temperature (see below). Diffraction data were collected on a single crystal of [Ni(L-asp)(H_2O)$_2$]•H_2O on a

Bruker APEX-II diffractometer with graphite-monochromated Mo Kα radiation (λ = 0.71073 Å). These data were integrated using the program SAINT,[7] while the absorption correction was carried out with the program SADABS.[8] Refinement was carried out against $|F|^2$ using all data[9] and the structure solved using SIR92[10] The final conventional *R*-factor was 0.019 for 3484 data. Listings of crystal and refinement data are given in Table 5.1.

Pressure/KPa	101.325 kPa
Phase	I
Radiation type	Mo *K*α
Chemical formula	$C_4H_9NNiO_6 \cdot H_2O$
M_r	243.84
Cell setting, space group	orthorhombic, $P2_12_12_1$
a, b, c/Å	12.2908(2), 8.9941(2), 7.6033(2)
V (Å^3)	840.50(3)
Z	4
D_0 (Mg m^{-3})	1.927
Measured, independent and observed reflections	15855, 3763, 3484
Criterion for observed reflections	$[I > 2.0\sigma(I)]$
R_{int}	0.019
Completeness	99.5% to $\theta = 31.2°$
$R[F^2 > 2\sigma(F^2)]$, $wR(F^2)$, S	0.016, 0.044, 1.05
No. of reflections	3763
No. of restraints	9
Parameters	137
$\Delta\rho_{max}$, $\Delta\rho_{min}$ /e Å^{-3}	0.40, -0.36
Absolute structure	Flack (1983), 1520 Friedel-pairs
Flack parameter	0.015(7)

Table 5.1. Crystal and refinement data for [Ni(L-asp)(H_2O)$_2$]•H_2O-I at ambient pressure.

High pressure diffraction data were collected with synchrotron radiation on a Bruker APEX II diffractometer at the CCLRC Daresbury Laboratory on Station 9.8 (λ = 0.4762 Å). Data were collected in ω-scans in 8 settings of 2θ and φ with a frame and step size of one second and 0.3°, respectively. The data were integrated using the program SAINT using 'dynamic masks' to avoid integration of regions of the detector shaded by the body of the pressure cell.[11] Absorption corrections for the

DAC and sample were carried out with the programs SHADE[12] and SADABS, respectively. Data were collected from 0.14 GPa up to a final pressure of 6.07 GPa, above which the sample became polycrystalline. On increasing pressure from 0.58 GPa to 1.26 GPa, the sample underwent a single-crystal to single-crystal phase transition.

Refinements of [Ni(L-Asp)(H_2O)$_2$]•H_2O-I (the ambient pressure phase) to 0.58 GPa were carried out starting from our room temperature re-determination of the structure. Refinements were carried out against $|F|^2$ using all data (CRYSTALS). Because of the low completeness of the high-pressure data-sets, all 1,2 and 1,3 distances on the aspartate ligand were restrained to the values observed in the ambient pressure structure, however all torsion angles and metal to ligand distances were refined freely. Thermal similarity restraints were also applied to the aspartate ligand. All hydrogen atoms attached to carbon and nitrogen were placed geometrically and not refined. The numbering scheme used is shown in Figure 5.3. Only the nickel atom was refined anisotropically, while all other non-hydrogen atoms were refined with isotropic thermal parameters. [Ni(L-Asp)(H_2O)$_2$]•H_2O-II at 1.26 GPa (the high-pressure phase), was solved using atomic coordinates from the room temperature re-determination of the structure, and refinements were carried out against $|F|^2$ using all data (CRYSTALS). All 1,2 and 1,3 distances on the aspartate ligand were restrained to the values observed in the ambient pressure structure, due to the low completeness of the high-pressure data-sets, as with the refinement of [Ni(L-Asp)(H_2O)$_2$]•H_2O-I high-pressure data. Again, all torsion angles and metal to ligand distances were refined freely. Thermal similarity restraints were also applied to the aspartate ligand. All hydrogen atoms attached to carbon and nitrogen were

placed geometrically and not refined. Listings of crystal and refinement data are given in Table 5.2.

Pressure/GPa	1.26
Phase	II
Radiation type	Synchrotron, $\lambda = 0.4769$ Å
Chemical formula	$C_4H_9NNiO_6 \cdot H_2O$
M_r	243.84
Cell setting, space group	orthorhombic, $P2_12_12_1$
a, b, c/ Å	11.2103(4), 9.1455(2), 7.7024(3)
V (Å^3)	789.68 (5)
Z	4
D_0 (Mg m^{-3})	2.051
Measured, independent and observed reflections	5532, 1551, 1283
Criterion for observed reflections	$[I > 2.0\sigma(I)]$
R_{int}	0.041
Completeness	66% to $\theta = 25.9°$
$R[F^2 > 2\sigma(F^2)]$, $wR(F^2)$, S	0.021, 0.060, 0.92
Reflections	1518
Restraints	27
Parameters	137
$\Delta\rho_{max}$, $\Delta\rho_{min}$ /e Å^{-3}	0.73, -0.78
Absolute structure	Flack (1983). 679 Friedel-pairs
Flack parameter	0.253(15)

Table 5.2. Crystal and refinement data for [Ni(L-asp)$(H_2O)_2$]•H_2O-II at 1.26GPa

Software for Structure Analysis

Crystal structures were visualized using the programs DIAMOND[13] and MERCURY[14]. Searches of the Cambridge Database[15,16] were performed with the program CONQUEST and version 5.29 of the database with updates up to January 2008.

5.2.2 *Ambient pressure crystal structure of [Ni(L-Asp)(H_2O)$_2$]•H_2O-I*

In [[Ni(L-Asp)(H_2O)$_2$]•H_2O-I,[17] Ni is 6-coordinate, bound to a single L-asp ligand and 2 water molecules. L-asp coordinates via the O-N-O tridentate chelation described in chapter 3, with a *syn-anti* bridging functionality arising from the C4 carboxylate that forms the 6-membered N-O metallacycle. The coordination sphere is completed by two water ligands, bound in a *cis* arrangement, leading to the complex in Figure 5.3. A single water molecule exists outside of the coordination sphere as a solvent of crystallisation.

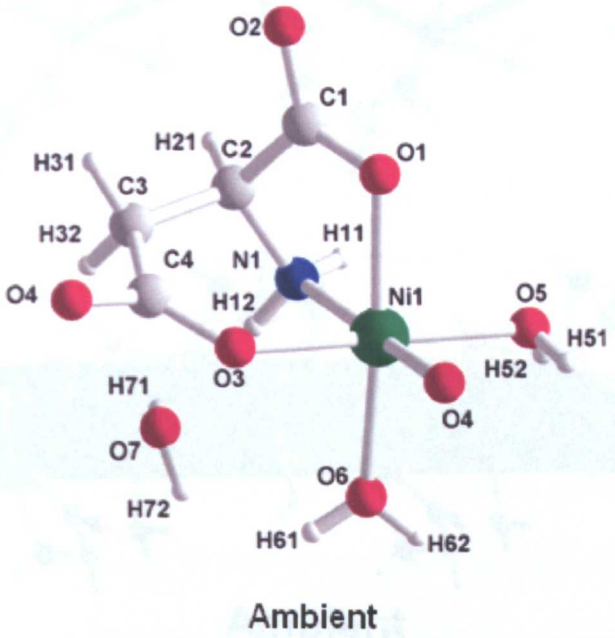

Figure 5.3. The coordination sphere of Ni in [Ni(L-Asp)(H_2O)$_2$]•H_2O-I at ambient pressure, and the solvent of crystallisation. Nickel is green, oxygen is red, nitrogen is blue, carbon is grey and hydrogen is white.

The *syn-anti* bridging from the C4 carboxylate results in a 1-dimensional coordination polymer. The bridging oxygen O4 is coordinated *trans* to the N1 nitrogen at the centre of the O-N-O chelation to Ni, and each Ni(L-asp) moiety is

rotated by 180°, resulting in a zigzag formation extending along the *b*-axis. The Ni-Ni-Ni bond angle is equal to 117.67(0)° (Figure 5.4a). Joining the Ni atoms along either side of the zigzag, the Ni(L-asp) moieties can be defined as a plane, which is further stabilised by three intermolecular hydrogen bonding interactions with the solvent of crystallisation water molecule (O7···O1 = 2.833(1) Å, O7···O4 = 2.954(1) Å, O6H62···O4 = 2.724(1) Å) (Figure 5.4b).

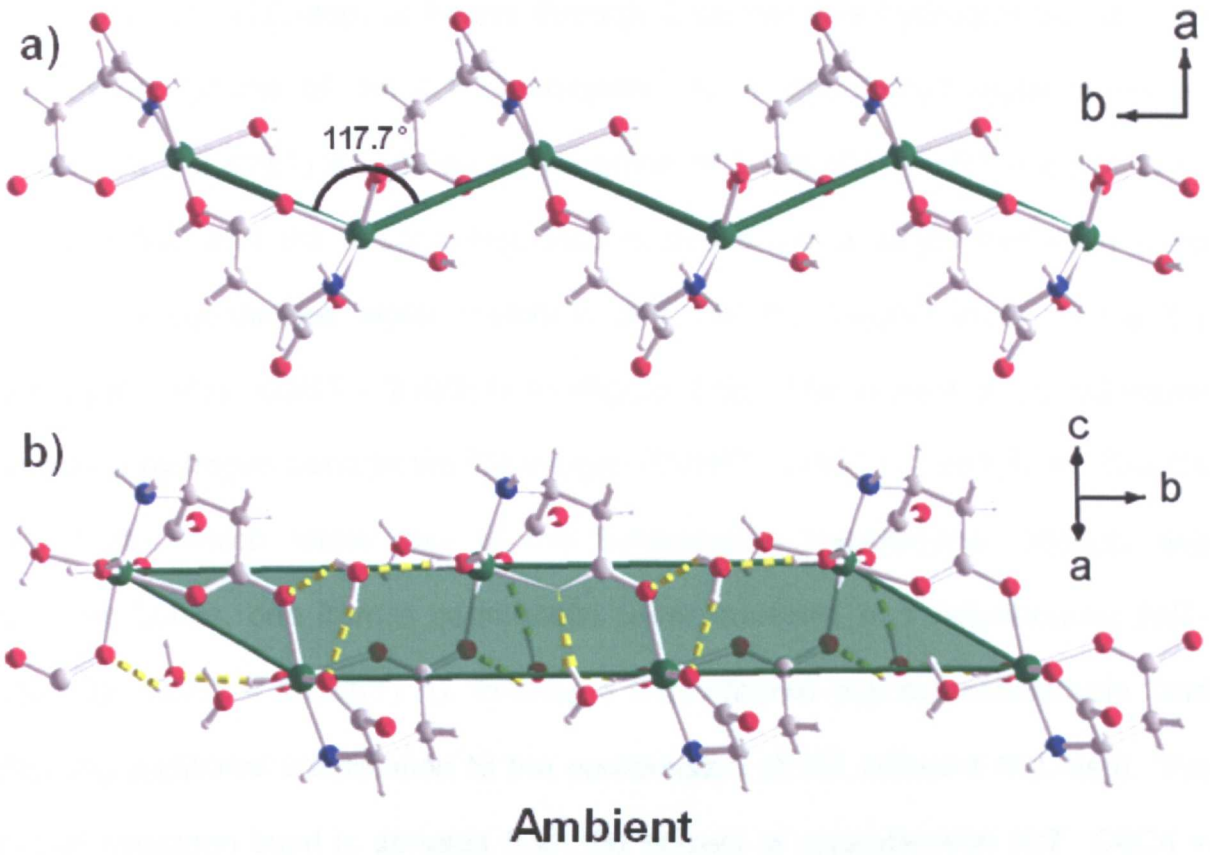

Figure 5.4. a) The extension of [Ni(L-Asp)(H_2O)$_2$]•H_2O-I along the *b*-axis at ambient pressure, note the zigzag shape. The green bonds signify the Ni atoms linked through L-asp coordination. b) The plane of Ni(L-asp) moieties which runs along the *b*-axis. Nickel is green, oxygen is red, nitrogen is blue, carbon is grey and hydrogen is white. Hydrogen bonds are denoted by a broken yellow line

The functional groups of L-asp also participate in additional hydrogen bonding interactions, which link the 1D chains in the second and third dimensions, and provide additional stabilisation to the structure, with each individual Ni(L-asp) forming supramolecular bonds to two distinct Ni(L-asp) moieties and three solvent of crystallisation water molecules. The C1 carboxylate, which forms part of the 5-membered metallacycle accepts four hydrogen bonds from two neighbouring Ni(L-asp) moieties, and a single hydrogen bond from the solvent of crystallisation. More specifically, one Ni(L-asp) is bound through 2 cooperative hydrogen bonds from both oxygen atoms of the C1 carboxylate to a coordinated water molecule (C1O2···O5 = 2.836(1) Å) and an amine group of L-asp (C1O1···N1 = 2.944(1) Å) (Figure 5.5a), and the second Ni(L-asp) is bound via a single hydrogen bond between a coordinated water molecule and the O2 oxygen atom of the C1 carboxylate (O6···O2C1 = 2.825(1) Å) (Figure 5.5b). The solvent of crystallisation donates a hydrogen bond to the O2 oxygen (O7H71···O1C1 = 2.833(1) Å). The C4 carboxylate, which forms part of the 6-membered metallacycle, accepts two hydrogen bonds, one from a coordinated water molecule of a neighbouring Ni(L-asp) (O5···O3C2 = 2.691(1) Å), forming a 6-membered pseudo-metallacycle, and providing additional stabilisation to the coordination of the adjacent Ni(L-asp). The second hydrogen bond is donated from the solvent of crystallisation (O7···O4C4 = 2.954(1) Å). All the hydrogen bonding interactions are summarised in Table 5.3

The effect of the unit cell parameters of $[Ni(L\text{-}Asp)(H_2O)_2]\cdot H_2O$-I upon the application of pressure is summarised in Figure 5.6. The graphs show a distinct anisotropic response at 1.26 GPa, with the unit cell parameters *b* and *c* increasing, and *a* decreasing. This is associated with a phase change in the structure from to [Ni(L-

Asp)$(H_2O)_2$]•H_2O-I (Ni(L-asp)-I) to [Ni(L-Asp)$(H_2O)_2$]•H_2O-II (Ni(L-asp)-II). The focus of the rest of this chapter will be on the structural changes associated with the increasing application of pressure, focussing upon the supramolecular interactions and the covalent bonds within the crystal structures.

.

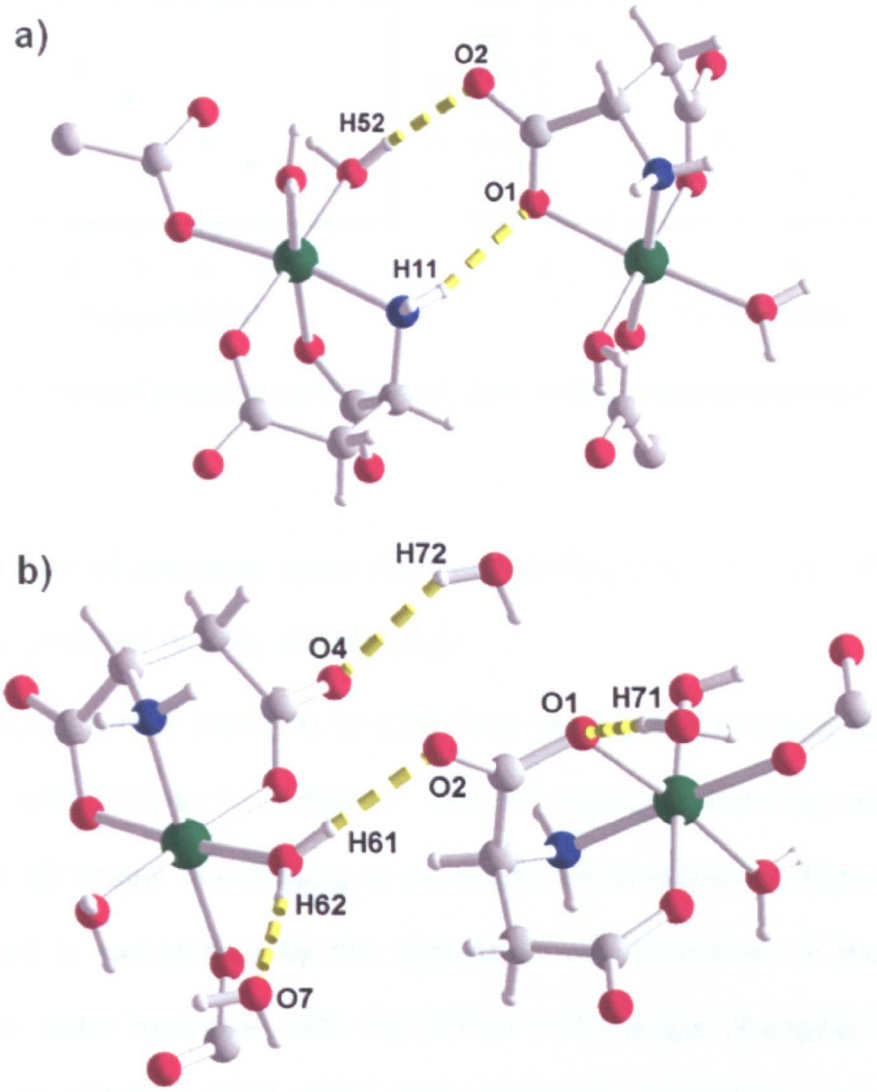

Figure 5.5. The supramolecular interactions of [Ni(L-Asp)$(H_2O)_2$]-I. a) The cooperative hydrogen bonding between the oxygen atoms of the C1 carboxylate, and a coordinated water molecule and the amine group of L-asp in a neighbouring [Ni(L-Asp)$(H_2O)_2$] moiety. b)The O2 oxygen of the C1 carboxylate bridges to a second [Ni(L-Asp)$(H_2O)_2$] moiety via a coordinated water molecule. The hydrogen bonds to the solvent of crystallisation are also evident.

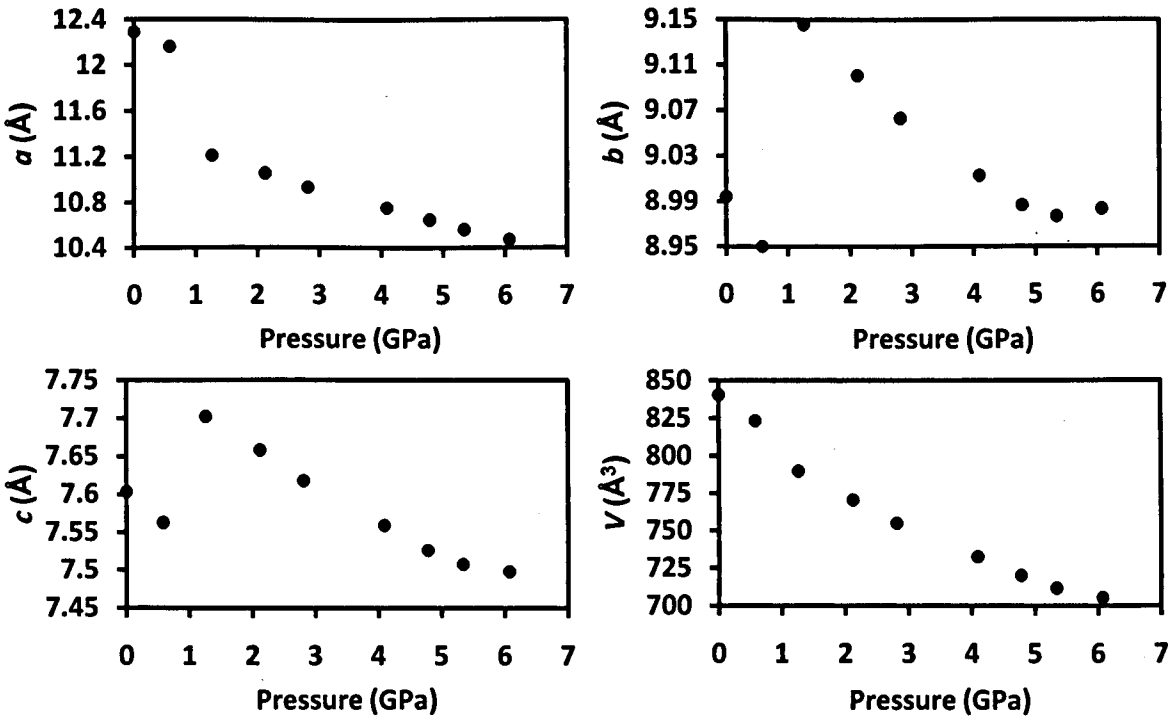

Figure 5.6. The effect of pressure upon the cell axes of $[Ni(L\text{-}Asp)(H_2O)_2]\cdot H_2O$.

5.2.3 The effect of pressure upon $[Ni(L\text{-}asp)(H_2O)_2]$-I up to 1.26 GPa, and the crystal structure of $[Ni(L\text{-}asp)(H_2O)_2]$-II

The initial application of pressure to 0.58 GPa causes the structure to contract in volume from 840.50(3) to 823.16(5) $Å^3$, with the hydrogen bonding interactions of between the 1D chains rearranging to maximise the interactions (Figure 5.7). This rearrangement is exemplified by the change in the orientation of the solvent of crystallisation water molecule, with the O7-H71···O1 angle changing from 163(1) (ambient P) to 178(3) ° (0.58 GPa). This change in orientation also effects the donor-acceptor distance of the hydrogen bonding interactions between O7H72···O4, destabilising the interaction, by increasing the length from 2.28(2) to 2.41(4) Å. The bond lengths of the hydrogen bonding interactions at ambient pressure and at 0.58 GPa are summarised in Table 5.3.

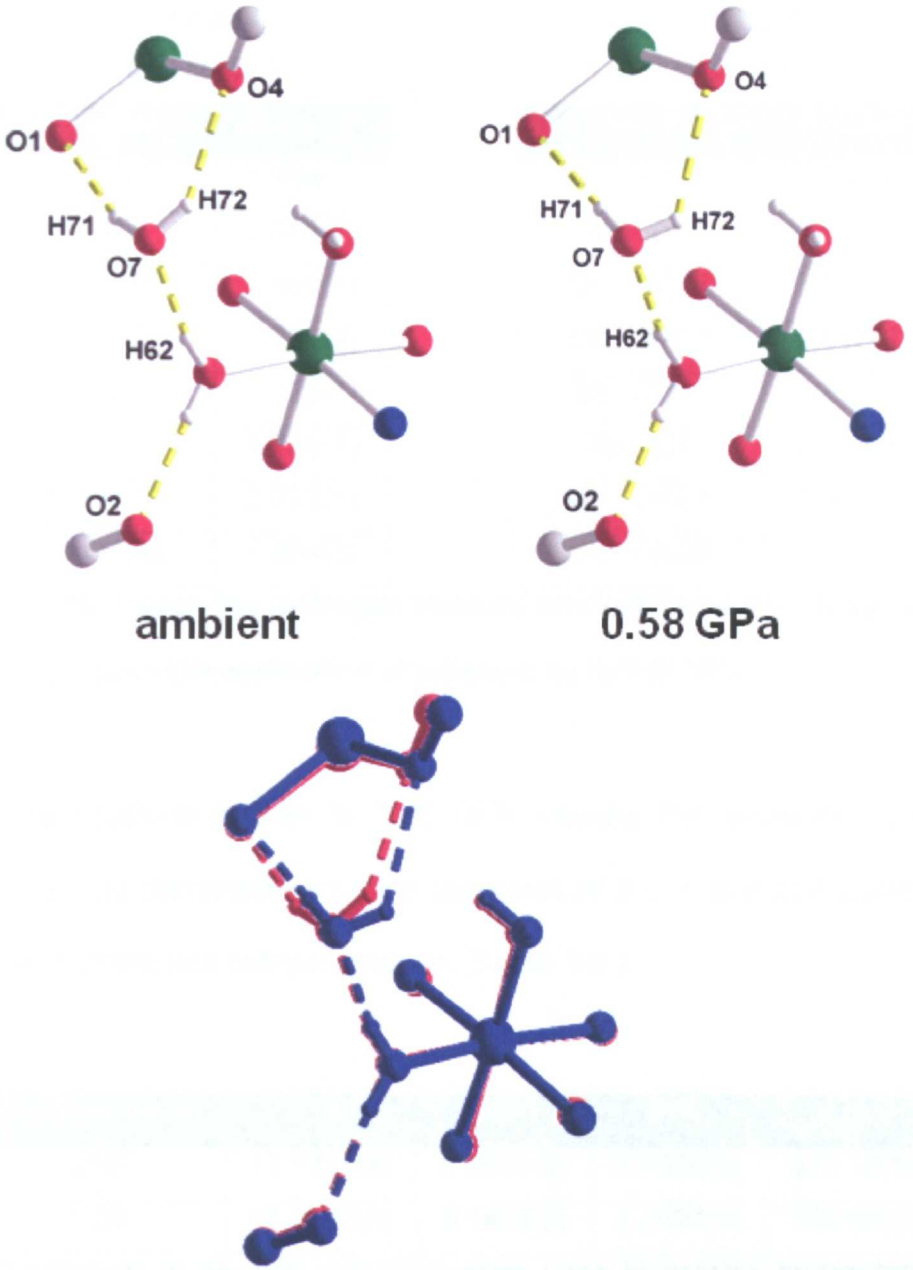

Figure 5.7. The effect upon the hydrogen bonding interactions upon the application of pressure up to 0.58 GPa. The change in orientation of the O7 water molecule at 0.59 GPa causes H71 to point directly at O1, and concurrently destabilised the H72···O4 interaction. This is exemplified by overlaying the two structures (bottom), with ambient pressure coloured red, and 0.58 GPa coloured blue.

P = Ambient *V = 840.50(3) Å^3*	
Interaction	**Dist / Å**
N1···O1C1	2.994(1)
N1···O7	2.971(1)
O5···O3C4	2.691(1)
O5···O2C1	2.836(1)
O6···O2C1	2.825(1)
O6···O7	2.724(1)
O7···O1C1	2.833(1)
O7···O4C4	1.954(1)

P = 0.58 GPa *V = 823.16(5) Å^3*	
Interaction	**Dist / Å**
N1···O1C1	2.966(4)
N1···O7	2.945(5)
O5···O3C4	2.687(4)
O5···O2C1	2.816(5)
O6···O2C1	2.793(5)
O6···O7	2.704(4)
O7···O1C1	2.809(5)
O7···O4C4	2.951(5)

Table 5.3. The effect upon the hydrogen bonding interactions in the crystal structure of [Ni(L-asp)(H_2O)$_2$]-I upon the application of pressure up to 0.58 GPa.

Increasing the pressure further to 1.26 GPa causes the structure to undergo a phase transition, as demonstrated by a reduction of 4% in unit cell volume, and an anisotropic shift in the unit cell parameters (Table 5.4.).

Pressure (GPa)	*a* (Å)	*b* (Å)	*c* (Å)	*V* (Å^3)
0.58	12.1614(4)	8.9501(2)	7.5626(3)	823.16(5)
1.26	11.2103(4)	9.1455(2)	7.7024(3)	789.68(5)

Table 5.4. The change in the unit cell parameters upon increasing hydrostatic pressure from 0.58 to 1.26 GPa.

The new high pressure phase, Ni(L-asp)-II, remains in the $P2_12_12_1$ space group, with the associated phase change arising from the Ni octahedra tilting out of the plane of the zigzagging Ni atoms described in section 5.2.2. In the ambient pressure phase (Ni(L-asp)-I), the axial water molecule Ni1-O6 points towards the plane of Ni atoms at an angle of 76.69(3) °, and upon the application of hydrostatic pressure, the Ni octahedron changes orientation, increasing the angle away from the plane to

100.18(8) ° at 0.58 GPa. However, within Ni(L-asp)-II at 1.26 GPa, the octahedron tilts in the opposite direction, orientating the axial water towards the plane at an angle of 58.14(5) ° (Figure 5.8).

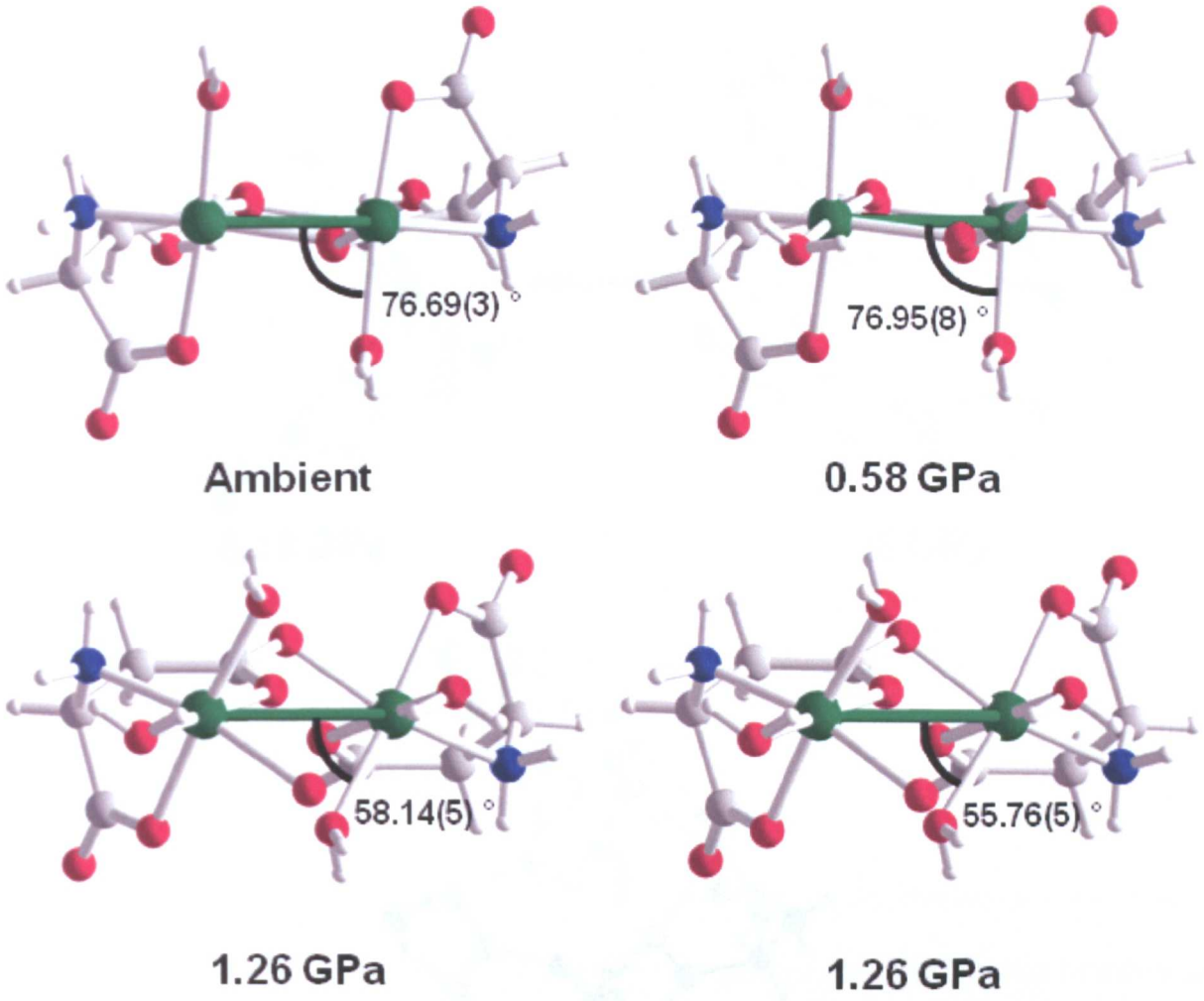

Figure 5.8. The effect of the octahedron tilt angle upon the application of pressure.

The tilting of the Ni octahedra also changes the orientation of the coordinated ligands within the solid state, having a direct impact upon the supramolecular bonds between the Ni(L-asp) 1D chains, and as such the structure undergoes a cooperative hydrogen bond rearrangement involving four donor-acceptor pairs (Figure 5.9). In addition, the water molecule included as a solvent of crystallisation

changes position, and pivots to change its hydrogen bonding contacts, with atom H71 changing from H71···O1 to H71···O4, and H72 changing from H72···O4 to H72···O4. The changes in the hydrogen bonding interactions upon the phase transition is summarised in Table 5.5.

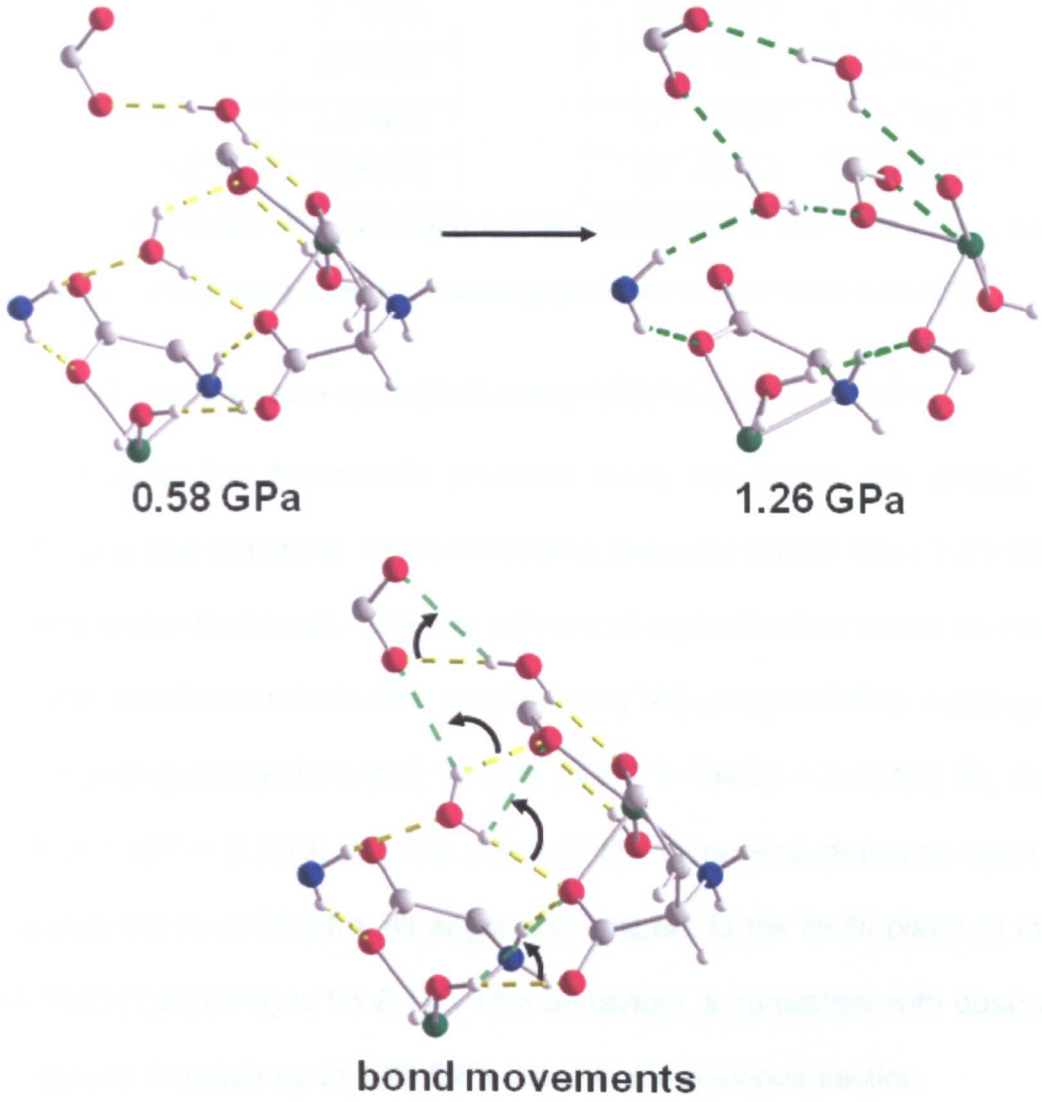

Figure 5.9. The cooperative hydrogen bond rearrangement upon increasing pressure from 0.58 to 1.26 GPa.

P = 0.58 GPa

V = 823.16(5) Å^3

Interaction	Dist / Å
N1···O1C1	2.966(4)
N1···O7	2.945(5)
O5···O3C4	2.687(4)
O5···O2C1	2.816(5)
O6···O2C1	2.793(5)
O6···O7	2.704(4)
O7···O1C1	2.809(5)
O7···O4C4	2.951(5)

P = 1.26 GPa

V = 789.68(5) Å^3

Interaction	Dist / Å
N1···O1	3.007(3)
N1···O7	2.966(3)
O5···O1C1	2.802(3)
O5···O3C4	2.877(3)
O6···O2C1	2.688(3)
O6···O7	2.670(3)
O7···O4C4	2.719(3)
O7···O2C1	2.670(3)

Table 5.5. The effect upon the hydrogen bonding interactions upon the phase transition from Ni(L-asp)-I to Ni(L-asp)-II upon increasing pressure from 0.58 to 1.26 GPa.

5.2.4 The effect of pressure upon [Ni(L-asp)(H_2O)$_2$]-II up to 6.07 GPa

Further increasing the hydrostatic pressure does not cause any further phase transitions to a new structure. Upon increasing pressure further from 1.26 GPa, the coordinated water molecules, and the solvent of crystallisation rotate to maximise the hydrogen bonding contacts with neighbouring Ni(L-asp) moieties, leading to new hydrogen bonding interactions at 2.12 GPa (N1H11···O4C2 = 2.414(2) Å), and 2.81 GPa (O5H52···O7 = 2.36(3) Å). The effect of the increasing pressure upon the Ni plane causes the Ni octahedral tilt angle with respect to the Ni-Ni plane to increase from 58.14(5) (1.26 GPa) to 93.2(1) °. This behaviour is consistent with observations in the pressure increase up to 1.26 GPa noted in the previous section.

5.2.5 Topological analysis

An alternative method of measuring the change in structure upon the application of hydrostatic pressure is to determine the change in topology. Utilising topological analysis introduced in chapter 3 to this structure, and assigning the nodes as Ni atoms, and the connections between adjacent Ni(L-asp) moieties as edges demonstrates that the structure is of the network type **lcy**,[18] a topology based upon extended metaprisms comprised of four faces, one triangular and three pentagular (Figure 5.10a and b), with the internal angles defining the base triangle each equal to 60°, and the external angles that define the apex linked by 3 pentagons equal to 99.59° (Figure 5.10c). The ambient pressure structure of Ni(L-asp) is highly distorted away from the ideal geometrical arrangement for this topology, due to the difference in the length of the edges (5.3-7.3 Å), and the angles of the tetrahedron (internal triangle angles ranges: 45.9- 82.0°, external apex angles ranges: 100.1-122.4°) (Figure 5.10d).

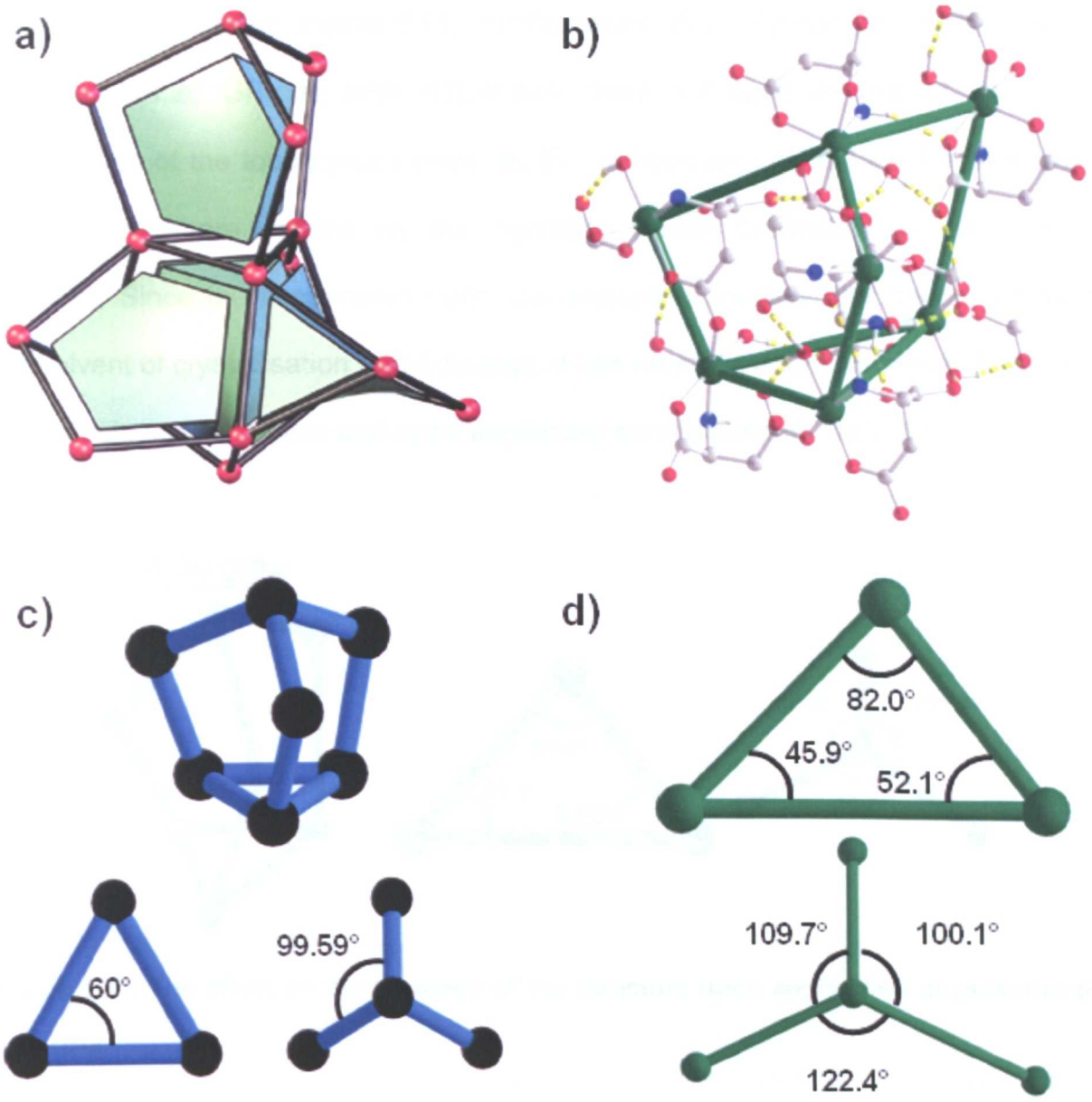

Figure 5.10. Topological analysis of Ni(L-asp)-I. a) The Icy topology comprised of extended metaprisms. b) A single metaprism of Icy within the structure of Ni(L-asp)-I, due to the hydrogen bonding connections and the *syn-anti* bridging functionality of a carboxylate group in L-asp. c) The ideal structure of Icy internal angles. d) The internal angles within Ni(L-asp)-I.

This initial application of pressure to 0.58 GPa affects the observed topology, changing the lengths of the edges (the distance between Ni atoms) and the angles which define the base and the apex, making the polyhedron defined in the previous

section more distorted (Figure 5.11). Further application of pressure past the phase change at 1.26 GPa to form Ni(L-asp)-II does not have an impact upon the connectivity of the topological bonds, as the vertices are defined as the Ni atoms, and the links are defined by the hydrogen bonds between $[Ni(L\text{-}asp)(H_2O)_2]$ moieties. Since the cooperative bond rearrangement involves the bonds between the solvent of crystallisation and Ni(L-asp), it has no effect upon the overall topology. The effects upon the base and apex angles are summarised in Table 5.6.

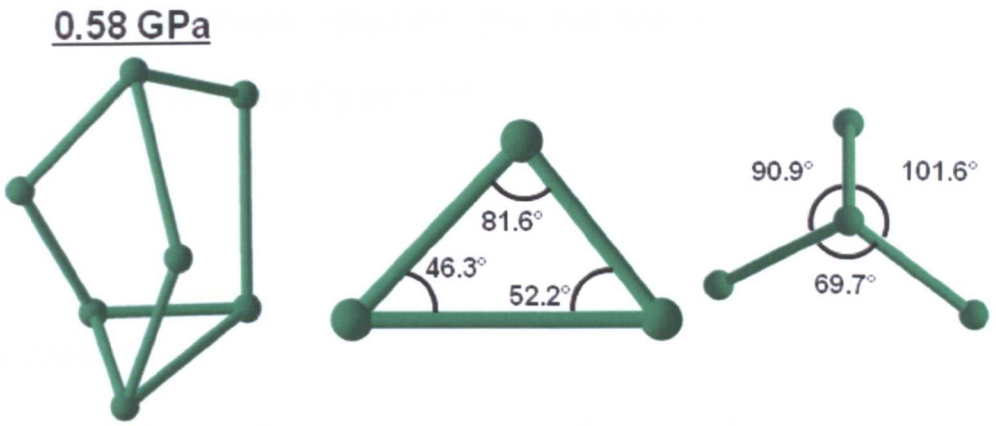

Figure 5.11. The effect on the topology of the structure upon application of pressure to 0.58 GPa.

Pressure (GPa)	Base angle range (°)	Apex angle range (°)
0	45.9 – 82.0	100.1 – 122.4
0.58	46.3 – 81.6	69.7 – 101.6
1.26	47.5 – 83.4	77.15 – 99.0
2.12	47.3 – 83.4	77.3 – 98.3
2.81	47.1 – 83.2	77.4 – 97.7
4.09	47.0 – 83.0	77.5 – 97.0
4.78	47.0 – 82.8	77.5 – 96.5
5.34	47.0 – 82.5	77.6 – 96.0
6.07	47.0 – 82.1	77.7 – 95.9

Table 5.6. The effect of pressure upon the base and apex angles of the topological polyhedra of $[Ni(L\text{-}asp)(H_2O)_2]$

Although there is no change in topology upon application of pressure, the change in the angles gives information about the flexibility of the structure. Between 0 and 0.58 GPa, the apex angles change dramatically, and upon the phase change at 1.26 GPa, the angles change drastically for a second time, reflecting the structural changes from the octahedra tilting and cooperative bond rearrangement. After the phase change, increasing the pressure further causes the ranges in the base and the apex to decrease, reducing the distortion to a more regular polyhedron. However, due to the difference in Ni-Ni distances from the different type of bonding contacts within the crystal structure, the polyhedron cannot adopt the ideal configuration of **Icy** shown in Figure 5.10.

5.3 Conclusion

The application of hydrostatic pressure to the chiral metal-organic framework [Ni(L-asp)$(H_2O)_2$]•H_2O-I undergoes a phase transition at 1.26 GPa to form Ni(L-asp)$(H_2O)_2$]•H_2O-II, which is demonstrated by a cooperative hydrogen bond rearrangement from the water molecule that exists as the solvent of crystallisation with neighbouring Ni(L-asp) moieties. This observation is consistent with pressure studies performed with other amino acid compounds,[19] such as cysteine,[20] which undergoes a phase transition affecting the hydrogen bonding interactions with the thiol side chain. Further application of pressure to Ni(L-asp)$(H_2O)_2$]•H_2O-II causes the structure to contract further, forming a more regular topological arrangement, as shown by the change in angles between the vertices of the network representation. The single crystal was stable up to a pressure of 6.07 GPa, and above this pressure, the sample became polycrystalline. This work highlights the possibility of

studying the structural effects of these crystalline materials under pressure, which could potentially be used for relating specific guest interactions in isotherms and species used in separation.

5.4 References

(1) Spencer, E. C.; Angel, R. J.; Ross, N. L.; Hanson, B. E.; Howard, J. A. K. *J. Am. Chem. Soc.* **2009**, *131*, 4022-4026.

(2) Moggach, S. A.; Bennett, T. D.; Cheetham, A. K. *Angew. Chem. Int. Ed.* **2009**, *121*, 7221-7223.

(3) Espallargas, G. M.; Brammer, L.; Allan, D. R.; Pulham, C. R.; Robertson, N.; Warren, J. E. *J. Am. Chem. Soc.* **2008**, *130*, 9058-9071.

(4) Park, K. S.; Ni, Z.; Cote, A. P.; Choi, J. Y.; Huang, R.; Uribe-Romo, F. J.; Chae, H. K.; O'Keeffe, M.; Yaghi, O. M. *PNAS* **2006**, *103*, 10186-10191.

(5) Banerjee, R.; Phan, A.; Wang, B.; Knobler, C.; Furukawa, H.; O'Keeffe, M.; Yaghi, O. M. *Science* **2008**, *319*, 939-943.

(6) Piermarini, G. J.; Block, S.; Barnett, J. D.; Forman, R. A. *J. Appl. Phys.* **1975**, *46*, 2774-2780.

(7) Bruker-Nonius SAINT version 7, Bruker-AXS: Madison, Wisconsin, USA, 2006.

(8) Sheldrick, G. M. SADABS Version 2004-1, Bruker-AXS: Madison, Wisconsin, USA, 2004.

(9) Betteridge, P. W.; Carruthers, J. R.; Cooper, R. I.; Prout, K.; Watkin, D. J. *J. Appl. Cryst.* **2003**, *36*, 1487.

(10) Altomare, A.; Cascarano, G.; Giacovazzo, C.; Guagliardi, A.; Burla, M. C.; Polidori, G.; Camalli, M. *J. Appl. Cryst.* **1994**, *27*, 435-435.

(11) Dawson, A.; Allan, D. R.; Parsons, S.; Ruf, M. *J. Appl. Cryst.* **2004**, *37*, 410-416.

(12) Parsons, S., SHADE, The University of Edinburgh: Edinburgh, United Kingdom, 2004.

(13) Brandenburg, K.; Putz, H. DIAMOND, Crystal Impact: Bonn, Germany, 2005.

(14) Bruno, I. J.; Cole, J. C.; Edgington, P. R.; Kessler, M.; Macrae, C. F.; McCabe, P.; Pearson, J.; Taylor, R. *Acta Cryst.* **2002**, *B58*, 389-397.

(15) Allen, F. H. *Acta Cryst.* **2002**, *B58*, 380-388.

(16) Allen, F. H.; Motherwell, W. D. S. *Acta Cryst.* **2002**, *B58*, 407-422.

(17) Antolini, L.; Menabue, L.; Pellacani, G. C.; Marcotrigiano, G. *J. Chem. Soc., Dalton Trans.* **1982**, 2541–2543.

(18) Friedrichs, O. D.; O'Keeffe, M.; Yaghi, O. M. *Acta Crystallogr.* **2003**, *A59*, 515-525.

(19) Moggach, S. A.; Parsons, S.; Wood, P. A. *Crystallography Reviews* **2008**, *14*, 143-184.

(20) Moggach, S. A.; Allan, D. R.; Clark, S. J.; Gutmann, M. J.; Parsons, S.; Pulham, C. R.; Sawyer, L. *Acta Crystallogr.* **2006**, *62*, 296-309.